NUMERICAL SIMULATION OF FLOW FIELD INSIDE A SQUEEZE FILM DAMPER AND THE STUDY OF THE EFFECT OF CAVITATION ON THE PRESSURE DISTRIBUTION

A Thesis

by

MILIND NANDKUMAR KHANDARE

Submitted to the Office of Graduate Studies of
Texas A&M University
in partial fulfillment of the requirements for the degree of

MASTER OF SCIENCE

December 2010

Major Subject: Mechanical Engineering

NUMERICAL SIMULATION OF FLOW FIELD INSIDE A SQUEEZE FILM DAMPER AND THE STUDY OF THE EFFECT OF CAVITATION ON THE PRESSURE DISTRIBUTION

A Thesis

by

MILIND NANDKUMAR KHANDARE

Submitted to the Office of Graduate Studies of
Texas A&M University
in partial fulfillment of the requirements for the degree of

MASTER OF SCIENCE

Approved by:

Chair of Committee,	Gerald L. Morrison
Committee Members,	Je-Chin Han
	Hamn-Ching Chen
Head of Department,	Dennis O' Neal

December 2010

Major Subject: Mechanical Engineering

ABSTRACT

Numerical Simulation of Flow Field Inside a Squeeze Film Damper and the Study of the Effect of Cavitation on the Pressure Distribution. (December 2010)

Milind Nandkumar Khandare, B.E., University of Pune, India

Chair of Advisory Committee: Dr. Gerald L. Morrison

Squeeze Film Dampers (SFDs) are employed in high-speed Turbomachinery, particularly aircraft jet engines, to provide external damping. Despite numerous successful applications, it is widely acknowledged that the theoretical models used for SFD design are either overly simplified or incapable of taking into account all the features such as cavitation, air entrainment etc., affecting the performance of a SFD. On the other hand, experimental investigation of flow field and dynamic performance of SFDs can be expensive and time consuming. The current work simulates the flow field inside the dynamically deforming annular gap of a SFD using the commercial computational fluid dynamics (CFD) code Fluent and compares the results to the experimental data of San Andrés and Delgado. The dynamic mesh capability of Fluent and a User Defined Function (UDF) was used to replicate the deforming gap and motion of the rotor respectively.

Two dimensional simulations were first performed with different combinations of rotor whirl speed, operating pressures and with and without incorporating the cavitation model. The fluid used in the simulations was ISO VG 2 Mobil Velocite no. 3.

After the successful use of the cavitation model in the 2D case, a 3D model with the same dimensions as the experimental setup was built and meshed. The simulations were run for a whirl speed of 50 Hz and an orbit amplitude of 74 μm with no through flow and an inlet pressure of 31kPa (gauge). The resulting pressures at the mid-span of the SFD land were obtained. They closely agreed with those obtained experimentally by San Andrés and Delgado.

DEDICATION

To my father

ACKNOWLEDGEMENTS

First and foremost I would like to thank my advisor, Dr. Gerald Morrison, who has provided invaluable guidance throughout the course of the research. I am deeply indebted to him for teaching me the methodology of research and being extremely patient while doing so.

I would also like to thank Dr. Je Han and Dr. Hamn-Ching Chen for acting as members of my thesis committee and providing valuable inputs. I am especially grateful to Dr. Chen for explaining several aspects of a commercial CFD solver in his immensely informative CFD courses. I wish to thank Dr. Luis San Andrés from the ME Department for providing access to experimental data on SFD and Dr. Debjyoti Banerjee for his valuable inputs on cavitation.

I would like to take this opportunity to express my sincere gratitude to members of Dr. Morrison's research group, Anand Vijaykmar and Aarathi Sekaran, for their help. I also wish to thank Shriram Jagannathan for his occasional help. Last but not least, I wish to thank Ms. Shraddha Sangelkar and Dr. Adolfo Delgado from the Tribology group at the Turbomachinery Lab for providing invaluable insights about several aspects of the Squeeze Film Damper in general and the vertical SFD test rig in particular.

NOMENCLATURE

C	Radial Clearance, m
C_{xx}, C_{xy}	Direct and Cross Coupled Damping Coefficients
H	Dynamic Film Thickness
K_{xx}, K_{xy}	Direct and Cross Coupled Stiffness Coefficients
M_{xx}, M_{xy}	Direct and Cross Coupled Inertia Coefficients
P	Dynamic Pressure
Pmin	Minimum Static Pressure in the Clearance
Pmax	Maximum Static Pressure in the Clearance
R	Polar Coordinate in the Radial Direction
T	Time
U_x, U_y, U_θ	Velocity Components in the X, Y and Azimuthal Directions Respectively
Fmag	Magnitude of Force on Rotor
Vof	Volume Fraction
ε	Dissipation of Turbulent Kinetic Energy
κ	Turbulent Kinetic Energy
μ	Dynamic Viscosity, Pa/s
ρ	Fluid Density at Tooth Inlet, kg/m^3
θ	Polar Coordinate in Azimuthal Direction

TABLE OF CONTENTS

Page

LIST OF FIGURES

Page

Page

Page

Page

Page

Page

Page

LIST OF TABLES

Page

1. INTRODUCTION

Squeeze Film Dampers are extensively used in various high-speed Turbomachinery applications, particularly in the aerospace industry, to provide external damping, dissipation of vibration energy, isolation of structural components and improvement of the dynamic stability characteristics of rotor-bearing systems [1]. A Squeeze Film Damper consists of a non-rotating journal, a fixed outer bearing and a lubricant film which is created by supplying lubricant at a specified pressure to the clearance between the two. The whirling motion of the journal, due to the unbalanced forces, gives rise to a dynamic pressure by squeezing the squeeze film of oil which in turn causes damping of rotor motions. By analyzing the flow field in the clearance one can predict the damping characteristics of the SFD.

Cavitation affects the performance of SFDs greatly. Zeidan et.al [2] found that cavitation, especially gaseous cavitation, had a drastic effect on the dynamic pressure profile resulting in reduction in the positive pressure and its circumferential extent. Zeidan and Vance [3] characterize cavitation into several regimes- 1.Uncavitated film, typically in low speed and sealed end SFDs. 2. Cavitation bubble formed from entrained air, following the journal. This type of cavitation regime is observed in relatively low speed ventilated SFDs with low supply pressures. 3. Oil air mixture regime for high speed cases compared to the previous regime. 4. Vapor cavitation. This occurs only if

---

This thesis follows the style of *The Shock and Vibration Digest*.

tight end seals are present and the supply pressure is high. In other words, the entrainment of atmospheric air into the SFD is prevented and the cavitation occurs solely because the negative pressure in the film falls below the vapor pressure of the oil. 5. A combination of gaseous and vapor cavitation. Another sub category is the expansion of previously dissolved gases in the oil due to drop in pressure. The experimental analysis of cavitation on the squeeze film supported rotor by Zeidan et al [4], yielded non-linear response characteristics. Reliable models for predicting performance of SFD taking into account this effect of cavitation and air-entrainment are not available.

Experimentally investigating SFD characteristics for design purposes can be very expensive. With the constantly evolving commercial CFD software and availability of faster computers it has becoming possible to investigate flows involving complex geometries and phenomenon such as cavitation. The current study examines the possibility of establishing CFD as a feasible methodology to study SFD characteristics, especially from the design perspective, by using appropriate numerical models. The computer simulation will be compared and to the experimental results of Delgado and San Andres [5] to determine the applicability of the CFD technique.

Researchers have studied the suitability of applying CFD to the study of Squeeze Film Dampers but they have used either simplified 2D geometry with laminar flow models [6], validated their results against the solution to the simplified Reynolds equation [6] or compared to various lubrication theory numerical calculation programs [7]. The current work uses a 3D flow domain with experimental data for validation.

2. A BRIEF DESCRIPTION OF SFD CONFIGURATION AND TERMINOLOGY

A typical Squeeze Film Damper configuration consists of a non-rotating journal and a stationary outer housing as shown in Figure 1. The spinning of the journal about its axis is constrained by an anti-rotation pin or a squirrel cage. The journal is mounted on a ball bearing assembly. The small gap between the housing and the journal is filled with a lubricant film. The lubricant may be supplied at high pressure. As the journal whirls due to the dynamic forces generated by the rotor, the lubricant is displaced giving rise to hydrodynamic reaction forces. These forces damp the motion of the journal thereby reducing the vibration amplitude.

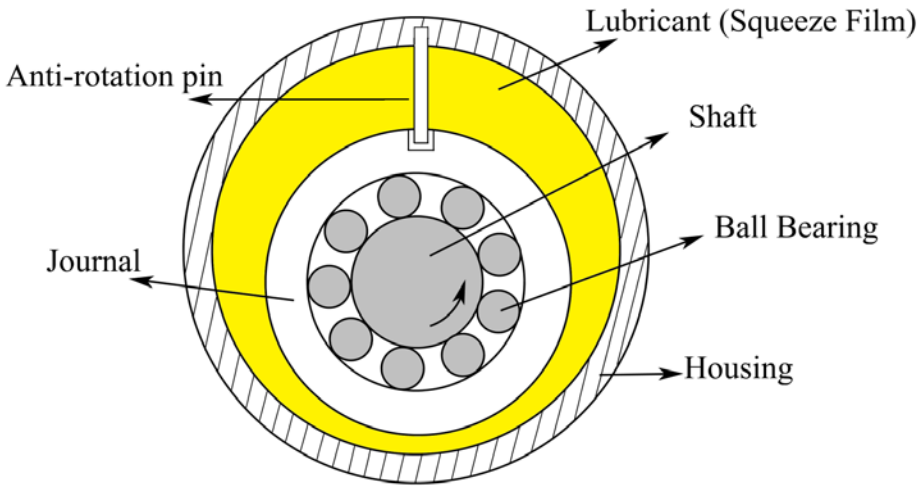

Figure 1. Simplified Configuration of a Typical Squeeze Film Damper [1] (the Lubricant Film is Exaggerated in Size)

Reynolds's equation based governing equation of the dynamic pressure distribution is [1]:

$$\frac{\partial}{R\partial\theta}\left(h^3\frac{\partial P}{R\partial\theta}\right)+\frac{\partial}{\partial z}\left(h^3\frac{\partial P}{\partial z}\right)=12\mu\frac{\partial h}{\partial t}+\rho h^2\left(\frac{\partial^2 h}{\partial t^2}\right) \tag{2.1}$$

where, P is the dynamic pressure, h is the dynamic film thickness, μ is the dynamic viscosity of the lubricant, R, θ and z are the polar coordinates with z along the SFD axis and t is time. Although numerical solutions to the above governing equation are available they do not take into account air-ingestion and entrapment, possible turbulent flow or fluid inertia.

The general force balance equation is

$$M\ddot{x}+C\dot{x}+Kx+F=0 \tag{2.2}$$

where M, C and K are Inertia, Damping and Stiffness Coefficients respectively.

In an SFD, since there are no reaction forces due to static journal displacements, the stiffness coefficient will be absent. Therefore the equation is reduced to: $M\ddot{x}+C\dot{x}+F=0$

This can be represented component-wise as follows:

$$\begin{pmatrix}F_x\\F_y\end{pmatrix}=-\begin{pmatrix}C_{xx}&C_{xy}\\C_{yx}&C_{yy}\end{pmatrix}\begin{pmatrix}v_x\\v_y\end{pmatrix}-\begin{pmatrix}M_{xx}&M_{xy}\\M_{yx}&M_{yy}\end{pmatrix}\begin{pmatrix}a_x\\a_y\end{pmatrix} \tag{2.3}$$

The various coefficients are-

C_{xx} , C_{yy} - Direct viscous Damping Coefficients

C_{xy} , C_{yx} - Cross-coupled viscous Damping Coefficients

M_{xx} , M_{yy} – Direct Fluid Inertia Coefficients

M_{xy} , M_{yx} - Cross-coupled Fluid Inertial Coefficients

The cross-coupled coefficients arise due to the motion perpendicular to the direction of force. SFD performance depends on several factors such as dimensions (diameter, land length, clearance), operating RPM, physical properties of lubricant, oil supply pressure, type of end seal, category of cavitation (vapor or gaseous or air ingestion) etc. Cavitation reduces the damping capability of the SFD. Hence it is necessary to include the complex effects of cavitation, in the pressure distribution prediction models.

3. LITERATURE REVIEW

3.1 Numerical Studies of Squeeze Film Damper Flow Field

PYP Chen and E J Hahn [6] investigated the suitability of applying CFD to Squeeze Film Dampers. They employed a 2D steady state laminar flow model based upon the Reynolds equation to validate the CFD results. They investigated the applicability of the Reynolds equation, which neglects the inertia and certain viscous terms, to short and long SFDs. A grid of 360X8 was used for the 2D geometry. It was found that the inertia effects predicted by CFD agreed well with results in the literature. Their results confirmed the assumption of constant pressure across the film. Guo et al [7], in their paper very briefly discussed the application of CFD analysis to SFDs, however no quantitative comparison was provided. They performed their simulations on a 1.18 in (30 mm) long damper with a radial clearance of 1.18 mil (0.03 mm), 0.79 mil (0.02 mm) eccentricity, whirl speed of 200 rad/s (1910 RPM) with the general purpose code CFX-TASCflow.

Changhu Xing et.al, [8] also used a commercial finite volume based algorithm CFD-ACE+ to study the effect of sealing on SFD performance and to develop the direct and cross-coupled coefficients for homogenous two-phase mixture films in a SFD. They also studied the effect of inertia forces and calculated these by using the actual value of the lubricant density and subsequently a density value of close to zero. The inertia coefficients from their study were compared with those reported by other researchers using the modified Reynolds's equation. The differences found between the two were

attributed to the three dimensional effects introduced by the additional terms in the full Navier-Stokes equations. A 288x18x27 3D grid was used in their studies.

3.2 Experimental Studies of Squeeze Film Damper Flow Field

L. Della Pietra and G. Adiletta [9, 10] in their paper "The Squeeze Film Damper over Four Decades of Investigations," summarize the main research findings pertaining to SFDs and their applications in the recent past. Thomsen and Andersen [11] were amongst the first to experimentally investigate a simple squeeze film damper to evaluate the effect of radial clearance and viscosity of the lubricant on the damping. They obtained the damping coefficients through measurement of radial support deflections. They found that for circular centered orbits (CCO) of small magnitudes, the damping coefficients were independent of rotor speed and vibration amplitude. Vance and Kirton [12] carried out an experimental investigation of the dynamic force response of a squeeze film bearing damper. They measured the dynamic pressure field for a journal performing Circular Centered Orbits to calculate the force components. Their findings showed good agreement with the long-bearing theory predictions. Feder et al [13] investigated the Squeeze Film Damper forces produced by Circular Centered Orbits. They concluded that inlet and cavitation pressures can have very important effects on damper forces. Analytical predictions, verified by the experimental results, showed that for damper pressures distributions between 180 and 360 degree an increase of inlet and/or cavitation pressure increased the circumferential pressure distribution, increased the damper force and decreased the stiffness force. For the same dynamic pressure, the damping force for the 360 degree pressure distribution is twice that of the 180 degree

pressure distribution. Also, inlet and cavitation pressures could be linearly added to the dynamic pressures. The stiffness force for the 360 degree pressure distribution is zero and there is no further increase in the damping force once the 360 degree pressure distribution is reached. Bansal and Hibner [14] carried out the experimental and analytical investigation of Squeeze Film Damper forces induced by offset Circular Whirl Orbits. They found that experimentally measured values differed from the analytical predictions made using the long bearing assumption due to the effect of bearing clearances and shaft flexibilities.

San Andres and Vance [15] measured the effect of fluid inertia and film forces in a SFD with circular centered orbits. They recorded large pressures in the groove and showed that earlier assumptions of low pressure ($1/25^{th}$ of the pressure in the SFD land) and its uniformity in grooved regions were invalid. They also found that in the absence of leakage, the regions of largest pressure were close to the end walls of the SFD land and the pressure fell as one approached the groove. Variations in pressure field along the circumferential direction at a fixed axial location were found to be negligible due to the small size of the inlet orifice.

The studies discussed, were conducted for Reynolds numbers less than 10. Later, Jung, San Andres, and Vance [16, 17] carried out similar investigations at Reynolds numbers up to 50 with fully open ended and partially sealed SFD configurations. They also investigated the effect of cavitation on the pressure profile. For the fully sealed configuration, it was found that the axial pressure profile predicted by the short bearing approximation solution was agreeable for the positive dynamic pressure region but was

unsatisfactory for the negative dynamic pressure region. It was inferred that cavitation observed in the submerged SFD was due to vapor cavitation. Also, the inertia coefficients became comparable in magnitude with increasing Reynolds number. For the partially sealed configuration, it was found that the pressure varied only slightly along the axial direction implying that this configuration would provide high damping owing to the uniform pressure levels in the axial direction. The results showed that vapor cavitation significantly slowed the development of the negative pressure region and reduce the damping and inertial coefficients. The amount of cavitation increased with increasing Reynolds number. The amount of cavitation was found to be much higher in the partially sealed configuration than in the open ended configuration.

Lelio Della Pietra [18] also carried out an analytical (based on the Short Bearing theory) and experimental investigation of squeeze film dampers. An analytical expression was obtained for the pressure in the annular gap taking into consideration the effect of offset circular orbits. With the help of this expression, the effect of offset on the dynamic pressure was investigated. Good agreement between the theoretical prediction and experimental findings was observed for the positive part of the dynamic pressure. However, the predictions varied for the negative part due to cavitation. Arauz and San Andres [19] studied the effect of whirl frequency and fluid viscosity on the dynamic force response of a SFD for both the open ended and partially sealed configurations. It was found that the open end seal configuration allowed flow of oil and prevented it from over-heating. The results showed that the partially sealed configuration SFD produced higher damping forces than the open configuration SFD.

Zeidan and Vance were amongst the first researchers to make a detailed study of the effects of cavitation on the SFD performance. Earlier Hahn and Feng [20] had proposed density and viscosity models for two phase homogenous hydrodynamic damper fluids and had done a preliminary investigation of the effect of cavitation on SFD performance [21]. Walter et al had also performed experimental observations of cavitating SFDs. Zeidan and Vance concluded that gaseous cavitation drastically reduced the load capacity of the damper. The assumption of a homogenous incompressible fluid for the analysis of an SFD was found to be grossly inadequate. It was noticed that at higher pressure, the splitting of gaseous cavities into smaller sized cavities led to the formation of a homogenous oil-air mixture. Large sized air cavities also continued to form separately and persisted in the high pressure region leading to a three phase mixture. They recommended incorporating the effects of a homogenous oil-air mixture and the compressible pockets of air in a compressible model for better prediction of SFD performance. In their subsequent studies, they investigated various cavitation regimes in SFDs and their effect on the pressure distribution. Five distinct cavitation regimes were identified by employing high speed motion photography. These were then characterized through pressure measurements. It was shown that air entrainment drastically reduced the pressure profile by reducing the negative pressure amplitude and preventing vapor cavitation from taking place. It increases the circumferential extent of the negative pressure. The presence of bubbles slows the development of positive pressure and reduces its amplitude. They suggested changes in

oil feed mechanisms, seals, outlet holes and supply pressure to reduce air entrainment into the damper and thus improve damper performance.

In later studies, Zeidan and Vance studied the effect of cavitation on the force coefficients. They varied parameters such as speed, operating eccentricity, end seals and supply pressure to study their effect on the extent of cavitation. They observed that air entrainment into the SFD has a very large influence on the force coefficients and the damper performance. They concluded that the radial damping coefficient changes from negative to positive due to air ingestion at low to medium eccentricities, the radial force coefficient remained unaffected at high eccentricities. They suggested that an effective end seal and high supply pressure could limit be used to reduce air ingestion into the damper.

4. OBJECTIVES

The following are the main objectives of this work:

1. To establish if the commercial CFD code Fluent® can be used to simulate the flow field inside a Squeeze Film Damper (SFD).
2. To use a 2D model to establish grid size and computer models required to obtain solutions.
3. Simulate one experimental condition considered by Delgado et. al [5].

Experimental study of the flow field inside a SFD can be expensive since it involves setting up a test rig and data acquisition system. Also, it can be cumbersome to study the effects of geometry change or journal eccentricity on the flow field. If CFD can be established as a valid, feasible alternative to experimentation, it would be immensely helpful for the study of SFDs from the design perspective. Cavitation in a squeeze film damper can be broadly divided into the following three categories: a) that due to expansion of dissolved gases (gaseous cavitation) b) that due to decrease in pressure below the vapor pressure of the lubricant (vapor cavitation) and c) that due to air entrainment into the SFD through recesses around probes and joints. This work will primarily address dissolved gases which will include the effect of quantity of dissolved air in the lubricating fluid. This could be the dominant category of cavitation at low speeds since typically; the vapor pressure of the lubricant is extremely low (of the order of a few Pascals). The present work uses the geometry of the test rig used in the experiments of San Andres & Delgado [5] and compares the CFD results with their experimental results.

5. METHODOLOGY

The geometry of the flow domain based upon Delgado et al [5] is as shown in the Figure on page 73. A full 3D simulation of this was used in the final stage of the study. The diameter of the journal is 5 in (127 mm), the clearance is 5 mil (0.127 mm) and the eccentricity is 2.9 mil (0.074 mm). The length of the SFD land is 1 in (25.4 mm). The frequency of rotation of the journal is 50 Hz. The journal follows a circular orbit. The study used grid generation software Gambit 2.4.6 and commercial computational fluid dynamics code Fluent 6.3.26.

Initially, 2D cases were simulated to determine the optimal mesh and time-step size. Grid-independence and time-step independence studies were carried out and a grid with 1440 nodes in the circumferential direction and 20 nodes across the clearance was selected. A time-step size such that the journal whirls by 1 degree per time-step was selected. Water was initially used as the working fluid and the operating pressures were varied to obtain varied degree of cavitation to demonstrate the use of the cavitation model. The working medium was then changed to oil (ISO VG 2 Mobil Velocite no.3 with density=800 kg/m^3 and a dynamic viscosity of 0.0016 kg/ms) and the effect of operating pressure, journal whirl speed, and dissolved air quantity in the oil was studied. The flow field was visualized using post-processing code Tecplot 360. The flow domain was exaggerated in size using a coordinate transformation. It has been established by several researchers that the flow field inside a SFD stabilizes after some time i.e. there is no variation in the pressure field along the circumferential direction at a fixed axial location. The simulations were run (unsteady solver) until there was no variation in the

pressure field to obtain the quasi-steady state pressure field. Although the dynamic mesh was ultimately used for the study, the possibility of applying a coordinate transformation technique to transform the problem to a steady state case was also examined. Under this technique, a relative circular motion was assigned to the fluid with respect to the journal while assuming the journal to be stationary. A steady state solver was used. However the pressure field obtained did not match with that obtained from the unsteady solver (dynamic, deforming mesh case). Therefore this technique as applied was found to be incapable of correctly predicting the flow field.

The numerical simulations were then performed on the full 3D model. A structured mesh (hexahedral cells) was generated using the mesh generation tool Gambit. A structured mesh was chosen over an unstructured one because of the number of cells in the mesh would have become prohibitively large due to the maximum allowable aspect ratio restriction for the unstructured grid. The grid has 1440 nodes in the circumferential direction, 20 in the radial direction across the clearance and 80 nodes along the axis. A total of 2.592 million hexahedral cells were created. Due to the large size of the mesh, it was partitioned and the Fluent parallel solver was used. An optimization study for the number of partitions was performed and 4 partitions were found to be optimal for the 8 processor machine used in the study.

This mesh was then imported into Fluent to simulate the flow field. The ‘Dynamic mesh’ capability of Fluent® gives the user the ability to simulate a flow domain which is changing in shape or size with time. The deformation of the domain is simulated by making the cells to radially compress or expand as the case might be by

assigning them a spring constant. Thus the dynamically deforming gap in the SFD can be achieved with the help of the dynamic mesh capability. A user defined function (UDF) was used to assign the circular motion to the journal. The UDF determines the position of each node on a surface of the mesh at a subsequent time-step in terms of its position at the current time-step.

An unsteady solver needed to be chosen since the flow domain changes with time. The mixture-multiphase model in Fluent was chosen to incorporate the effects of cavitation. The Standard k-ε model was selected with the Standard Wall Functions for the near-wall treatment. An operating pressure of 1 atm (101325 Pascals) was prescribed. The oil inlet is the top surface of the domain. In their experiments, San Andres and Delgado used a supply pressure of 31 kPa. Hence the inlet surface was assigned to be a pressure inlet at 31 kPa. A completely sealed outlet was assumed for the simulations. For the mixture-multiphase model, the default value of pre-dissolved gases is about 1% (percent by volume of lubricant). To study the variation in pressure field with the amount of dissolved gases, the runs were repeated with 3, 5 and 7 % dissolved gases. In the experimental work, pressures probes were installed at the mid-section of the SFD land for recording pressures. Therefore pressures along the circumference, at the mid-section of the SFD land (in the axial direction) were analyzed. Although the numerical results showed a good agreement with the experimental results, the pressures in the cavitation regime could not be accurately predicted. The reasons behind this discrepancy were investigated.

The next step to extend the scope of this work would be to investigate the flow field at higher speeds by eliminating the numerical instabilities encountered at large orbit speeds, enable non-circular orbits, study the effect of grooves/plenums inside the damper and study the effect of sealing.

6. RESULTS AND DISCUSSION

6.1 2D Geometry Studies

A structured mesh was created in the mesh generation software Gambit. The mesh has 1440 nodes in the circumferential direction and 20 nodes in the clearance as shown in Figure 2. Since the clearance (5 mil or 0.127 mm) is extremely small compared to the diameter (2.5 in or 63.5 mm), the clearance had to be enlarged to visualize it. Post-processing software Tecplot® was used. The following coordinate transformation was used for this purpose:

$$X' = \sqrt{X^2 + Y^2} \tag{6.1}$$

$$Y' = \tan^{-1}\left(\frac{Y}{X}\right) \tag{6.2}$$

$$\text{temp\_variable} = X' - 0.0632 \tag{6.3}$$

$$\text{Xmod} = \text{temp\_variable} \times \cos(Y') \tag{6.4}$$

$$\text{Ymod} = \text{temp\_variable} \times \sin(Y') \tag{6.5}$$

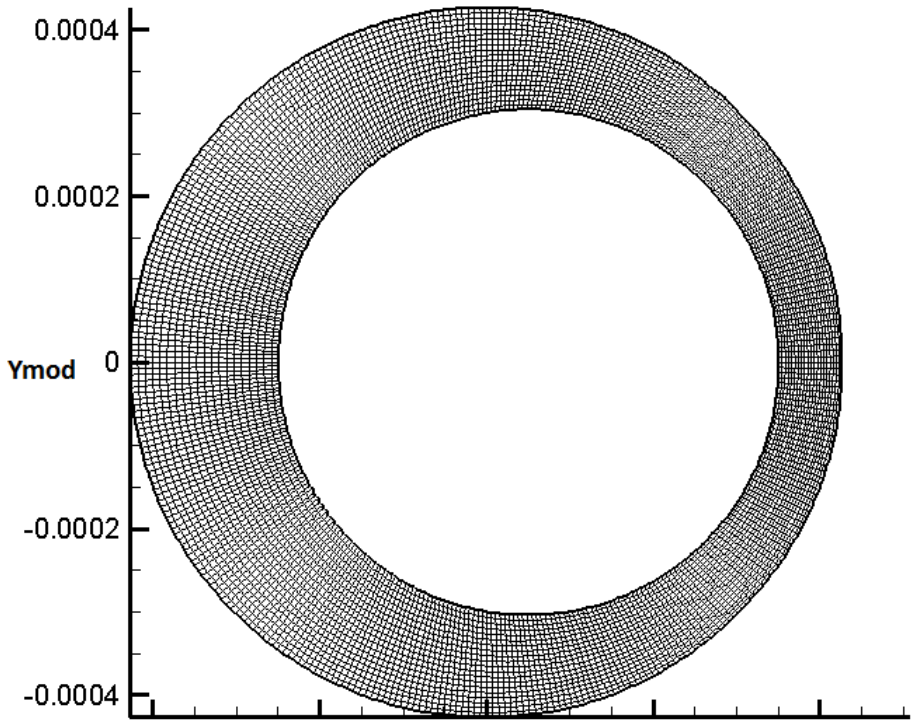

Figure 2. 2D Mesh 1440X20 (Nodes in Circumferential Direction Reduced to 360 for Clear Representation)

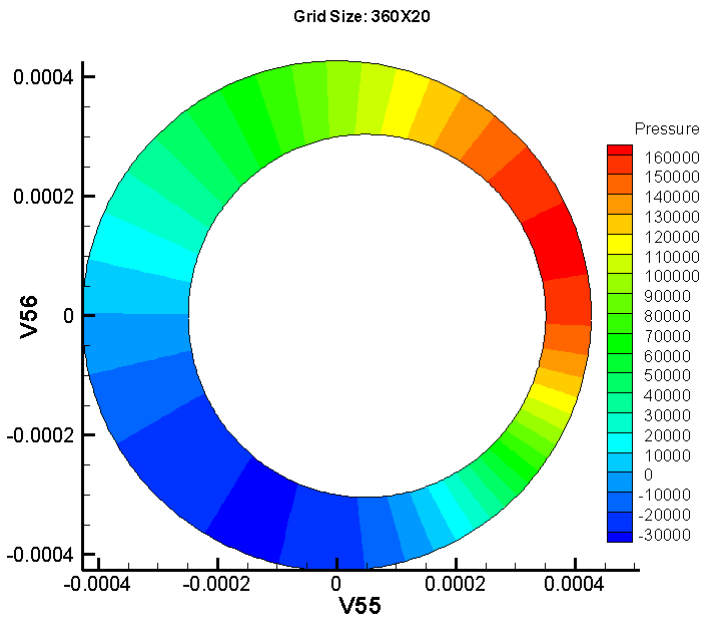

Figure 3. Contours of Pressure, Grid Size 360 (Circumferential Nodes) X 20 (Radial Nodes)

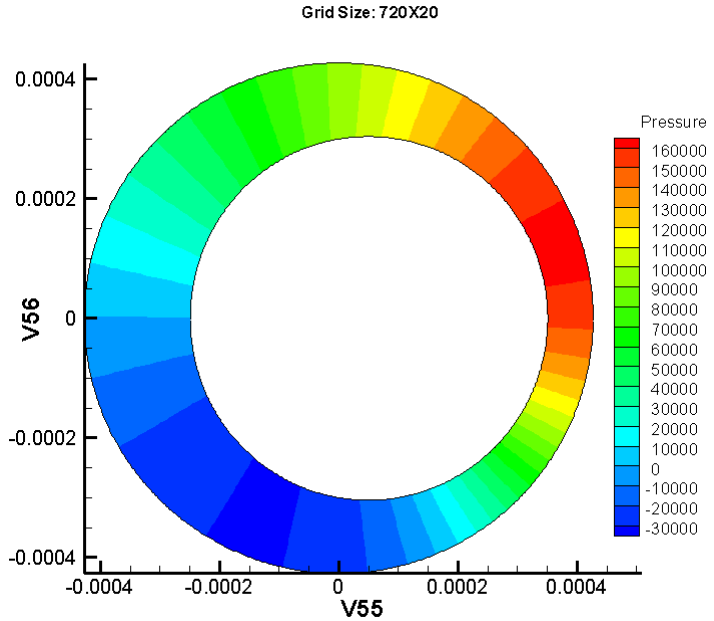

Figure 4. Contours of Pressure, Grid Size 720 (Circumferential Nodes) X 20 (Radial Nodes)

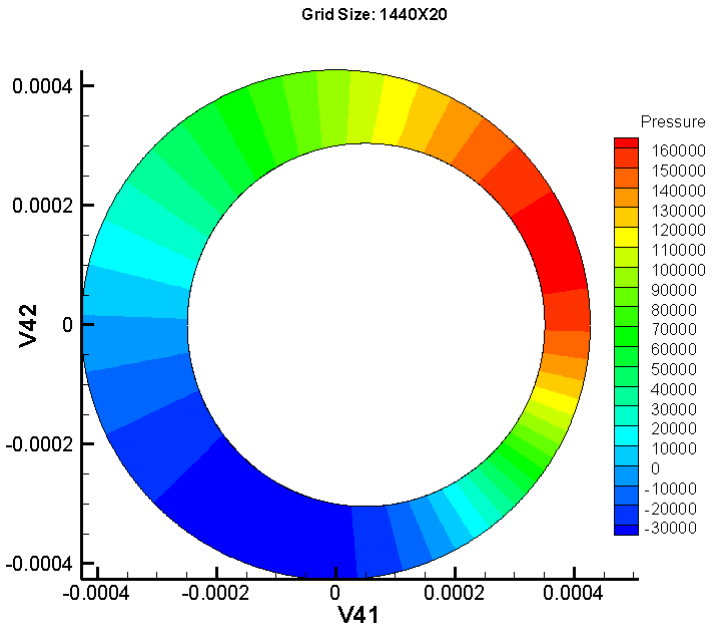

Figure 5. Contours of Pressure, Grid Size 1440 (Circumferential Nodes) X 20 (Radial Nodes)

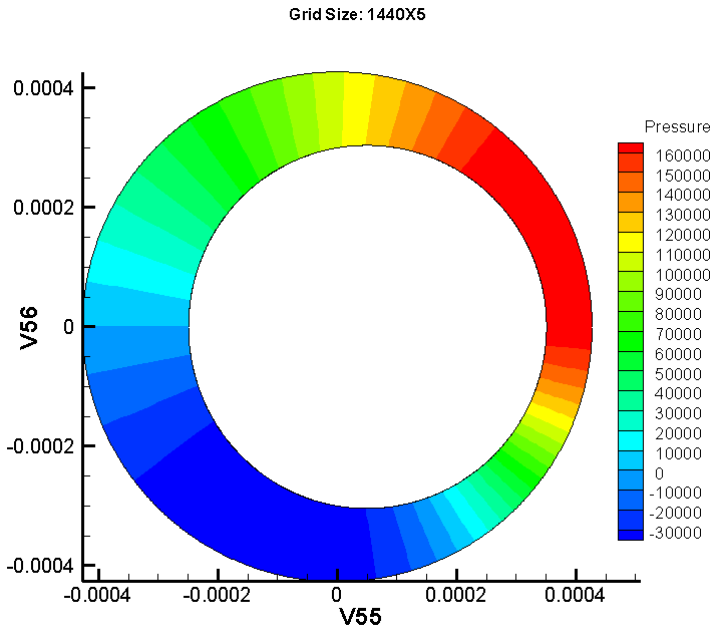

Figure 6. Contours of Pressure, Grid Size 1440 (Circumferential Nodes) X 5 (Radial Nodes)

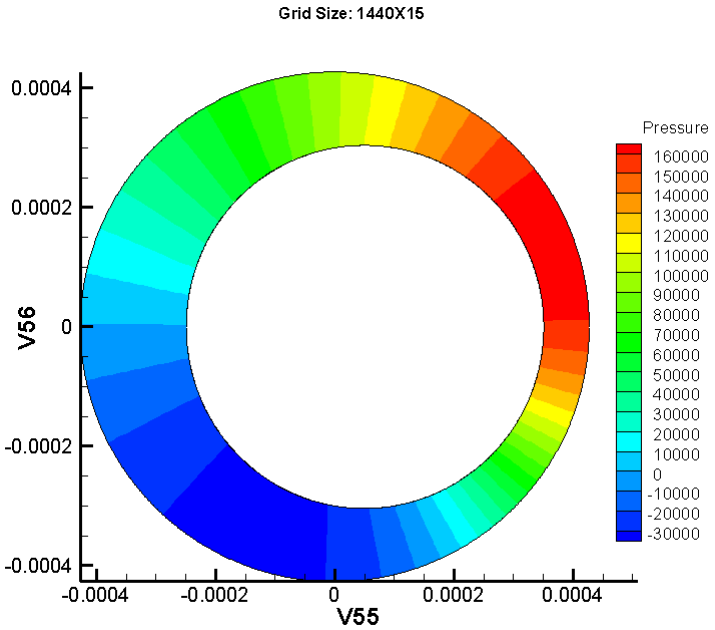

Figure 7. Contours of Pressure, Grid Size 1440 (Circumferential Nodes) X 15 (Radial Nodes)

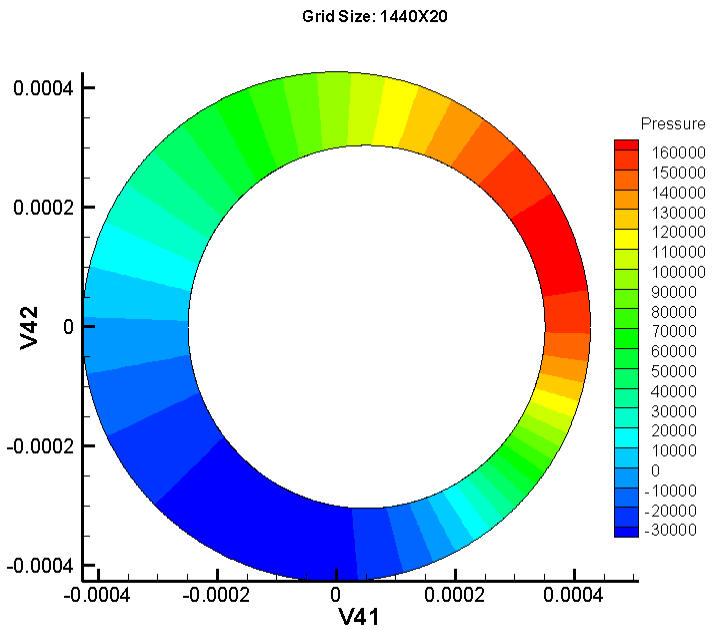

Figure 8. Contours of Pressure, Grid Size 1440 (Circumferential Nodes) X 20 (Radial Nodes)

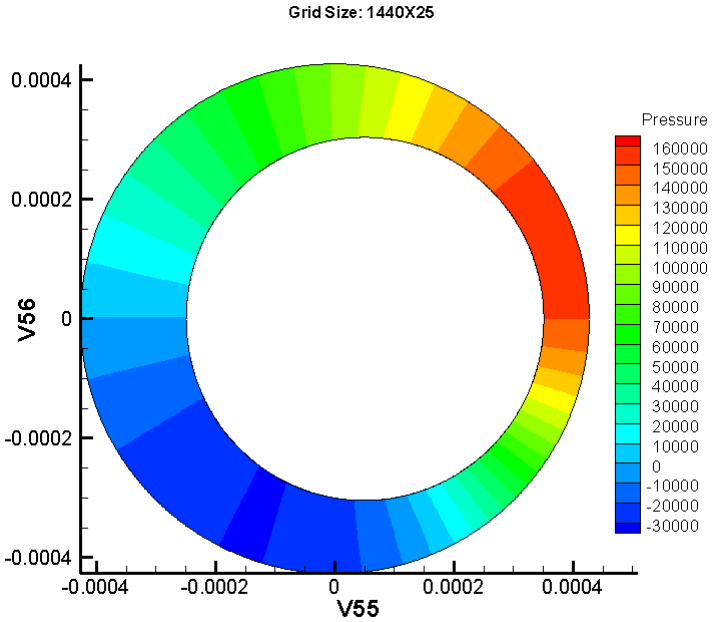

Figure 9. Contours of Pressure, Grid Size 1440 (Circumferential Nodes) X 25 (Radial Nodes)

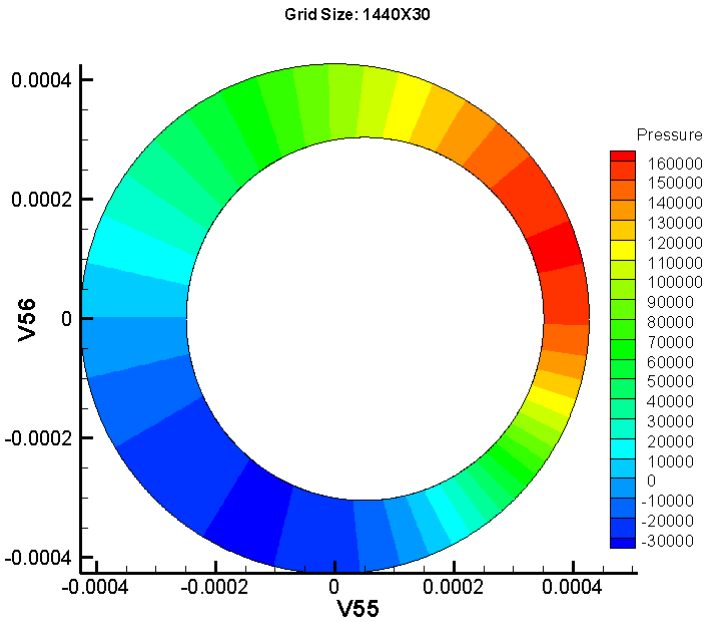

Figure 10. Contours of Pressure, Grid Size 1440 (Circumferential Nodes) X 30 (Radial Nodes)

6.2 Grid Independence Study (Pressure Contour Plots for Different Grid Sizes)

Since the pressure distribution was the quantity of interest rather than a single valued quantity, the contour plots of pressure (Figure 3 through Figure 10) needed to be monitored to establish grid independence. First the nodes in the circumferential direction were increased from 360 to 1440. Each consecutive value exceeded the preceding value by a multiple of 2. The number of nodes in the radial direction (in the annular gap) was maintained at a constant value of 20. Subsequently, the number of nodes in the circumferential direction was maintained at 1440 and the nodes in the annular gap were increased from 5 to 30 in steps of 5. As it can be seen from the contour plots, the pressure distribution does not vary to a large extent with grid sizes. Grid independence was thus established, it was decided to use the 1140X20 grid for the study.

To test the dynamic mesh setup, a preliminary case with no cavitation was run. The rotation RPM was varied from 540 RPM to 50X540 RPM. The working fluid used was Mobil Velocite 3. The physical properties are- Density = 800 kg/m^3, Viscosity = 0.0016 kg/m-s (2 cSt), Vapor pressure = 1mmHg (0.1336 kPa). The direction of rotation was anti-clockwise. The rotor started from zero whirl rate to the specified RPM at time t=0. The simulation was run until the solution became the same for all subsequent time steps, only rotating in time.

The following figures are the contours of pressure and velocity components (Figure 11 through Figure 25). Velocity vectors were also plotted for cases with increasing shaft speeds to take a close look at the flow field (Figure 26 through Figure 35). The red and blue regions represent high and low pressure zones respectively:

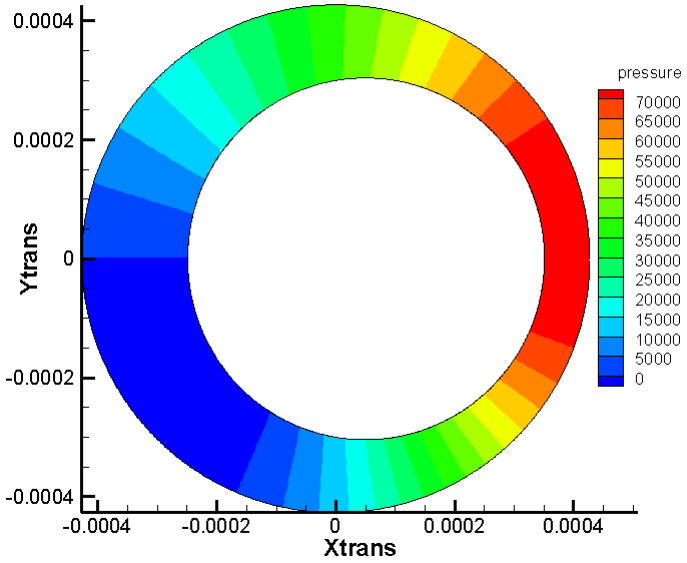

Figure 11. Contours of Pressure, 1X540 RPM

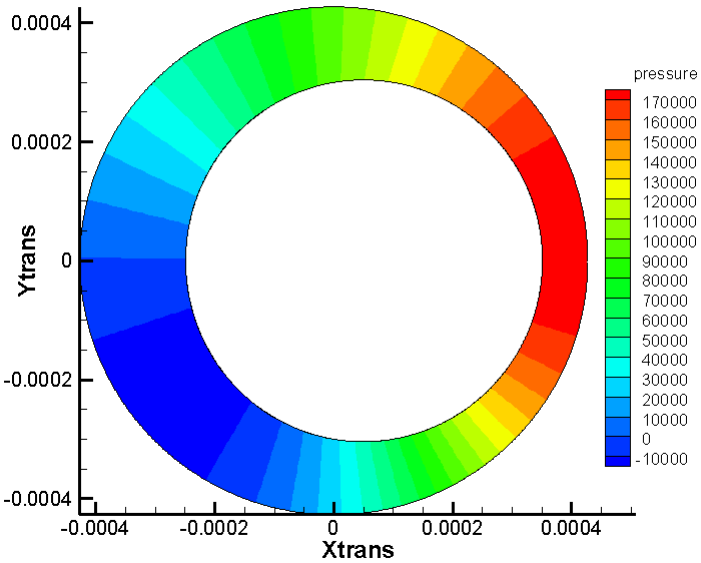

Figure 12. Contours of Pressure, 2X540 RPM

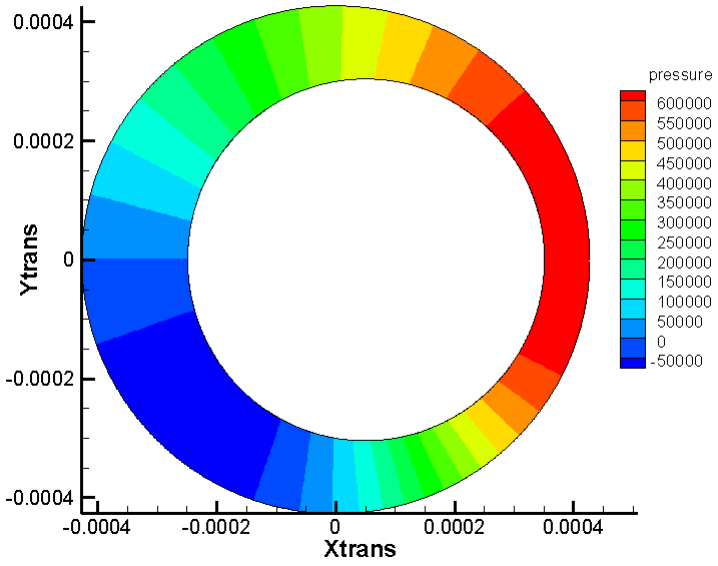

Figure 13. Contours of Pressure, 5X540 RPM

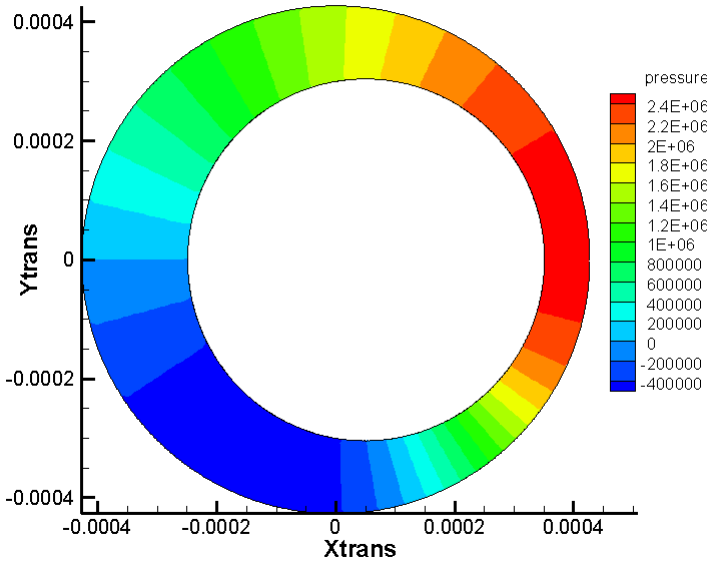

Figure 14. Contours of Pressure, 10X540 RPM

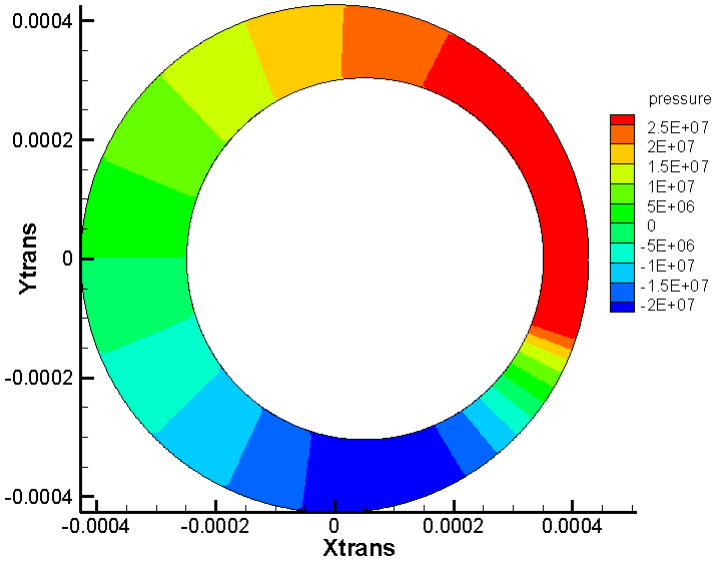

Figure 15. Contours of Pressure, 50X540 RPM

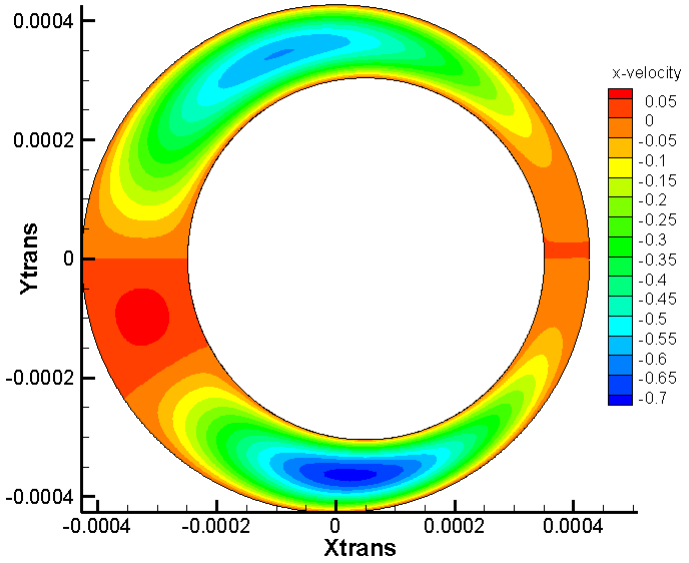

Figure 16. Contours of X Velocity, 1X540 RPM

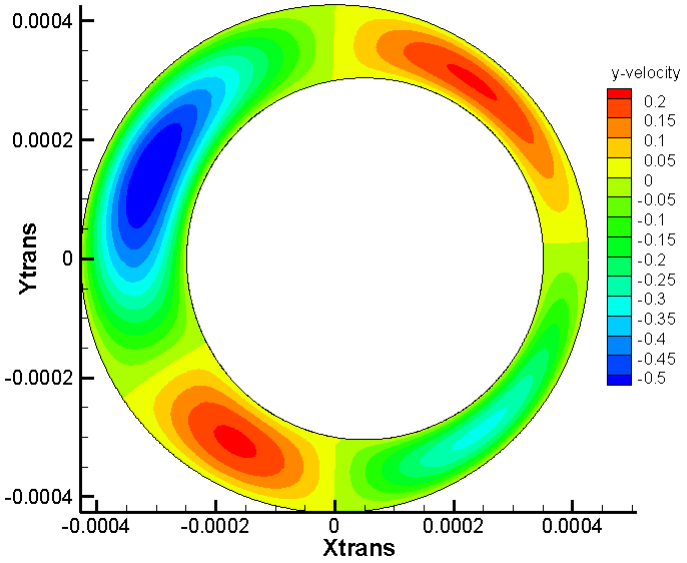

Figure 17. Contours of Y Velocity, 1X540 RPM

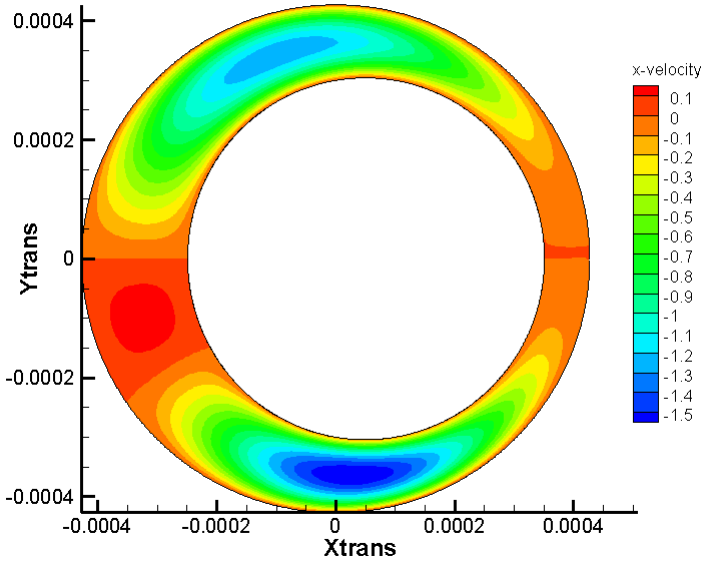

Figure 18. Contours of X Velocity, 2X540

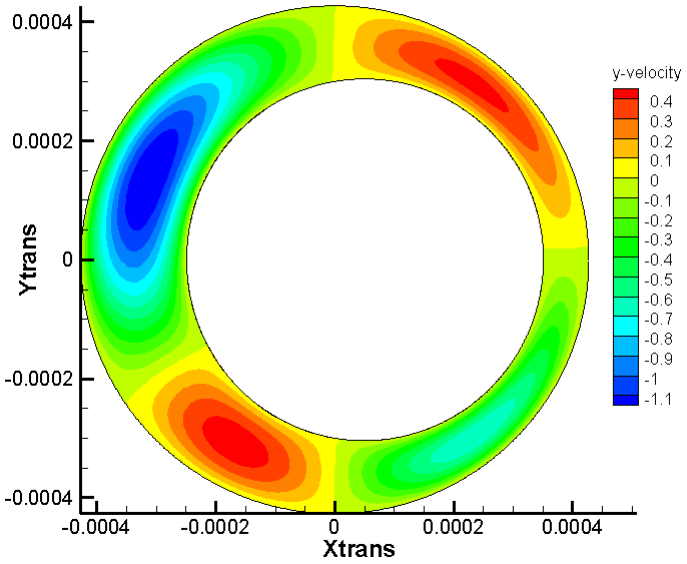

Figure 19. Contours of Y Velocity, 2X540 RPM

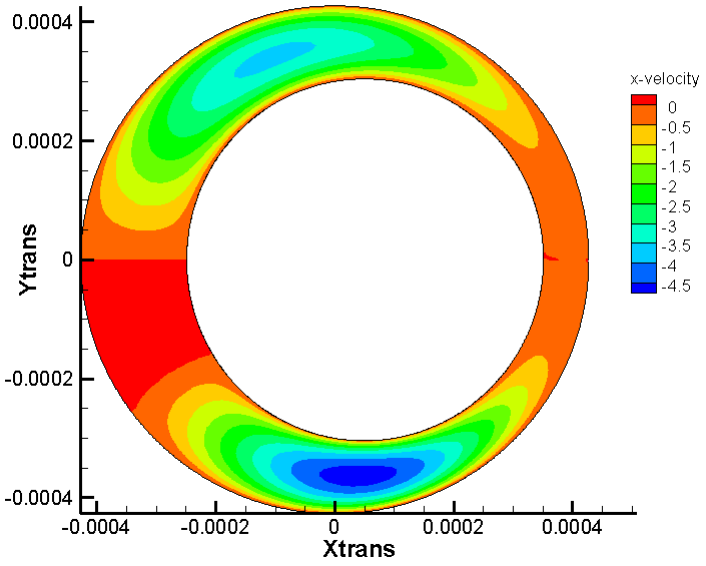

Figure 20. Contours of X Velocity, 5X540 RPM

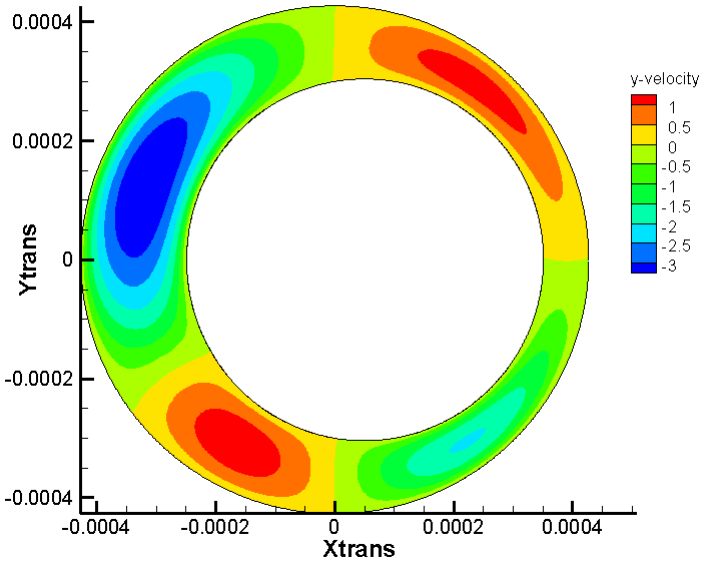

Figure 21. Contours of Y Velocity, 5X540 RPM

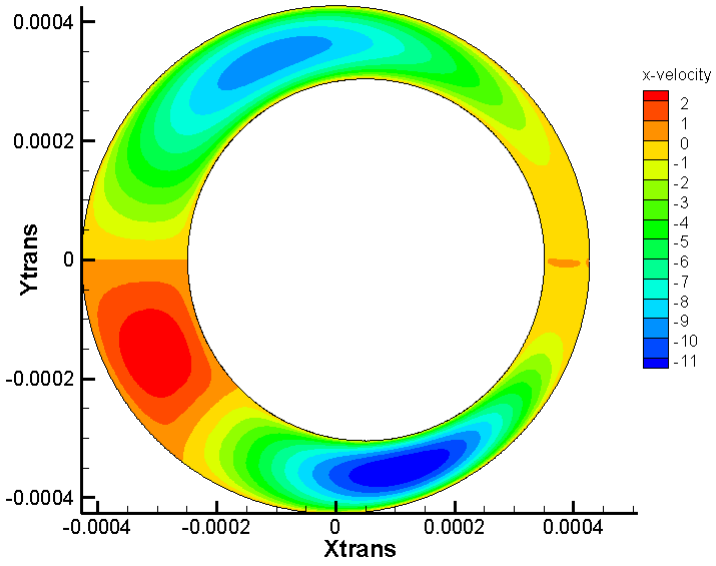

Figure 22. Contours of X Velocity, 10X540 RPM

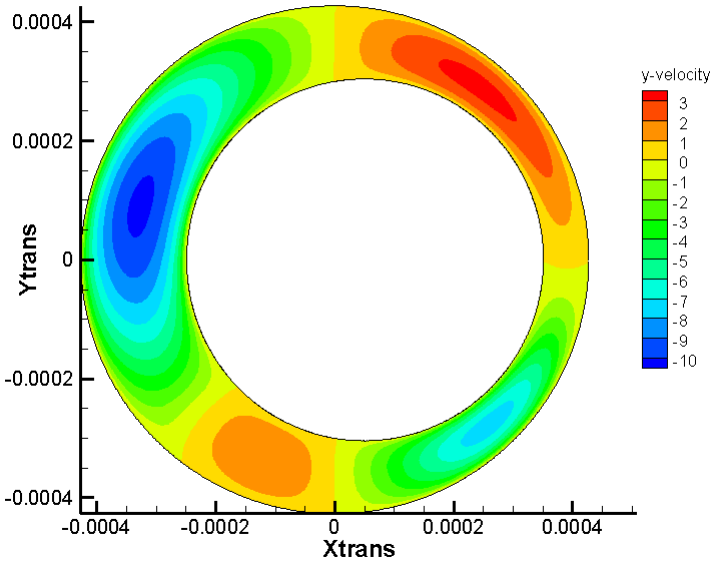

Figure 23. Contours of Y Velocity, 10X540 RPM

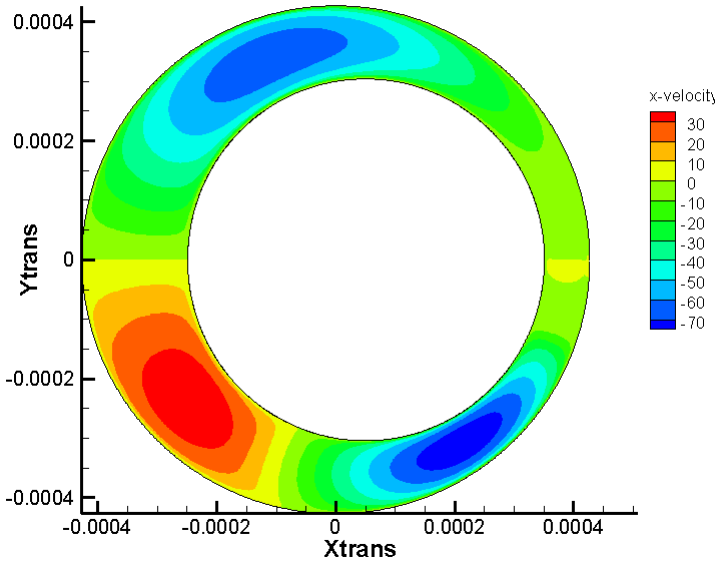

Figure 24. Contours of X Velocity, 50X540 RPM

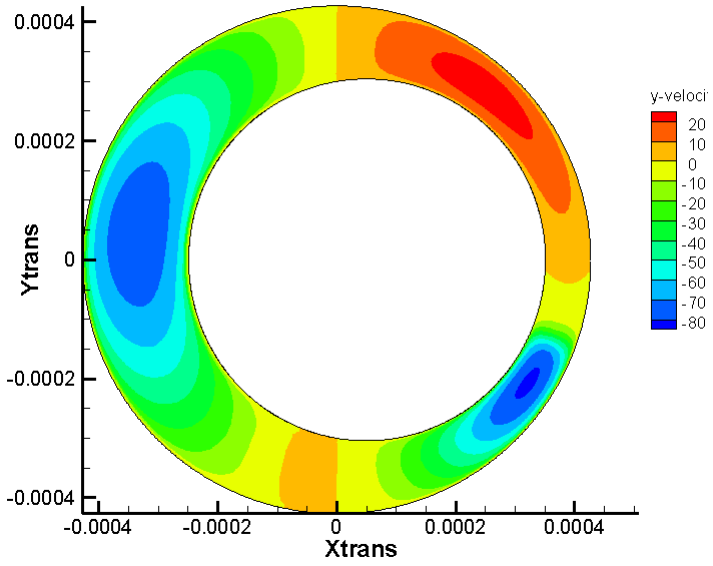

Figure 25. Contours of Y Velocity, 50X540 RPM

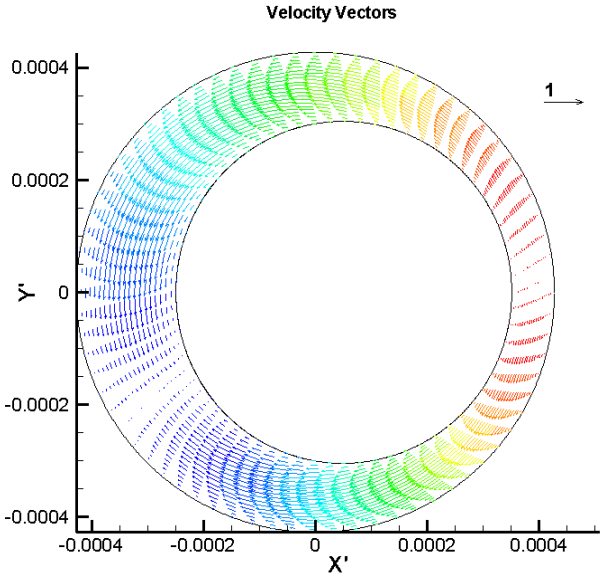

Figure 26. Velocity Vectors, No-cavitation Case 1X540 Rotor Whirl RPM

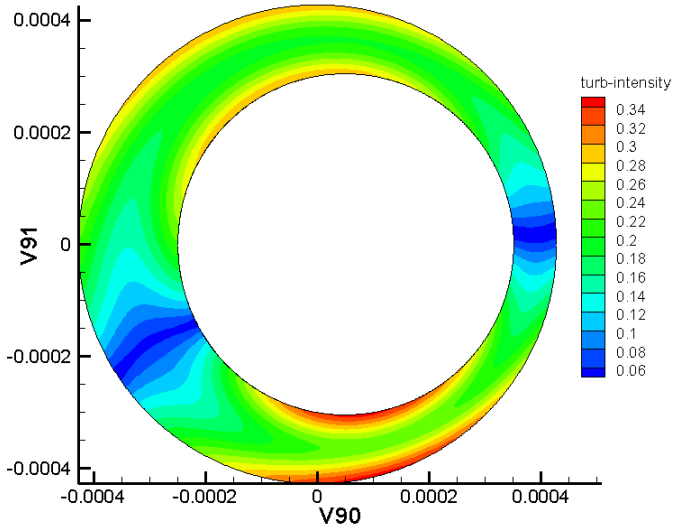

Figure 27. Contours of Turbulence Intensity, No-cavitation Case,1X540 Rotor Whirl RPM

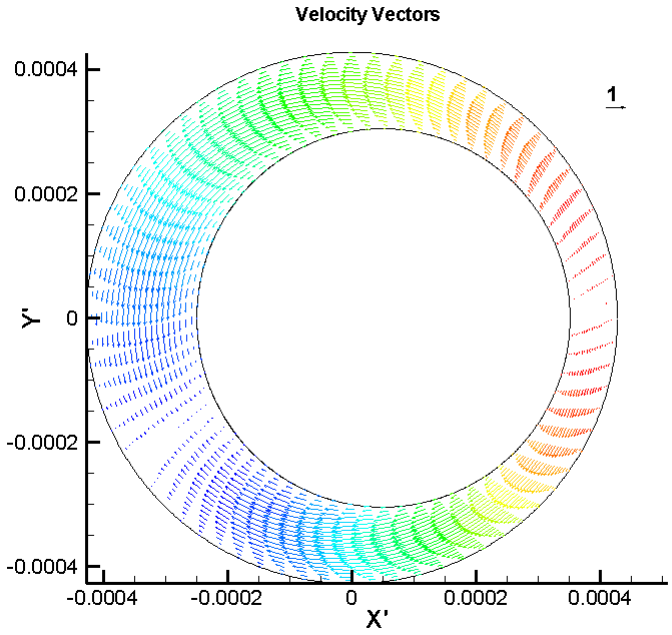

Figure 28. Velocity Vectors, No-cavitation Case 2X540 Rotor Whirl RPM

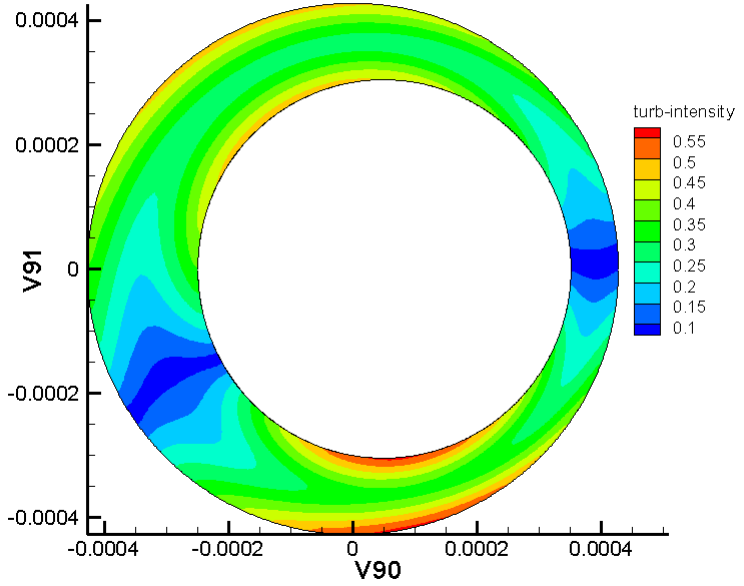

Figure 29. Contours of Turbulence Intensity, No-cavitation Case, 2X540 Rotor Whirl RPM

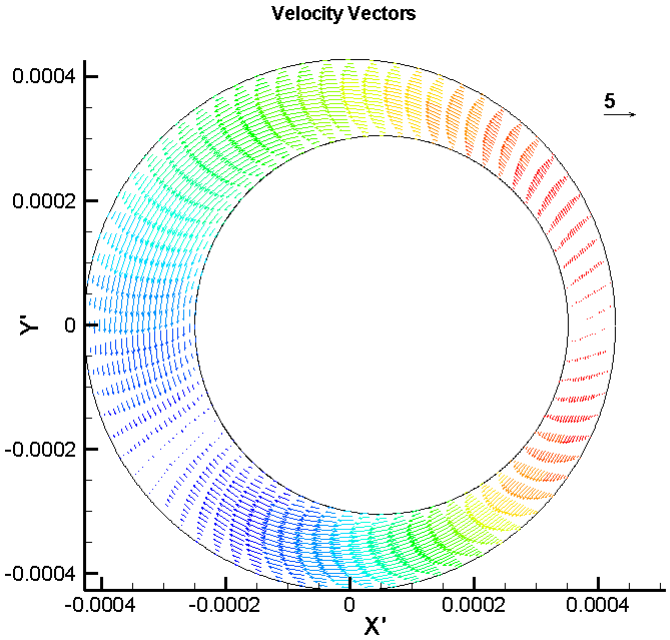

Figure 30. Velocity Vectors, No-cavitation Case 5X540 Rotor Whirl RPM

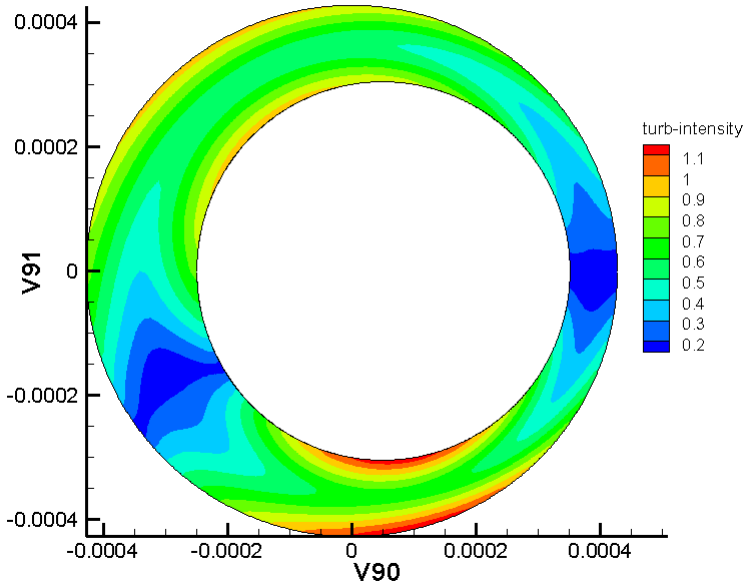

Figure 31. Contours of Turbulence Intensity, No-cavitation Case, 5X540 Rotor Whirl RPM

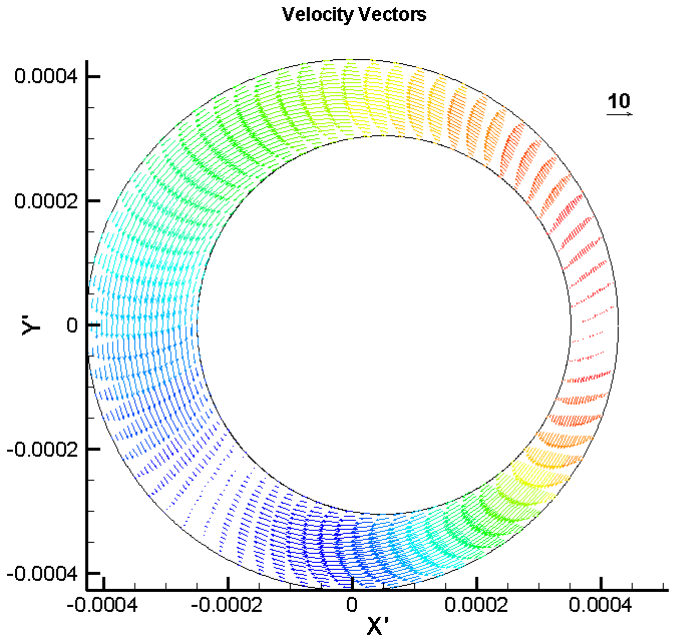

Figure 32. Velocity Vectors, No-cavitation Case 10X540 Rotor Whirl RPM

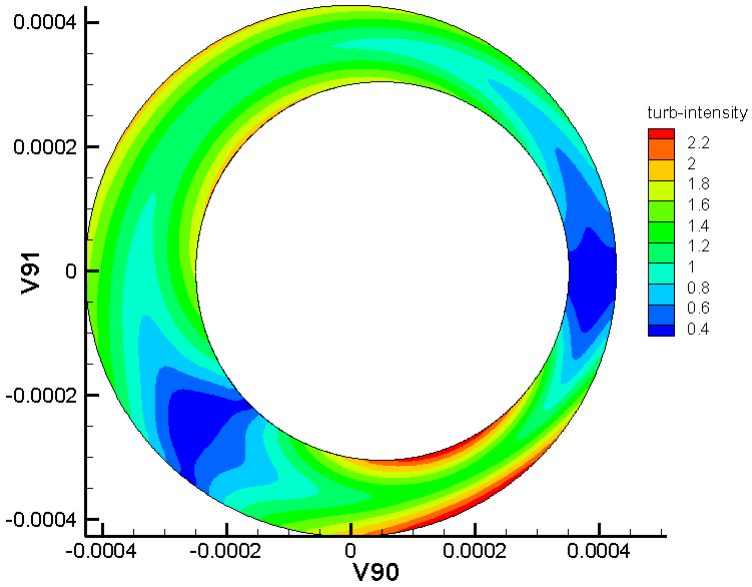

Figure 33. Contours of Turbulence Intensity, No-cavitation Case, 10X540 Rotor Whirl RPM

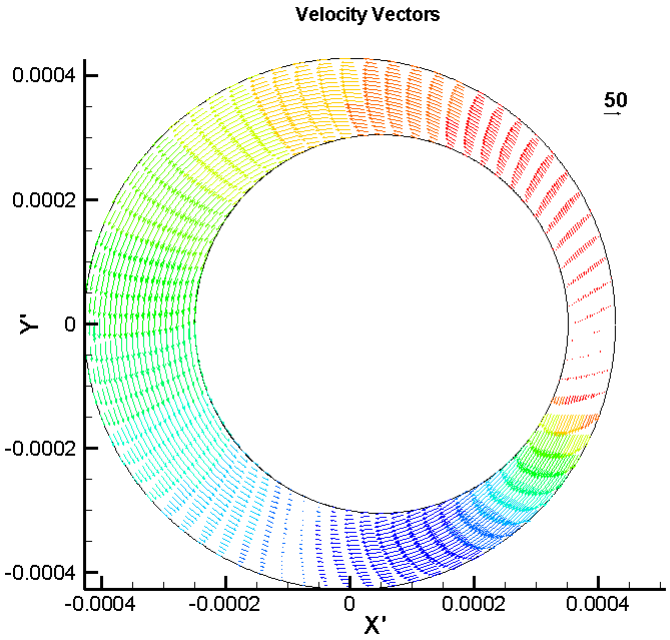

Figure 34. Velocity Vectors, No-cavitation Case 50X540 Rotor Whirl RPM

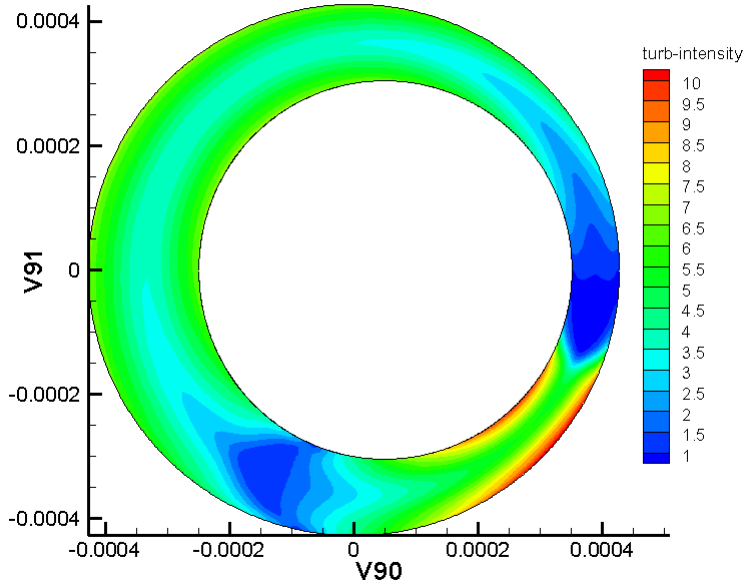

Figure 35. Contours of Turbulence Intensity, No-cavitation Case, 50X540 Rotor Whirl RPM

As mentioned in [1], in fully developed turbulent flows, the velocity profiles do not have the typical parabolic profiles, being almost uniform across the film thickness and with steep gradients close to the wall boundaries, thus forming thin boundary layers. From the vector plots, it can be seen that the velocity profile is parabolic for the lowest shaft whirl speed of 1X540 RPM and begins to flatten at a whirl speed of 2X540. This transition of the velocity profile from the parabolic shape is more pronounced in the maximum clearance region. For higher shaft whirl speeds of 5X540, 10X540 and 50X540 RPM, the velocity profiles are no longer parabolic.

The increasing effect of turbulence can also be observed by studying the contours of Turbulence Intensity. The Turbulent Intensity is the ratio of the Root-Mean-Square (RMS) of the turbulent velocity fluctuations at a particular location over a specified period of time to the average of the velocity at the same location over same time period. The minimum Turbulence Intensity increases from 6% for the lowest whirl speed of 1X540 RPM to 100% for the highest whirl speed of 50X540 RPM. It is also interesting to note that the region of highest Turbulence Intensity is close to the walls on the wake side of the rotor. The region of maximum turbulence intensity occurs at the same location for all rotor speeds but increases in value by almost two orders of magnitude indicating a transition to turbulence.

From the pressure and velocity contours, it can be seen that the pressure distribution changes mainly in magnitude with increase in Rotor speed. The position of maximum and minimum pressure relative to the minimum clearance remains the same except at high Rotor whirl speed where the minimum pressure location rotates counter-

clockwise about 50 degree. This could be attributed to effects of turbulence and inertia effects due to higher velocities. Similarly, the position of maximum and minimum X-velocity and Y-velocity remains same relative to the minimum clearance, as well, except for the highest whirl RPM case. For this case, the location of the maximum X-velocity and Y-velocity shifts by about 20 degree in the counter-clockwise direction.

Table 1. Change in P, Ux, Uy and Uθ with rotor whirl RPM (no cavitation case)

RPM	**Pmax (Pa)**	**Pmin (Pa)**	**Ux_{max} (m/s)**	**Ux_{min} (m/s)**	**Uy_{max} (m/s)**	**Uy_{min} (m/s)**	**$U\theta_{max}$ (m/s)**	**$U\theta_{min}$ (m/s)**
1X540	76070	-4924	0.066	-0.718	0.213	-0.557	0.669	-0.720
2X540	179557	-14750	0.152	-1.598	0.467	-1.211	1.435	-1.604
5X540	659869	-85454	0.542	-4.77	1.311	-3.554	4.103	-4.809
10X540	2490830	-625165	2.745	-12.217	3.301	-10.247	11.182	-13.023
50X540	29709400	-23440300	36.455	-79.897	23.480	-81.740	79.577	-102.45

In Table 1 large negative values of pressure can be observed. The operating pressure is 1 atm. Pressures much below the vapor pressure of oil, are observed since the cavitation model has not been turned on and the flow is incompressible. For incompressible flows, Fluent does not recognize absolute vacuum but only pressures relative to the operating pressure.

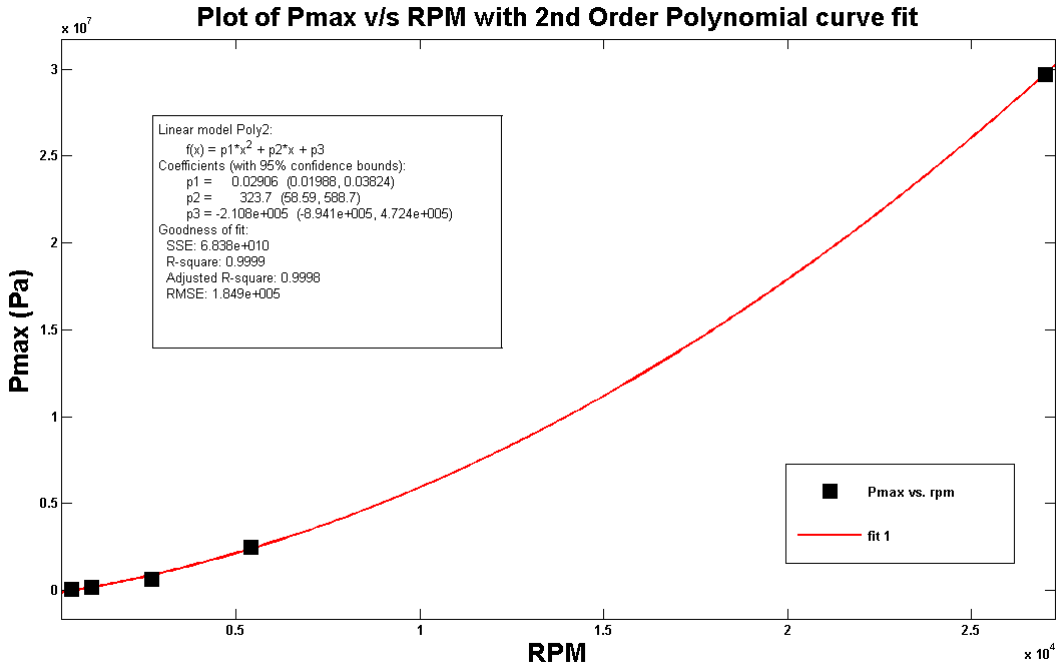

Figure 36. Plot of Maximum Pressure v/s Rotor Whirl RPM and a Corresponding 2nd Order Polynomial Curve Fit

A fairly accurate 2nd Order Polynomial fit is obtained for the maximum positive pressure as it can be seen from Figure 36. Since the pressure distribution varies only in magnitude with the RPM and since the positions of maximum and minimum pressure remain the same with respect to the minimum clearance except at the highest rotor speed, a simple predictive model can be developed to predict the pressure distribution for different RPMs.

The total force (as calculated by Fluent including pressure and viscous drag) acting on the Rotor (Figure 37 through Figure 41) and its line of action, were plotted against the whirl angle for the various whirl speeds. The whirl angle is the measure of

the time since the Rotor began its motion, so these plots illustrate the transient start up of a Squeeze Film Damper, starting from rest. The whirl angle also indicates the location of the minimum clearance. Considering that the SFD domain is divided into four quadrants, the angles are measured from the positive X-axis. The purpose of these plots is to present the transient start-up effects on the pressure filed and how a Quasi-steady solution is reached.

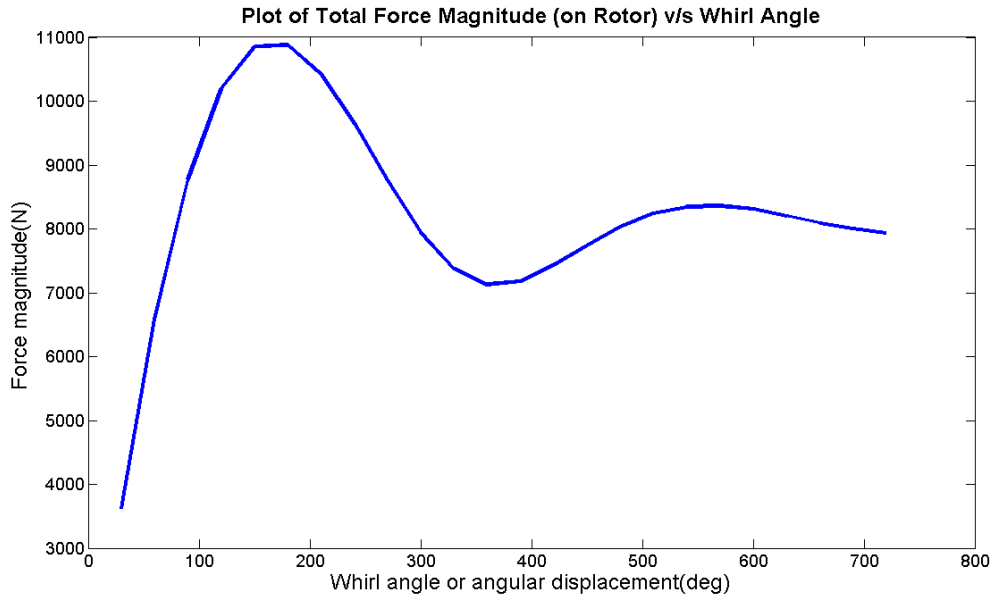

Figure 37. Magnitude of Force on Rotor v/s Whirl Angle (1X540 RPM, No-cavitation Case)

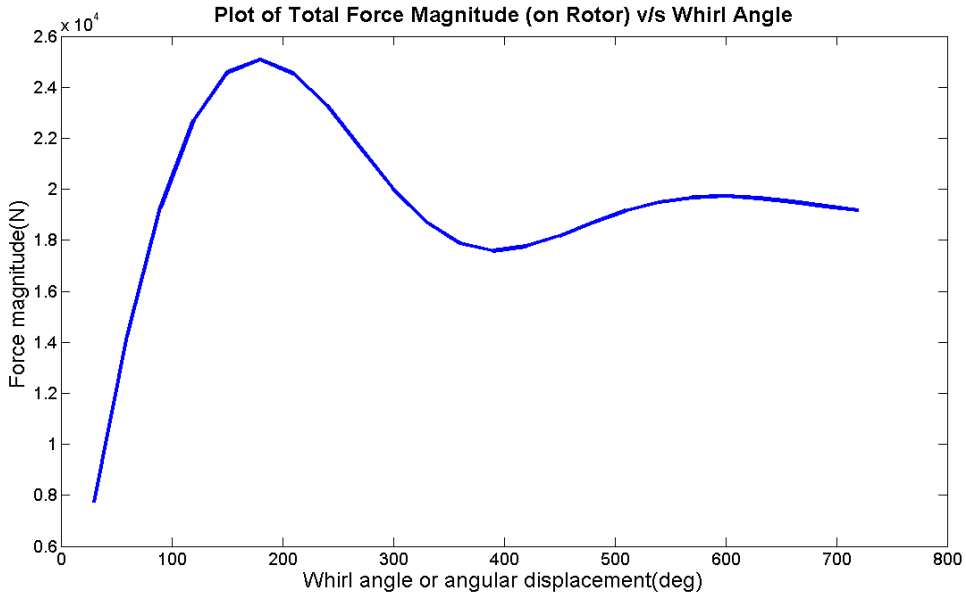

Figure 38. Magnitude of Force on Rotor v/s Whirl Angle (2X540 RPM, No-cavitation Case)

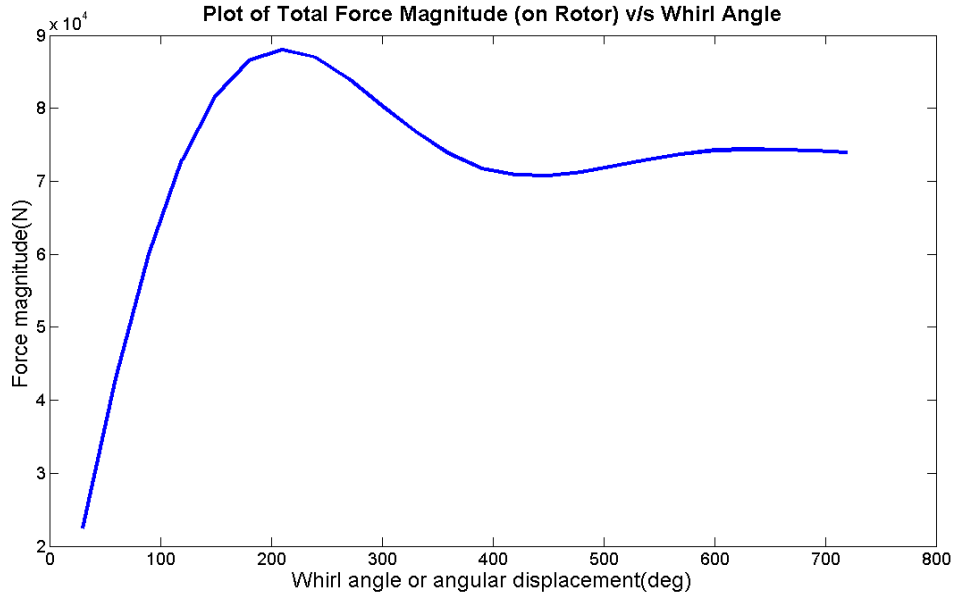

Figure 39. Magnitude of Force on Rotor v/s Whirl Angle (5X540 RPM, No-cavitation Case)

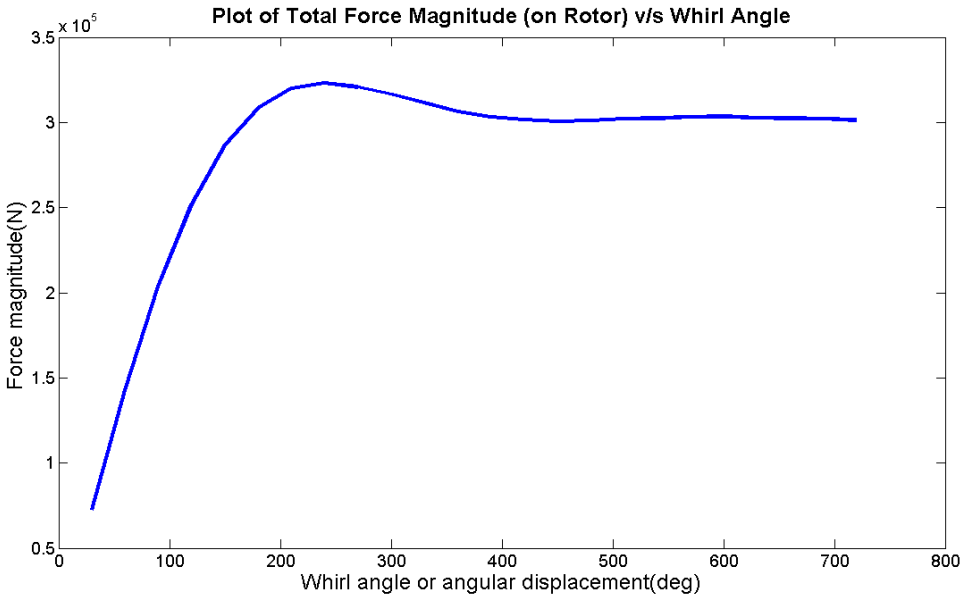

Figure 40. Magnitude of Force on Rotor v/s Whirl Angle (10X540 RPM, No-cavitation Case)

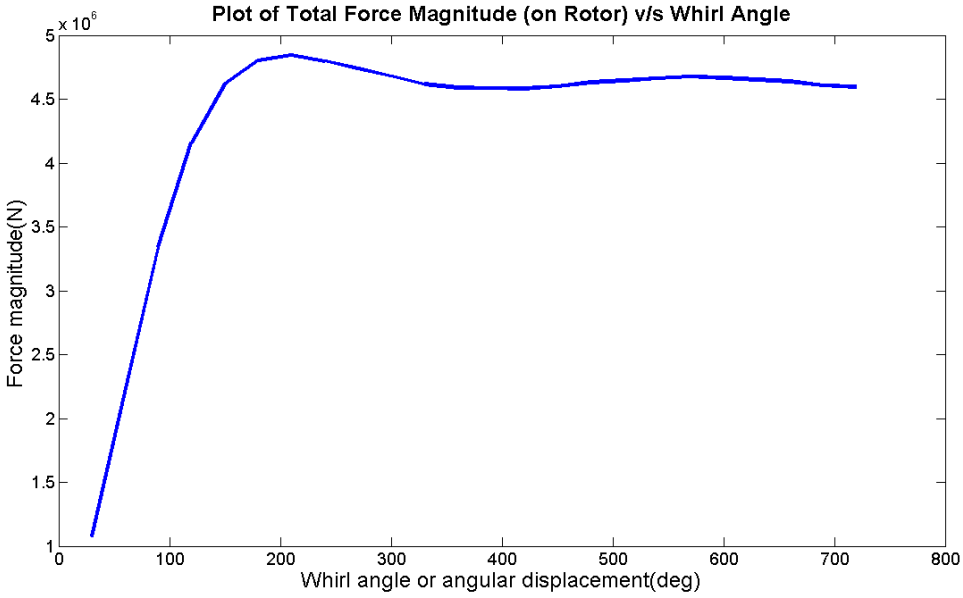

Figure 41. Magnitude of Force on Rotor v/s Whirl Angle (50X540 RPM, No-cavitation Case)

Figure 42 presents the results where the force has been normalized by the steady state value to facilitate easy comparison between the different rotation rates. From the plots of magnitude of force on rotor v/s whirl angle, at different RPMs, the following observations are made:

i. The magnitude of force asymptotically tends to a constant value. This is referred to as the quasi-steady state in SFD literature. Once this state is attained, the pressure distribution remains almost unchanged with respect to the minimum clearance.

ii. Upon start up, the total force on the rotor gradually increases to a peak value and oscillates until it reaches almost a steady value at the end of 2 complete revolutions (i.e. whirl angle of 720 degree).

iii. The rate of increase of force from 0 to the peak value (i.e. initial slope) decrease with increase in RPM.

iv. At low RPMs the rotor is under damped and the force magnitude oscillates. As the RPM increases, damping increases, until at 50X540 RPM, there is very little over & undershoot. This becomes apparent from the following plot of the Normalized Force Magnitude (Fmag/ Fmag at quasi-steady state) v/s Whirl angle, for different RPMs.

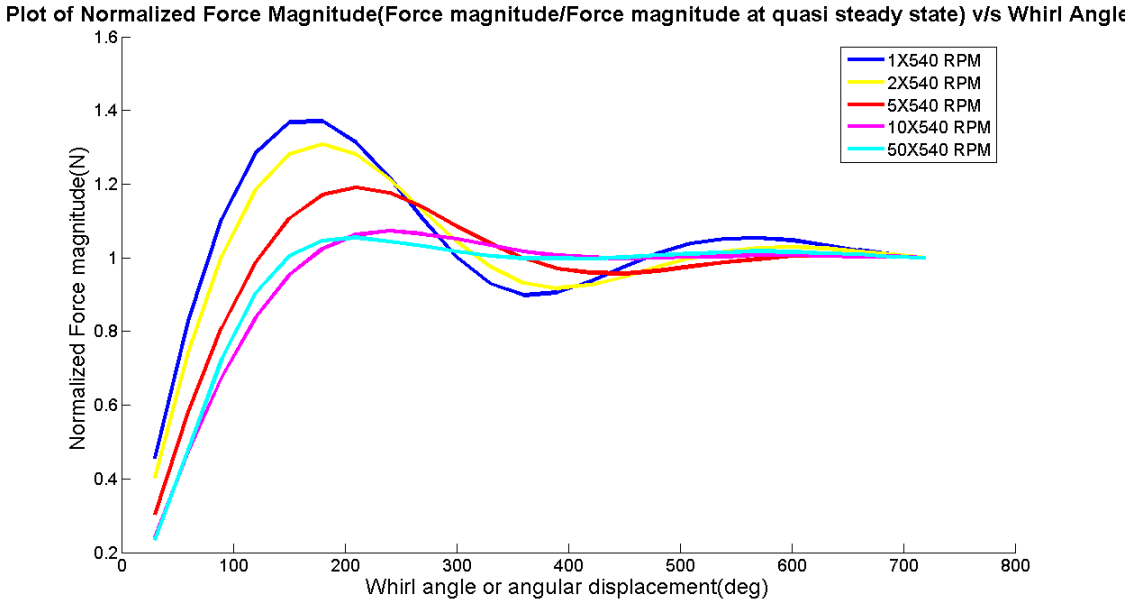

Figure 42. Plot of Normalized Force Magnitude (F_{mag}/ F_{mag} at Quasi-steady State) v/s Whirl Angle for Different Rotor Whirl RPMs

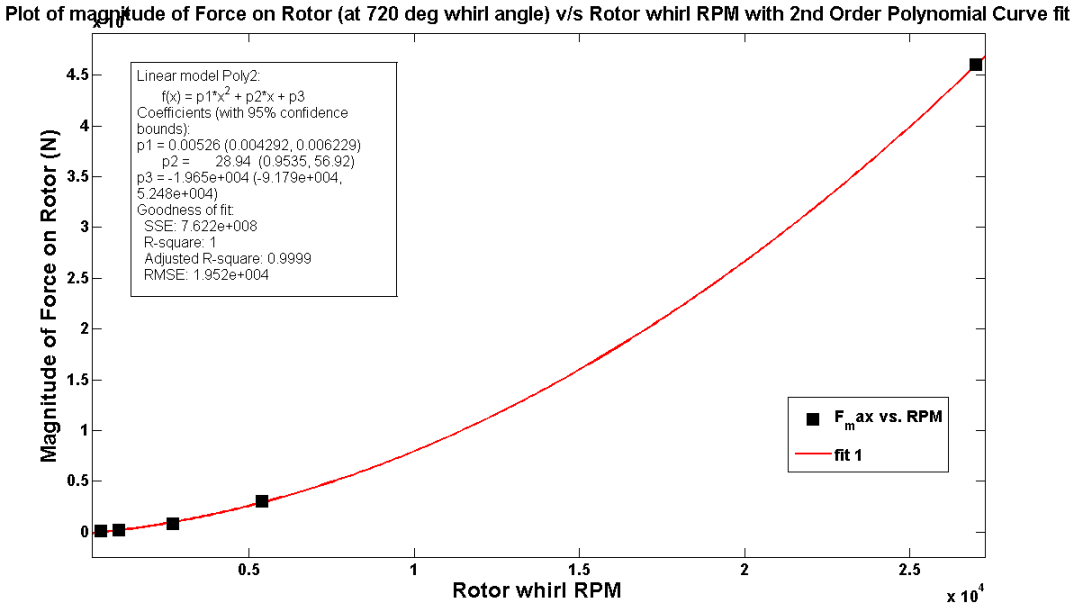

Figure 43. Plot of Force Magnitude at Quasi-steady State v/s Rotor Whirl RPM and a Corresponding 2nd Order Polynomial Curve Fit

It can be seen that the Maximum pressure and Magnitude of total force on rotor, follow a similar trend with increase in the rotor whirl RPM. To confirm this (Magnitude of force at quasi-steady state/P_{max}) was plotted against the rotor whirl RPM. It was observed that the ratio varies between a narrow range of 0.1 to 0.16 m^2 (Figure 43 and Figure 44).

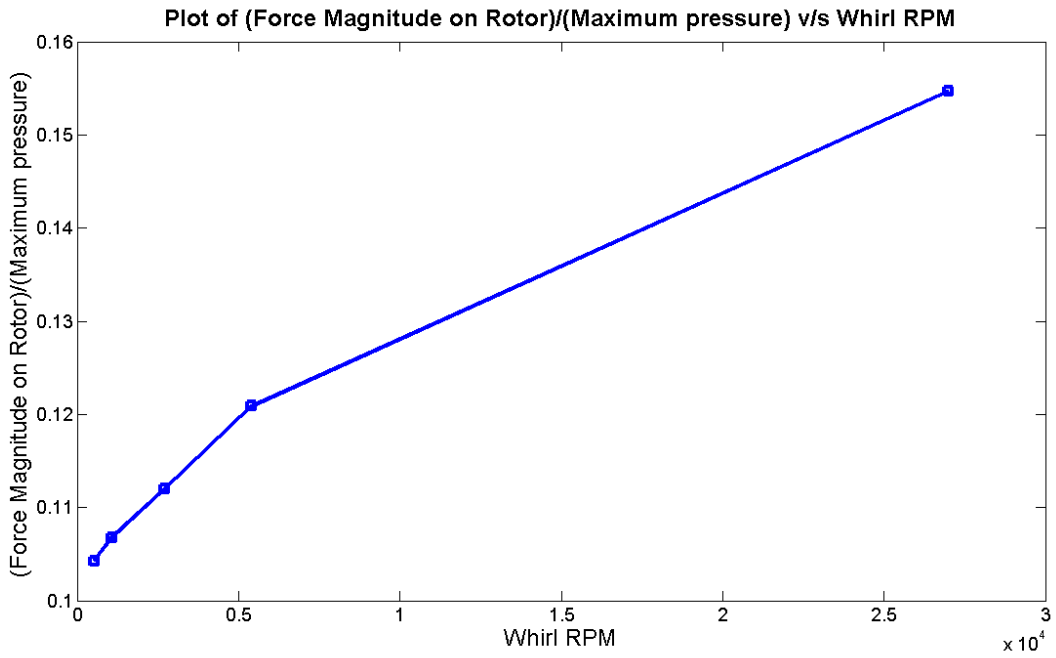

Figure 44. (Magnitude of Force on Rotor/P_{max}) v/s Whirl RPM

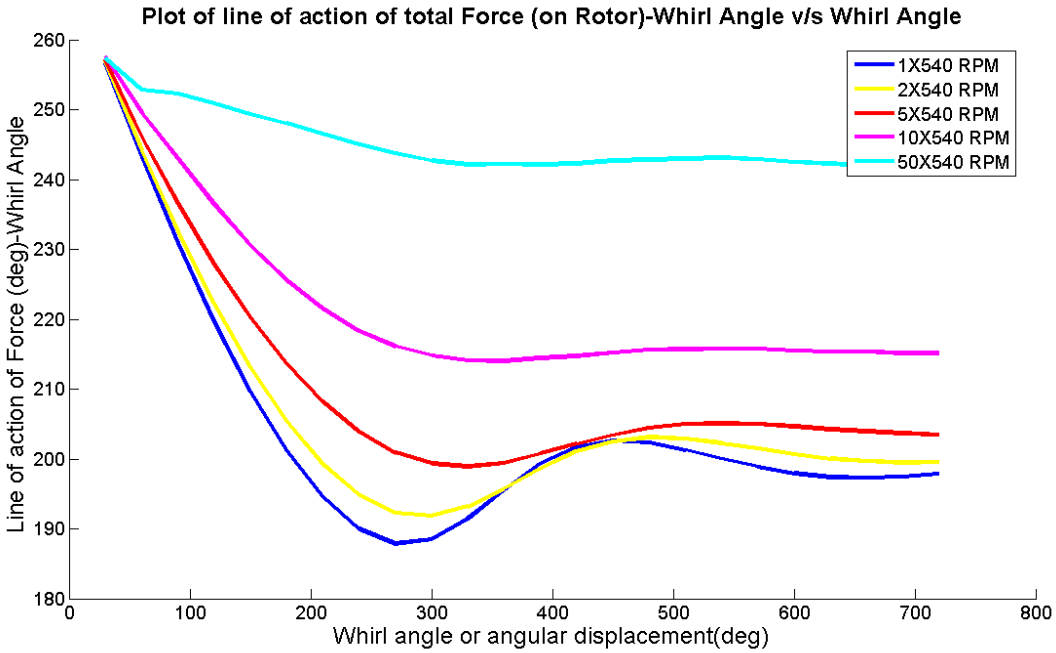

Figure 45. Plot of Line of Action of Force (on Rotor) v/s Rotor Whirl Angle, for Different Rotor Whirl RPMs

Figure 45 shows the change in the line of action of total Force with the whirl of the rotor. The Following observations are made:

i. Similar to the Force Magnitude on the rotor, the line of action of the force too settles to a constant value with respect to the minimum clearance, after the quasi-steady state is reached.

ii. The angle relative to the minimum clearance drops after startup. The rate of decrease of the angle (slope) decreases with increase is RPM. This trend is similar to that noticed for the Magnitude of Force plot.

iii. It can also be seen that as the rotor whirl RPM increases, the aforementioned angle settles to a steady value faster.

iv. The angle of the line of action increases with increasing whirl speed. The largest whirl speed has the largest angle as is the case for force and pressure. This is reflected in the pressure contours.

6.3 2D Case with Cavitation

Subsequently, the mixture model was used to include the effect of cavitation. Cases were run for varying rotation speeds from 540 RPM to 10X540 RPM. The top speed was limited to 10X540 RPM due to numerical instabilities and convergence issues. As per the Fluent User's Guide, for the cavitation model, large ratio of liquid to vapor density and near zero saturation pressures are unfavorable causes for convergence. Both these properties are possessed by the oil used. Initial investigations showed that presence of gas in the SFD is primarily due to dissolved gases coming out of the solution and not a phase change of the oil. The Following are the results for initial static concentrations of 3% and 7% dissolved gases by volume respectively (Figure 46 through Figure 57):

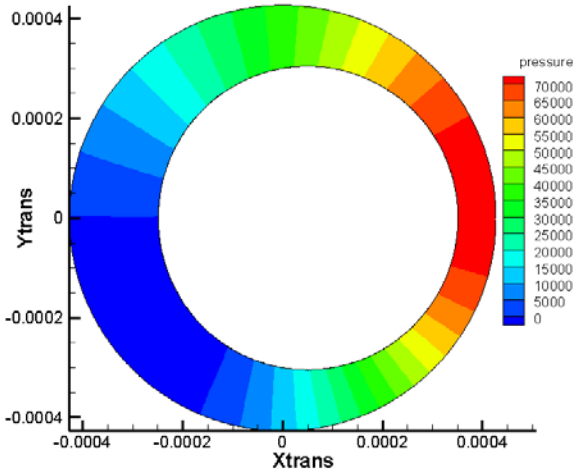

Figure 46. Contours of Pressure, 1X540 RPM, 3% Dissolved Gas

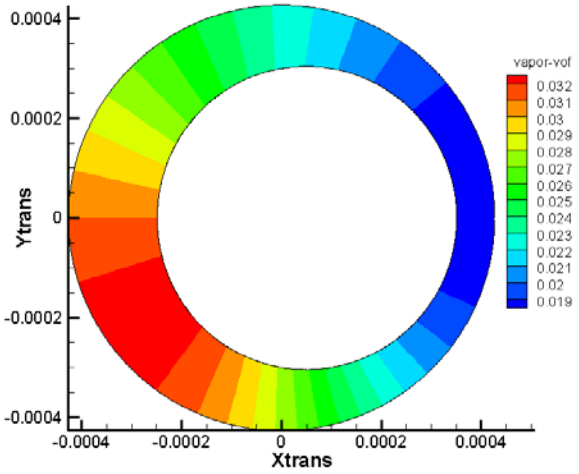

Figure 47. Contours of Volume Fraction of Vapor, 1X540 RPM, 3% Dissolved Gas

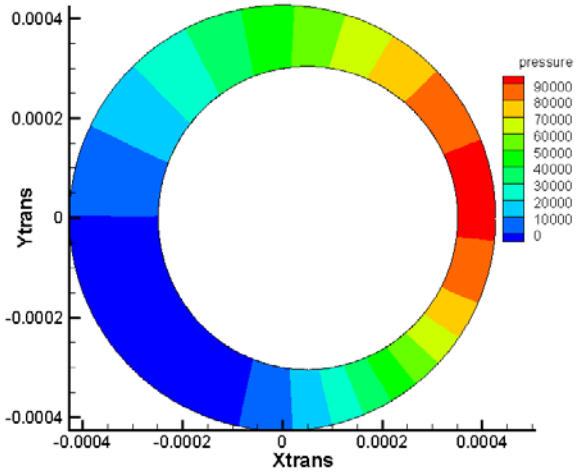

Figure 48. Contours of Pressure, 1X540 RPM, 7% Dissolved Gas

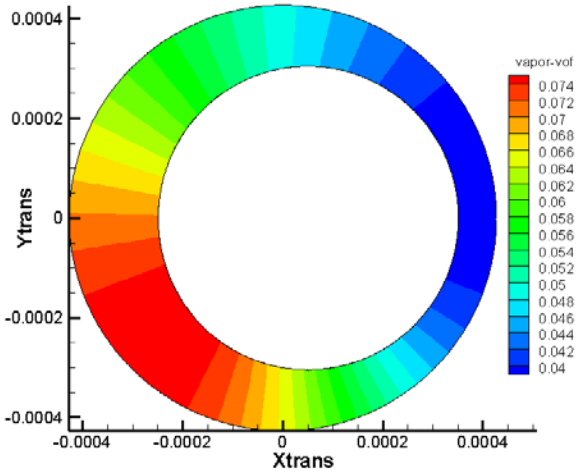

Figure 49. Contours of Volume Fraction of Vapor, 1X540 RPM, 7% Dissolved Gas

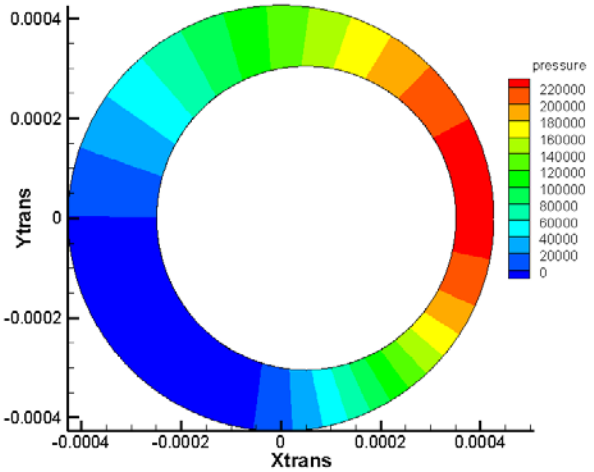

Figure 50. Contours of Pressure, 2X540 RPM, 3% Dissolved Gas

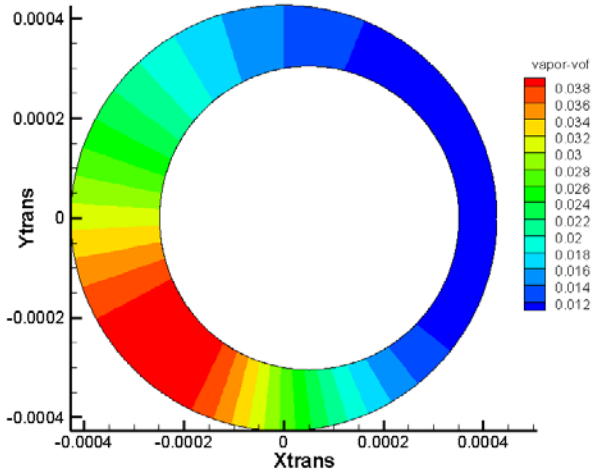

Figure 51. Contours of Volume Fraction of Vapor, 2X540 RPM, 3% Dissolved Gas

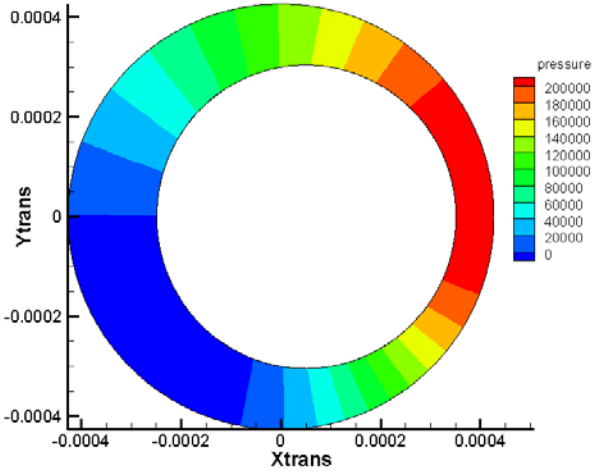

Figure 52. Contours of Pressure, 2X540 RPM, 7% Dissolved Gas

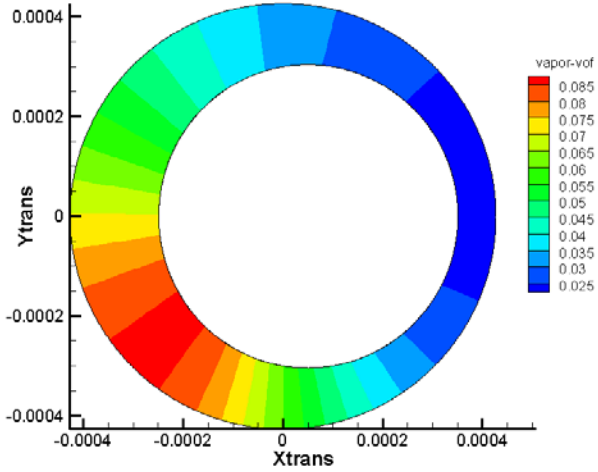

Figure 53. Contours of Volume Fraction of Vapor, 2X540 RPM, 7% Dissolved Gas

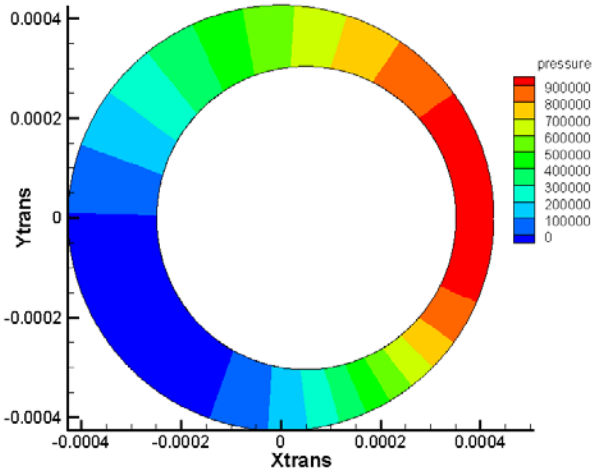

Figure 54. Contours of Pressure, 5X540 RPM, 3% Dissolved Gas

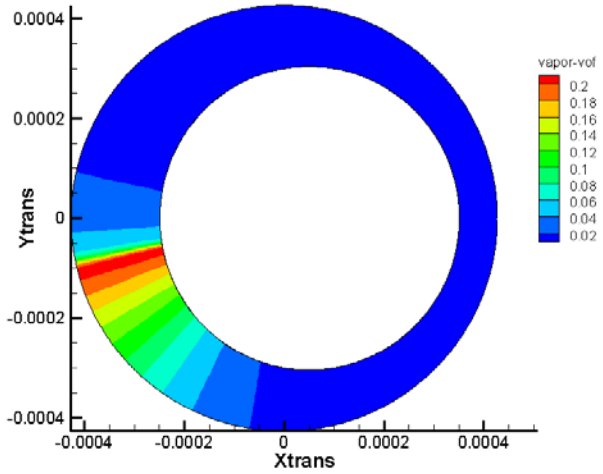

Figure 55. Contours of Volume Fraction of Vapor, 5X540 RPM, 3% Dissolved Gas

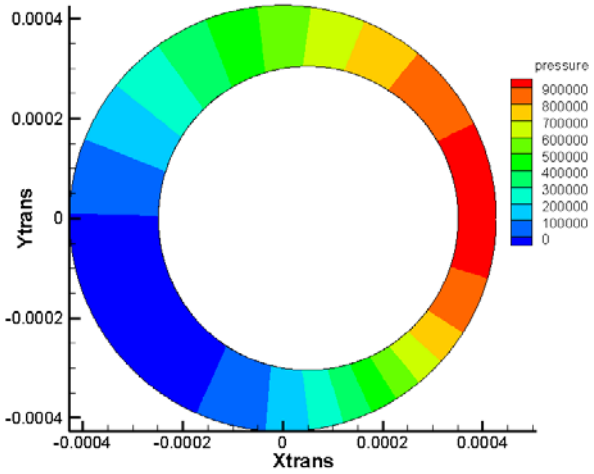

Figure 56. Contours of Pressure, 5X540 RPM, 7% Dissolved Gas

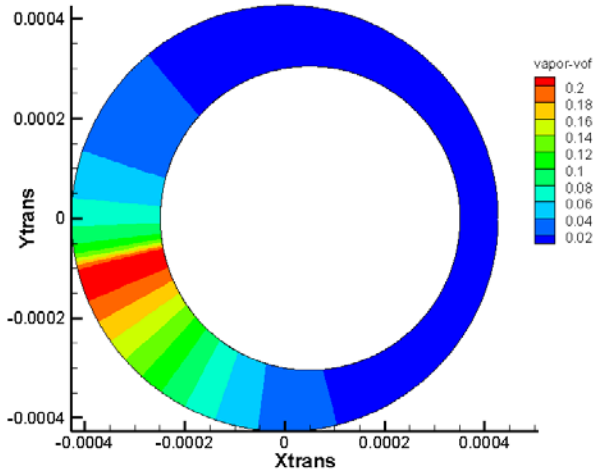

Figure 57. Contours of Volume Fraction of Vapor, 5X540 RPM, 7% Dissolved Gas

From the above plots, it can be seen that the pressure distribution in the clearance, for different RPMs, remains the same relative to the minimum clearance position. This is similar to the previous case without cavitation. Moreover, the position of minimum and maximum pressure with respect to the minimum clearance is the same as the 'No cavitation' case.

Table 2. Change in P, VOF and Fmag with Rotor Whirl RPM (Oil Cavitation Case)

RPM & dissolved gas (% by vol)	P_{max}(Pa)	P_{min} (Pa)	VOF_{max} (% by vol)	VOF_{min} (% by vol)	Magnitude of Force (N, at Rotor whirl angle 720 degree)
1X540 (3% dissolved gases)	74090	-4849	3.2	1.8	7673
1X540 (7% dissolved gases)	92147	-8007	7.5	3.8	9737
2X540 (3% dissolved gases)	229218	-23729	4	0.9	24935
2X540 (7% dissolved gases)	222556	-20126	8.6	2.3	23943
5X540 (3% dissolved gases)	967973	-88900	20.8	0.3	105310
5X540 (7% dissolved gases)	934533	-73528	21.6	0.7	100940

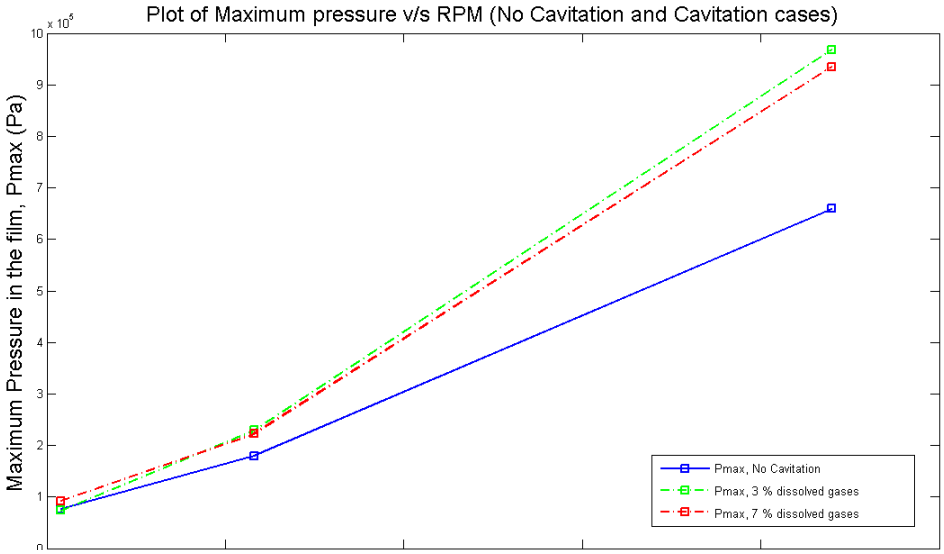

Figure 58. Comparison of Maximum Pressure, P_{max} in the Film for Cavitation and No Cavitation Cases for Different Rotor Whirl RPMs

Larger amounts of cavitation occur at larger RPMs (refer Table 2). This is due to the fact that at higher RPMs the values of P_{min} are more negative (i.e. below the 1 atm operating pressure). The maximum pressure and consequentially the total force exerted on the Rotor, increase with the cavitation occurrence (Figure 58). The contour plots of pressure & volume fraction of vapor comparing the pressure filed for the No cavitation, 3% dissolved air case and 7% dissolved air case illustrate this. The values of P_{max} and P_{min} are higher and the pressure zones are wider for the cavitation cases giving rise to a larger net force on the rotor. The increase in pressure can be attributed to the rise in local pressure due to the collapse of gas bubbles in high pressure zones. P_{min} values are less negative for the cavitation cases since this represents an actual scenario in which P_{min}

will not fall below the saturation vapor pressure of the oil until all the liquid has undergone a phase change and vaporized.

Figure 58 compares the values of P_{max} for cavitating and non-cavitating cases. The effect of the concentration of non-condensable gases on P_{max} is negligible since the two curves for 3% and 7% dissolved non-condensable gases lie almost exactly on top of each other. The difference between P_{max} for the no-cavitation and cavitation cases, increases with whirl RPM to a maximum of almost 50% larger P_{max} for the cavitation case at the highest whirl RPM.

When starting from a static condition, the pressure field in the SFD clearance is expected to stabilize and attain a quasi-steady state after a few initial rotations. This is verified with the following plots of the pressure and vapor fraction as a function of time and angle. The 1X540 rotor RPM case was chosen. As the time-step progresses, the high and low pressure zones linearly move along the circumferential direction with the minimum clearance.

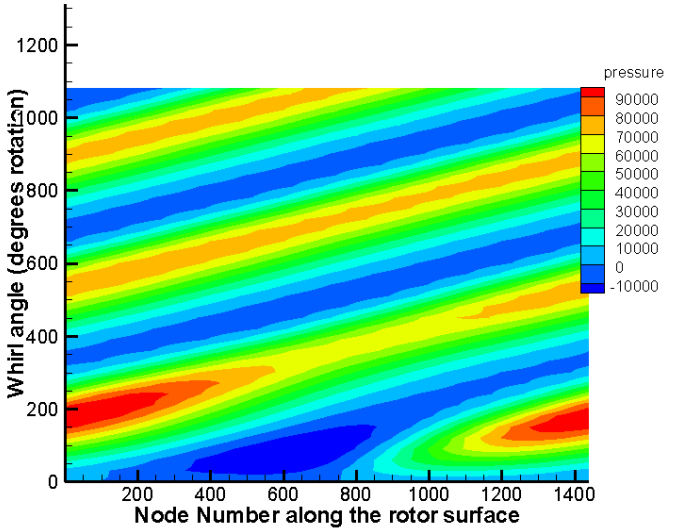

Figure 59. Pressure Stabilization Plot

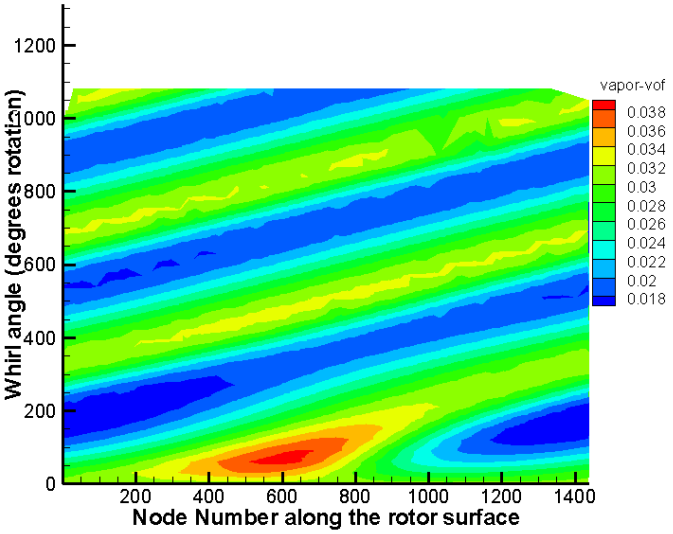

Figure 60. Vapor Fraction Stabilization Plot

From Figure 59, we can see that for the first 200 degree of whirl motion, the pressure variance around the rotor increases with a large high-pressure span. It then decays in amplitude slightly over the next 200 degree after which it recovers in amplitude around 600 degree of whirl angle. It stays relatively steady in amplitude from there on. This trend is similar to that of the total magnitude as observed in subsequent plots.

In the void fraction plot (Figure 60), the high magnitude zones are replaced by low magnitude ones and vice versa, as expected. The void fraction variance around the rotor too, increases for the first 200 degree and then decays up to 400 degree after which it reaches relatively constant amplitude.

6.4 Forces Acting on the Rotor

The total force acting on the Rotor & its line of action, were plotted against the whirl angle & (angle of line of action of force – whirl angle) respectively, for the various whirl speeds and dissolved gas quantities (Figure 61 through Figure 66). Considering that the SFD domain is divided into 4 quadrants, the angles are measured from the positive X-axis. The purpose is to present the transient start-up effects on the pressure filed and how a Quasi-steady solution is reached.

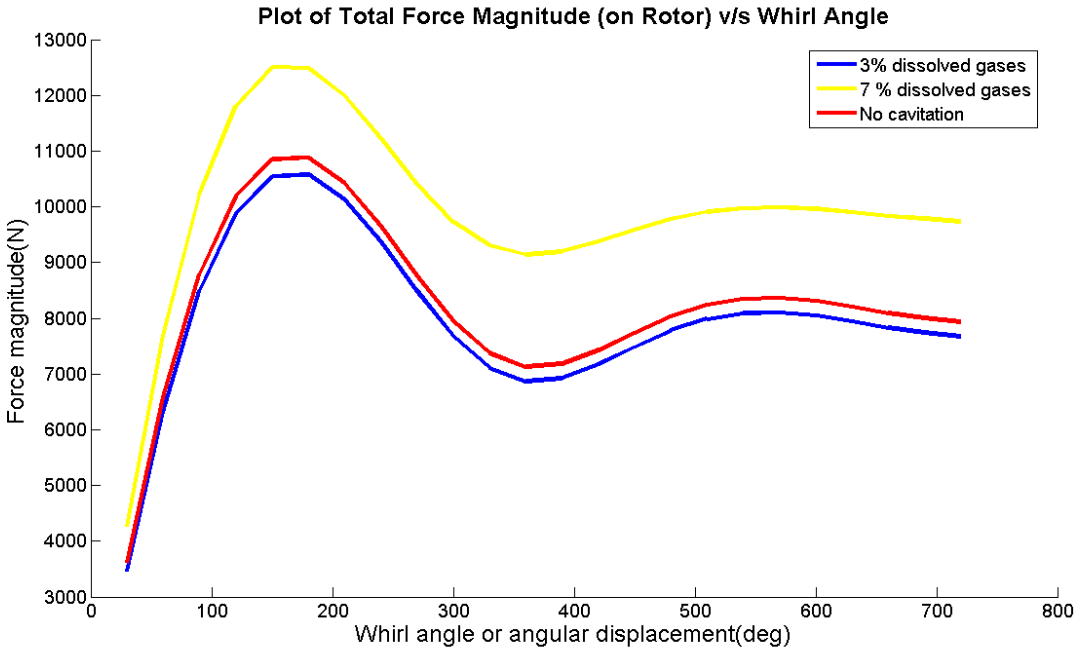

Figure 61. Comparison of Force Magnitude for 1X540 RPM - Different Quantities of Dissolved Gases

The total force exerted on the rotor increases for the cavitation case (consistent with Figure 58 indicating increase in Pmax).

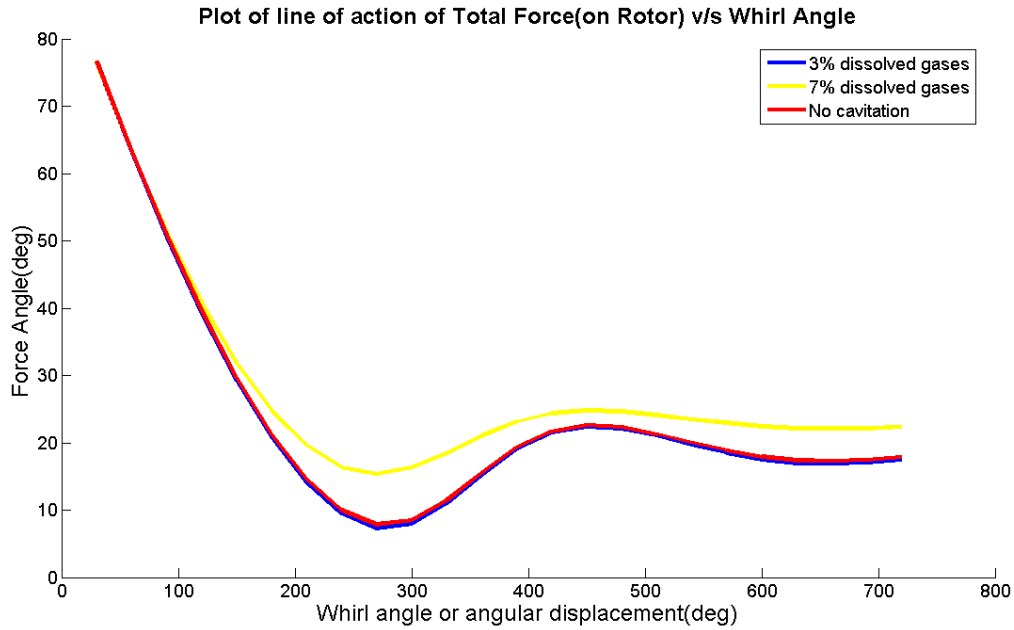

Figure 62. Comparison of (Angle of Line of Action of Force- Whirl Angle) for 1X540 RPM - Different Quantities of Dissolved Gases

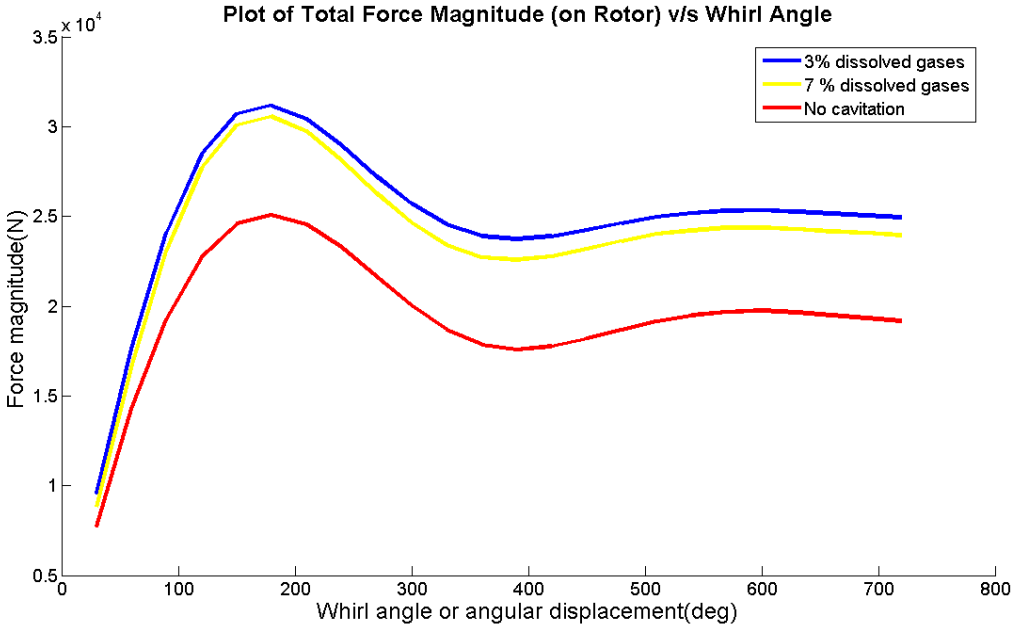

Figure 63. Comparison of Force Magnitudes 2X540 RPM- Different Quantities of Dissolved Gases

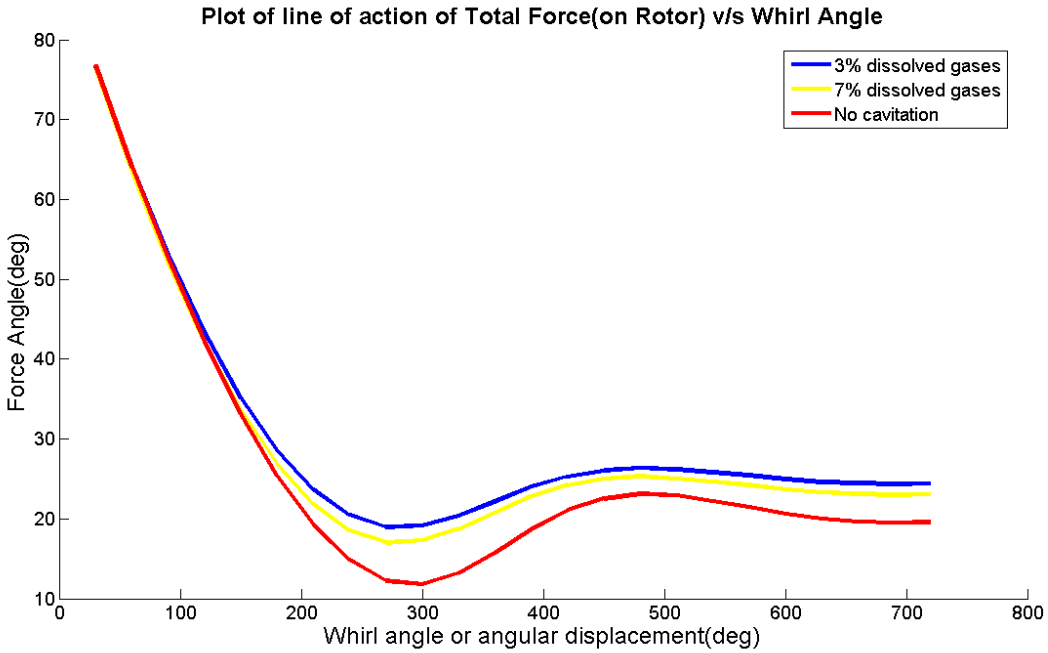

Figure 64. Comparison of (Angle of Line of Action of Force- Whirl Angle) for 2X540 RPM - Different Quantities of Dissolved Gases

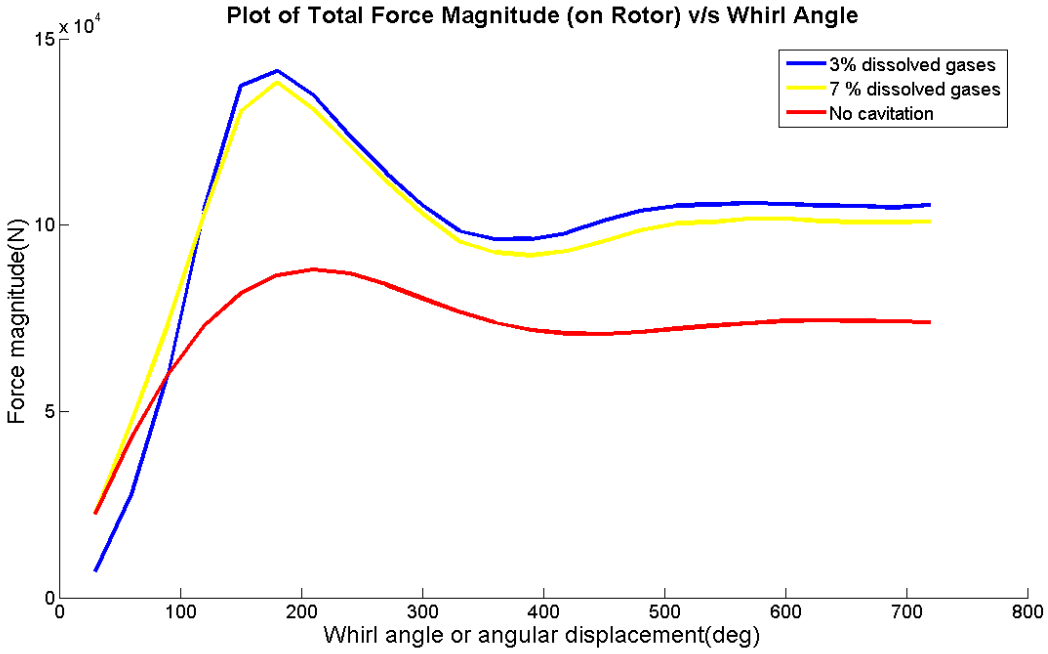

Figure 65. Comparison of Force Magnitudes for 5X540 RPM- Different Quantities of Dissolved Gases

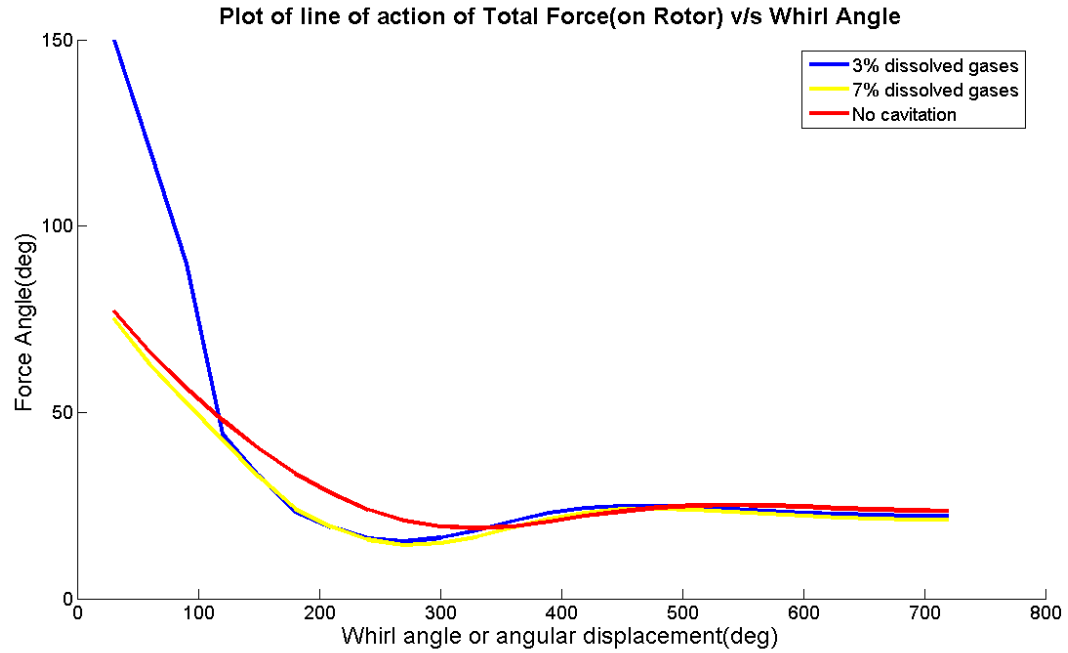

Figure 66. Comparison of (Angle of Line of Action of Force- Whirl Angle) for 5X540 RPM - Different Quantities of Dissolved Gases

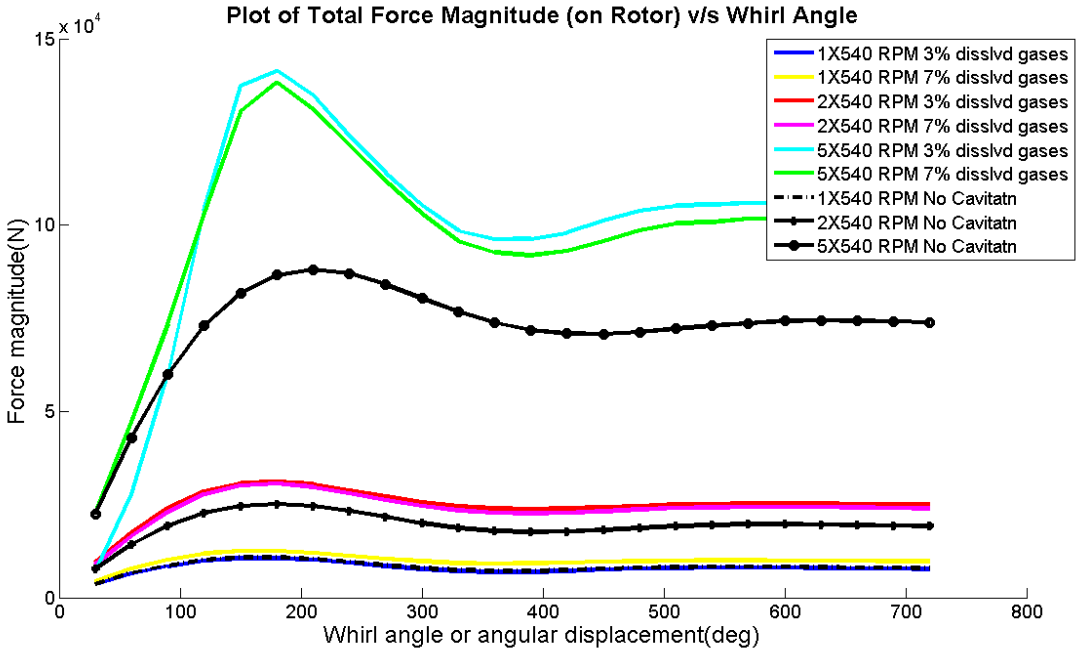

Figure 67. Comparison of Force Magnitudes for Different Rotor Speeds

The force on the rotor increases significantly with the RPM. The Volume fraction of vapor increases significantly with the rotor speed. The vapor bubbles collapse to liquid in the high pressure regions giving rise to large forces on the rotor.

From the plots of magnitude of force on rotor v/s whirl angle (Figure 67), at different RPMs, the following observations are made:

v. Similar to the no-cavitation case, the magnitude of force asymptotically tends to a constant value. This is referred to as the quasi-steady state in SFD literature. Once this state is attained, the pressure distribution remains almost unchanged with respect to the minimum clearance.

vi. Upon start up, the total force on the rotor gradually increases to a peak value and oscillates until it reaches almost a steady value at the end of 2 complete revolutions (i.e. whirl angle of 720 degree).

vii. As with the pressure, the force acting on the rotor is higher for the cavitation case.

viii. The magnitude of force oscillates more (under damped) for the cavitation case than the no-cavitation case. Therefore, it would take longer for the quasi-steady state to be reached when cavitation is present.

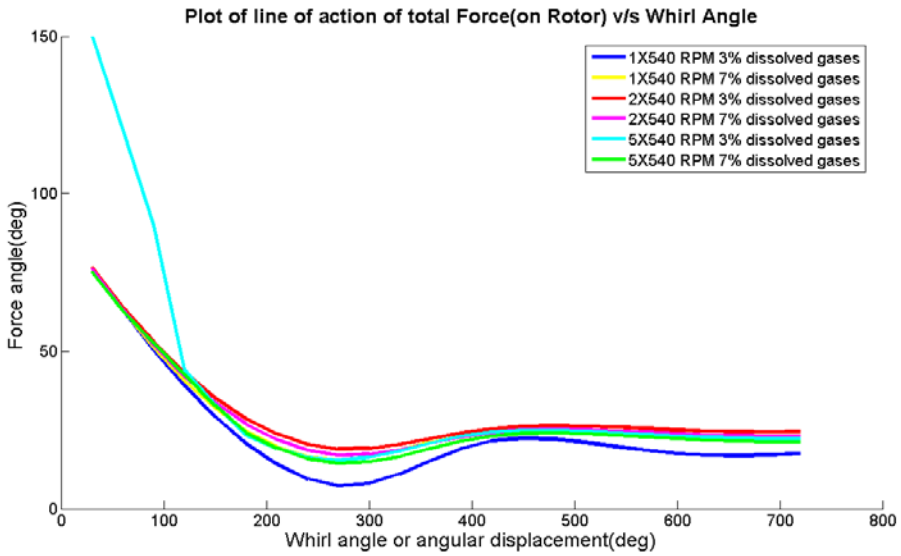

Figure 68. Comparison of (Angle of Line of Action of Force- Whirl Angle) for Different Rotor Speeds

The following observations are made about the line of action of force on rotor (Figure 68):

ix. Similar to the Force Magnitude on the rotor, the line of action of the force also settles to a constant value with respect to the minimum clearance, after the quasi-steady state is reached.

x. The angle relative to the minimum clearance drops after startup. The rate of decrease of the angle (slope) decreases with increase is RPM. This trend is similar to that noticed for the magnitude of force plot.

xi. It can also be seen that as the rotor whirl RPM increases, the aforementioned angle settles to a steady value faster.

6.5 Operating Pressure Variation Cases (Water as Working Fluid)

It can be seem from the Oil Cavitation cases discussed in the previous section, that the maximum percentage Volume fraction of vapor was about 21% for the 5X540 RPM case with 7% dissolved gases by volume. Typically larger amounts of vapor fractions are observed for comparable speeds. There are 3 different sources of the vapor. These are:

xii. Non condensable dissolved gases in the liquid.

xiii. True phase change cavitation occurring due to the local pressure dropping below the vapor pressure of the liquid.

xiv. Gas ingestion into the SFD i.e. sub-atmospheric pressures causing the gases to leak into the SFD.

Therefore it was decided to study the effect of variation of Operating pressure on the Volume fraction of vapor. As per the Fluent User's Guide, the cavitation model accounts for all first-order effects i.e., phase change, bubble dynamics, turbulent pressure fluctuations, and non-condensable gases. Water was chosen as the working medium for this study since the properties like vapor pressure, surface tension, density, thermodynamic properties are established for both liquid and gaseous phase of water. Moreover, the vapor pressure of water (3168 Pa at 298K) is much larger than the vapor pressure of Mobile Velocite 3 oil (13.3 Pa). This allows more phase change cavitation to occur so that its effect can be observed (Figures 69 through Figure 76).

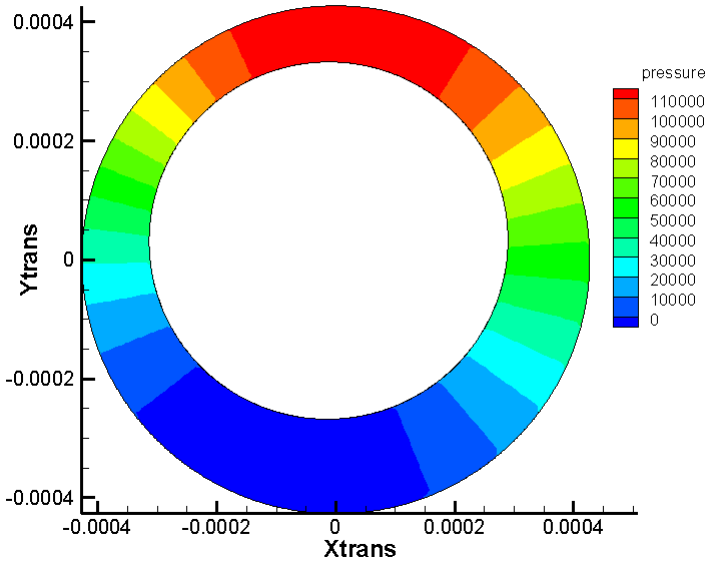

Figure 69. Contours of Pressure, Operating Pressure 90 kPa, Operating Speed 1X540 RPM

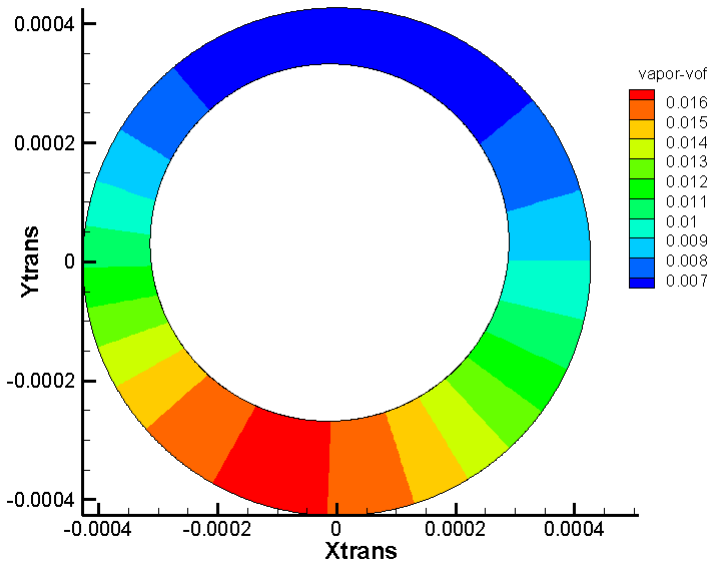

Figure 70. Contours of Vapor Fraction, Operating Pressure 90 kPa, Operating Speed 1X540 RPM

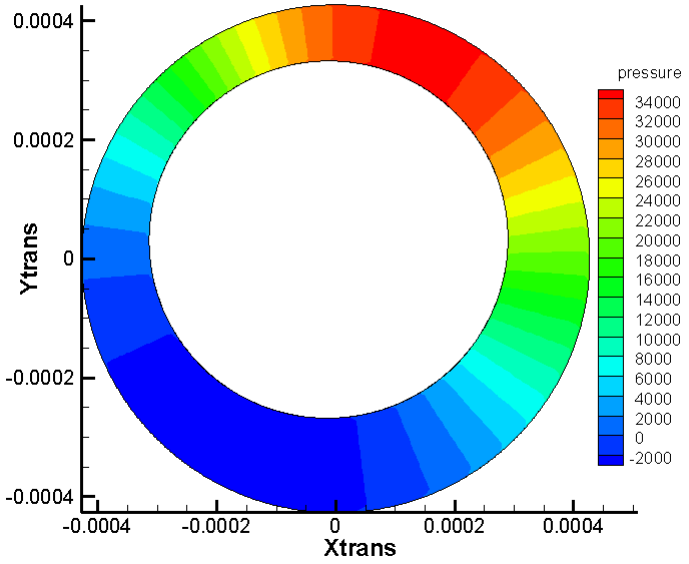

Figure 71. Contours of Pressure, Operating Pressure 20 kPa, Operating Speed 1X540 RPM

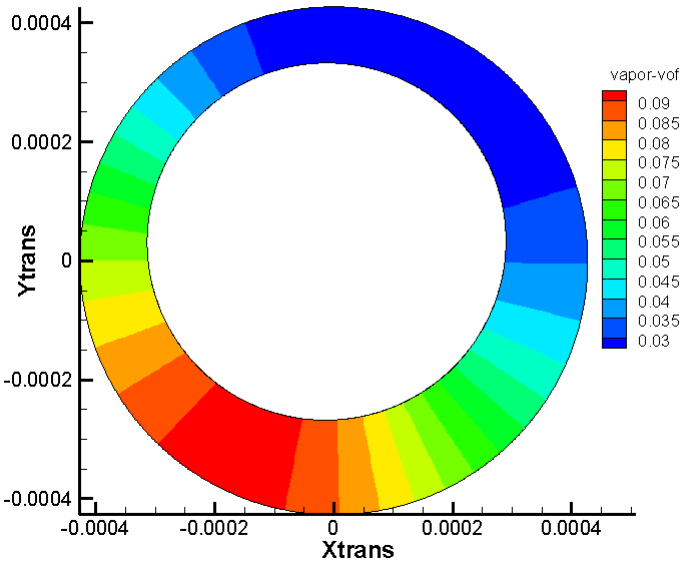

Figure 72. Contours of Vapor Fraction, Operating Pressure 20 kPa, Operating Speed 1X540 RPM

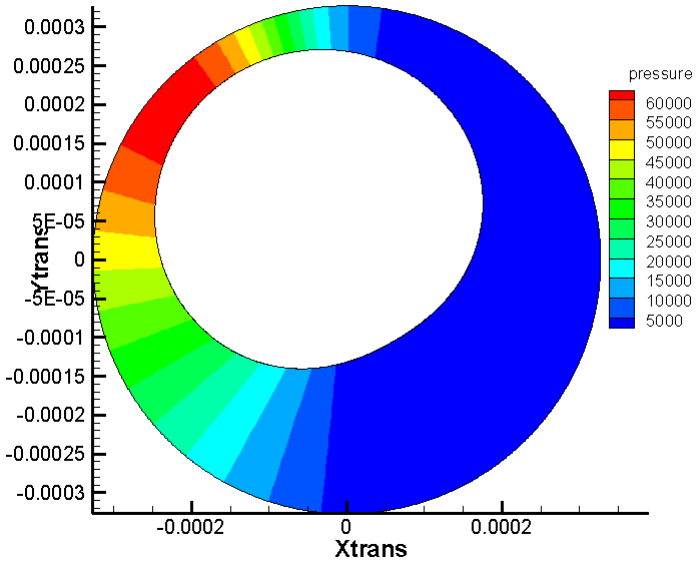

Figure 73. Contours of Pressure, Operating Pressure 5 kPa, Operating Speed 1X540 RPM

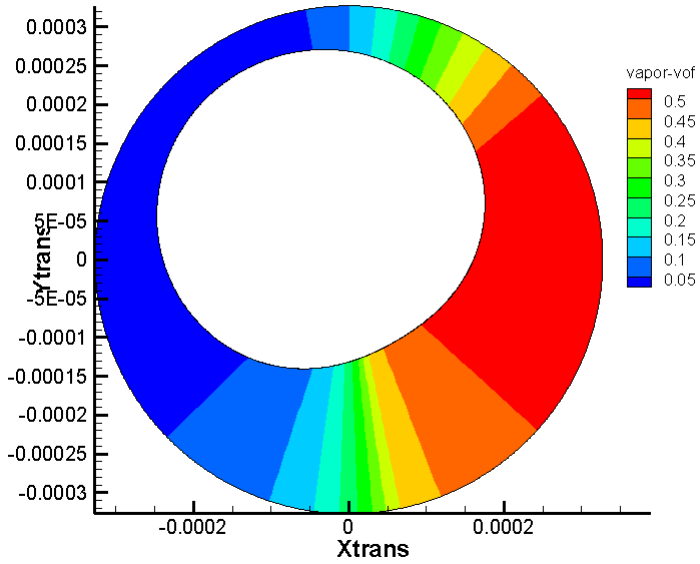

Figure 74. Contours of Vapor Fraction, Operating Pressure 5 kPa, Operating Speed 1X540 RPM

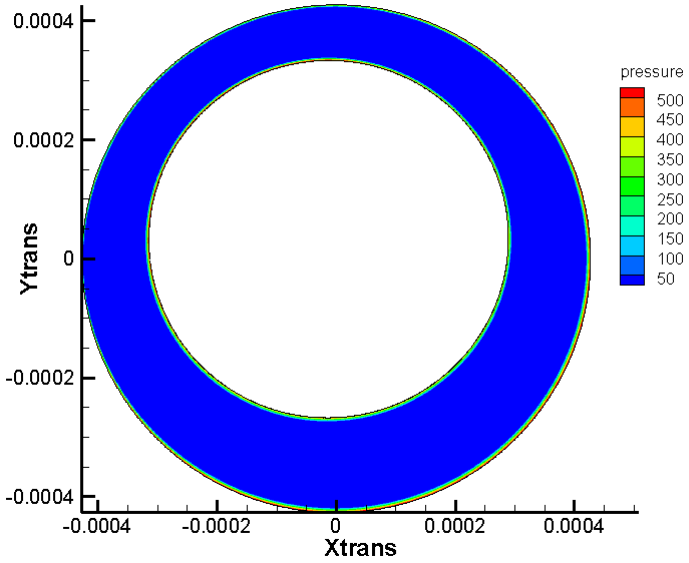

Figure 75. Contours of Pressure, Operating Pressure 3 kPa, Operating Speed 1X540 RPM

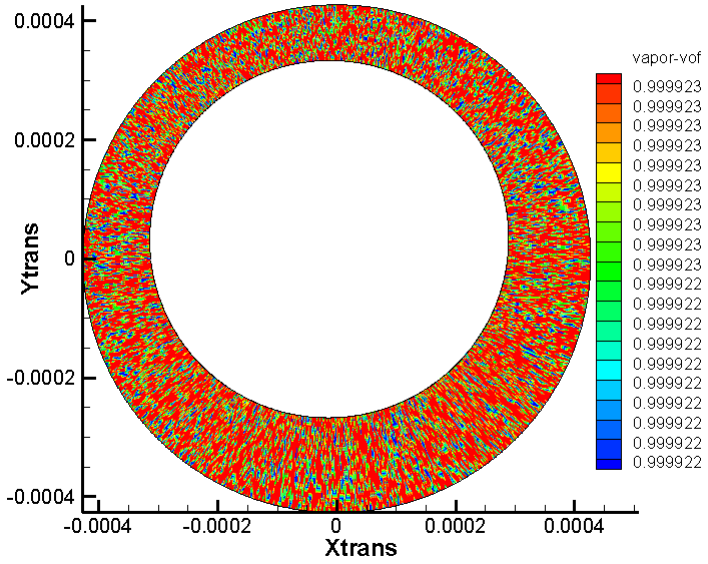

Figure 76. Contours of Vapor Fraction, Operating Pressure 3 kPa, Operating Speed 1X540 RPM

Starting from 1 atm, the operating pressure is steadily varied downward to 3 KPa (just below the vapor pressure of water at room temperature). The percentage of vapor by volume increases from 7.5% at operating pressure of 1 atm to about 50 % at 5 kPa operating pressure. When the operating pressure is further reduced below the vapor pressure of water (3168 Pa), almost all the fluid changes phase from liquid to vapor and there is no pressure variation throughout the SFD clearance. This also demonstrates the ability of the mixture-cavitation model to handle large quantities of vapor.

Table 3. Variation of Force Magnitude and Angle with Operating Pressure

Operating pressure (kPa)	Fx (N)	Fy (N)	F_{mag} (N)	(F_{angle}-Min clearance angle)
90	-2140.83	-12696.56	12876	305.43
20	-1870.31	-3338.56	5686	285.74
5	945.38	5607.09	3826	215.42
3	0.00275	-0.0069	0.0074	178.68

It can be seen from Table 3 that the magnitude of force on the rotor reduces with decrease in operating pressure. The angle of line of action of force with respect to the minimum clearance too decreases. It can be seen that for the 3 kPa operating pressure case, the force is negligible. Since this operating pressure is lower than the vapor pressure of water, almost all the water in the domain undergoes phase change and the clearance is filled with vapor.

6.6 Coordinate Transformation Technique

The results discussed in the previous sections were obtained using a transient solver. The rotor is actually made to whirl using mesh deformation. This is very time and

computation intensive. To address this issue, the applicability of a Coordinate Transformation technique was explored. Under this technique, instead of using the dynamic deforming mesh, a coordinate transform was used to convert the problem to a steady state condition by using a Rotating Coordinate frame. A rotational velocity relative to the rotor and stator was assigned to the fluid in the clearance. Thus a steady state non time dependent solution is obtained reducing the required computational resources required. Details of this technique are included in Appendix B.

A large number of iterations were required to obtain a converged solution. However, the solution obtained through this approach did not match that obtained through the previously used transient, deforming mesh approach. As it can be seen from Figure 77 and Figure 78, the pressure distribution from the Coordinate transformation technique is different. The magnitudes of pressure are higher and the position of the high/low pressure zones with respect to the minimum clearance is also different.

As per this technique, the walls were rendered stationary and the fluid domain was assigned a rotational motion. It would be interesting to explore other transformations as well. Therefore, this technique requires more investigation to determine whether it can be used to obtain a steady state solution.

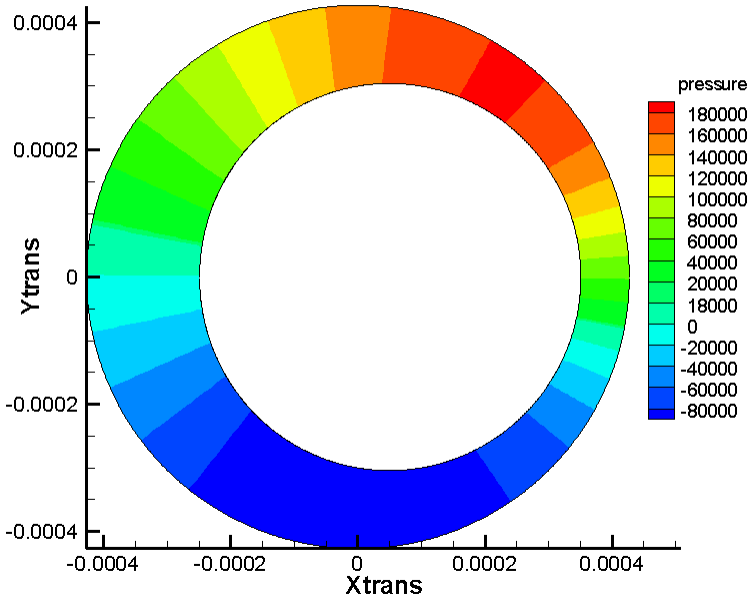

Figure 77. Contours of Pressure, 1X540 RPM- 320,000 Iterations (Steady State Coordinate Transformation Approach)

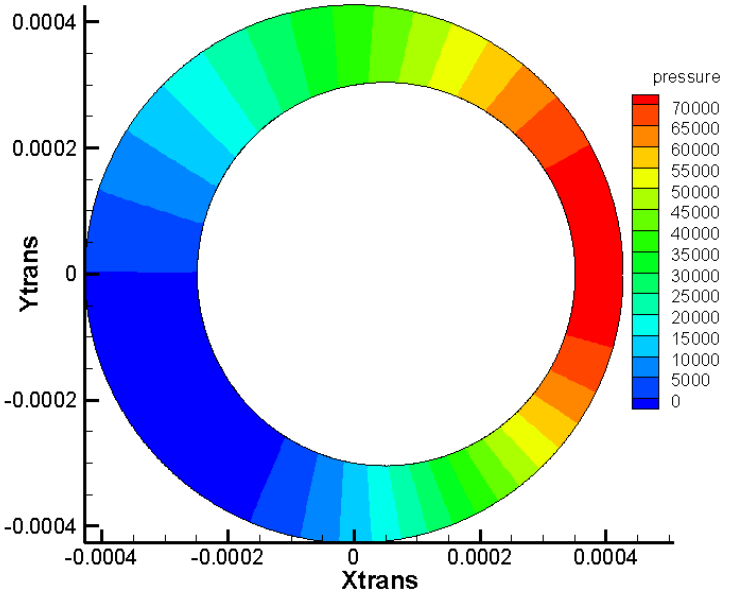

Figure 78. Contours of Pressure, 1X540 RPM- Transient Deforming Mesh Approach

6.7 3D Results

Now that the CFD methodology along with the moving mesh approach, cavitation model, physical phenomenon of phase change cavitation and expansion of non-condensable gases, mesh and time-step requirements etc. had been established, a previously measured, full 3D case was simulated. The case from the studies of Delgado and San Andrés [5] was selected. The simplified geometry of the test rig used by Delgado and San Andrés is represented in Figure 79.

The inner radius of the SFD is 2.5 in (63.5 mm) and the clearance is 5 mil (0.127 mm). The length of the SFD land is 1 in (25.4 mm). The case simulated has 0.074 mm or 60% eccentricity, 50 Hz rotor whirl frequency and a supply pressure of 31 kPa at the inlet section at the top. There is no leakage flow, i.e. 'Section out' at the bottom is sealed without any fluid flowing past it. The lubricant used is Mobil Velocite 3 which possesses a density of 800 kg/m^3, Kinematic Viscosity of 0.0016 kg/m-s (2 cSt) and a low vapor pressure of 1mmHg (13.13 Pa). The operating pressure was maintained at 1 atm. Since the quantity of non-condensable dissolved gases is unknown, it was varied from 1 % to 7% by volume in increments of 2%.

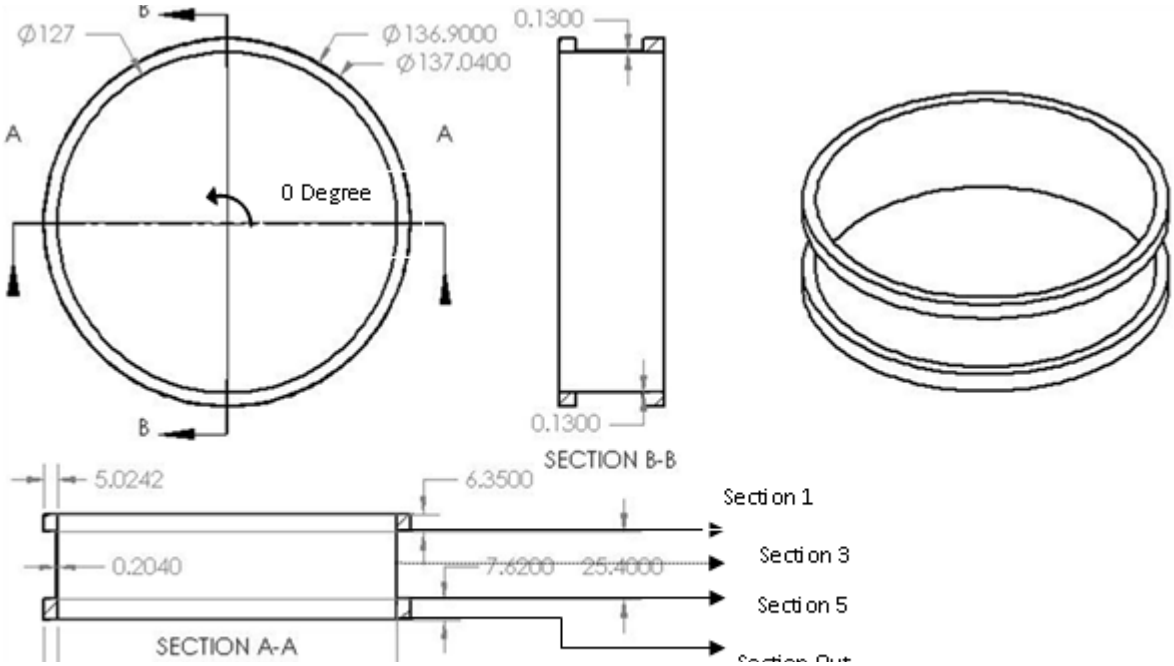

Figure 79. Simplified SFD Geometry

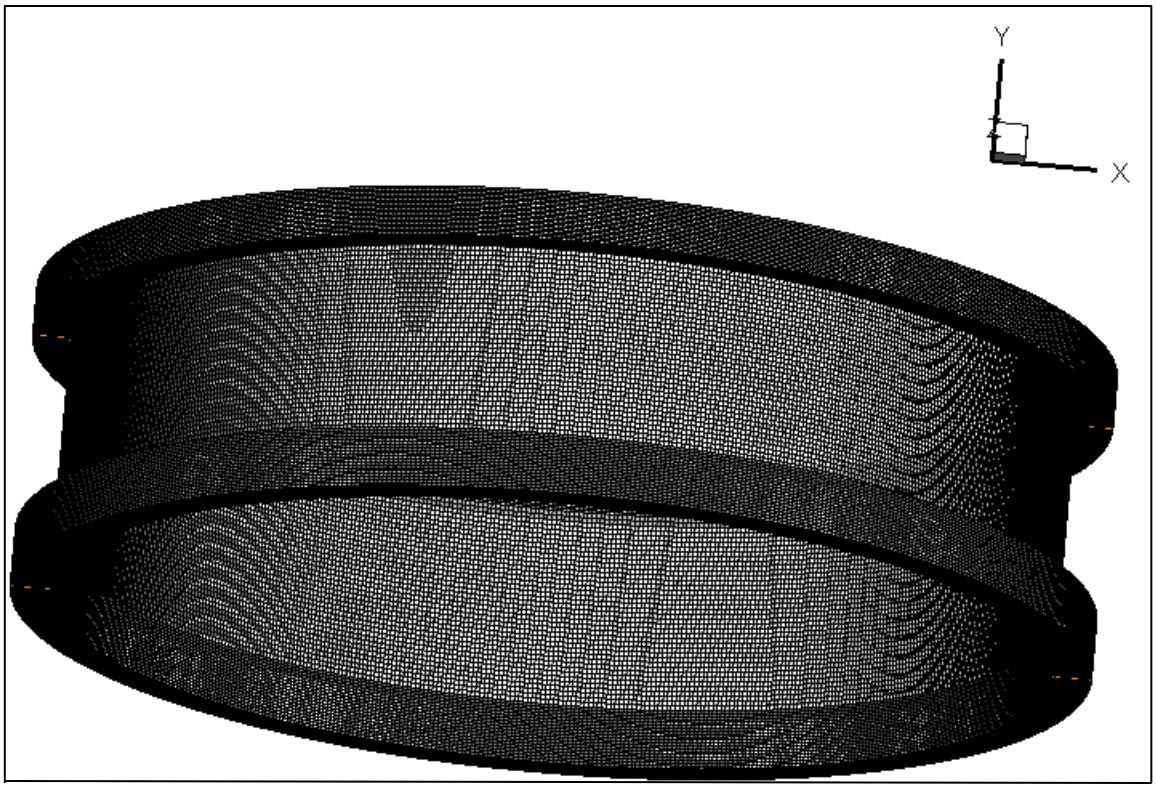

Figure 80. 3D Mesh, 25,92,000 Cells

Figure 80 shows the 3D grid. Due to numerical instabilities, the 3D simulation could not be run beyond 150 degree whirl angle. As per the Fluent User's Guide, for the cavitation model, large ratio of liquid to vapor density and near zero saturation pressures are unfavorable causes for convergence. The oil has a very low vapor pressure of 13.3 Pa. However, since it is known that the pressure field stabilizes and attains a quasi-steady state, it was examined if this condition was indeed attained before a whirl angle of 150 degree was reached. Due to numerical instabilities, the 3D simulation could not

be run beyond 150 degree whirl angle. The original mesh has elements with large aspect ratios to begin with since the flow domain has very large length to width ratio (R/c) and the total number of cells in the grid needs to be maintained at a reasonably small value to minimize computational resources required. Since the dynamic mesh is used the 3D mesh is stretched and compressed, resulting in elements with high aspect ratios and cell squish as the rotor whirls and the flow domain is deformed. Squish is a measure used to quantify the non-orthogonality of a cell with respect to its faces. The cell squish index of the original mesh before dynamic mesh deformation is 9.92299e-001. Although a warning about a cell squish index higher than 0.99 is displayed by the solver, the simulation can be run successfully even for such a mesh if further deterioration in mesh quality can be avoided. However, the cell squish further deteriorates to a maximum of 9.96288e-001, 9.96078e-001, 9.96274e-001, and 9.96111e-001 for the 1%, 3%, 5% and 7% dissolved gases cases respectively.

The pressure on the rotor, at the mid span of the SFD land was plotted for solutions obtained at 120 degree through 150 degree, in Figure 81.

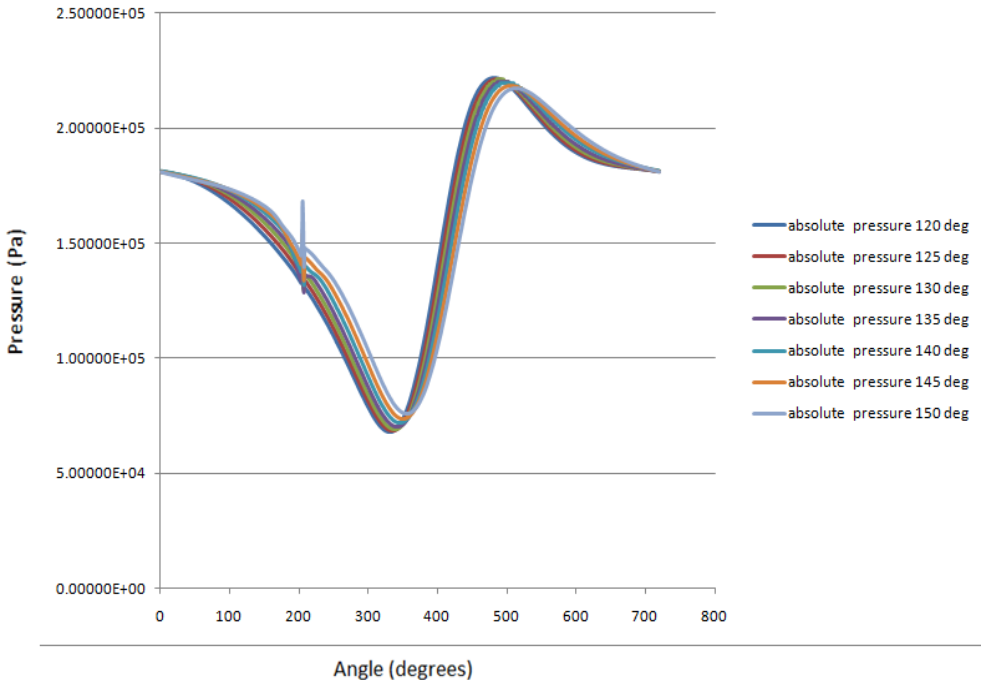

Figure 81. Convergence for 3D Case (0.127 mm Clearance, 25.4 mm SFD Land Length, 50 Hz Whirl Frequency, 0.074 mm or 60% Eccentricity, Supply Pressure 31 kPa, 1% Dissolved Air)

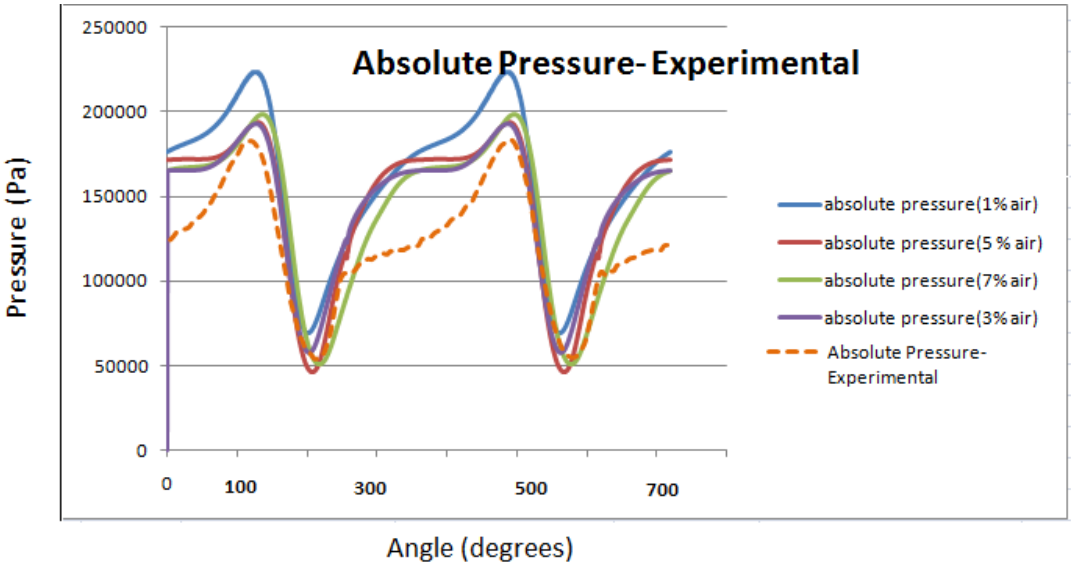

Figure 82. Pressure Distribution for Cases with Different Quantities of Dissolved Air

The pressure has been measured on the rotor wall at the mid span since the pressure probes also have been placed at the same location for the experimental measurements also by Delgado and San Andrés. Even a very small amount (e.g., 10 ppm) of non condensable gases can have significant effects on the cavitating flow field due to expansion at low pressures (following the ideal gas law). Since the exact quantity of pre dissolved non condensable gases is unknown, the quantity was varied from 1% to 7% by volume to evaluate which quantity best matches the experimental pressure profile.

The pressure prediction in the cavitation zone predicted from CFD exceeded the experimental pressure values (Figure 81 and Figure 82). This can be attributed to several facts. The ingestion of surrounding air into the SFD has not been simulated in the CFD study. Cavitation bubble formation on the surfaces is not taken into account by the CFD solver Fluent. The flat portion in the pressure plot has so far been attributed to air ingestion into the SFD. However this typical nature of the pressure plot has been obtained through CFD simulations as well despite air ingestion not being incorporated in the modeling. This provides evidence for the case that the flat portion of the pressure plot i.e slow increase in pressure, might be partly due to the gaseous cavitation phenomenon as well.

Thus it is observed that both P_{max} and P_{min} have been predicted well by the CFD flow. The pressure profile is predicted well, in general, except in the cavitation portion of the profile. The details of flow predicted by CFD calculations will now be examined.

Contour plots of the Pressure distribution at various axial locations of the SFD are investigated to evaluate the change in pressure field in the axial direction. The inlet pressure is 31 kPa (gauge). The cross-sections are evenly spaced in the SFD land. The rotor has undergone a whirl of 110 degree from the positiveve X axis. The direction of whirl is anti-clockwise. The first cross-section is taken at the opening of the narrow section, 6.35 mm from the top surface as shown in SECTION A-A of Figure 89. This is the location where the radial clearance reduces to 0.0560 mm from 4.8762 mm. Sections 2, 3,4 and 5 are taken at even intervals of 6.35 mm in the axial direction from Section 1. Section 6 is the outlet or the lower surface in SECTION A-A. The area of interest i.e. the radial clearance is exaggerated in size using a coordinate transformation. Similarly, pressure distributions across radial cross-sections are also studied. The radial cross-sections 1 through 4 are taken at 0, 45, 90 and 135 degree locations. Following are the Pressure Contours at axial Sections 1 through 6 (Figure 83 through Figure 88).

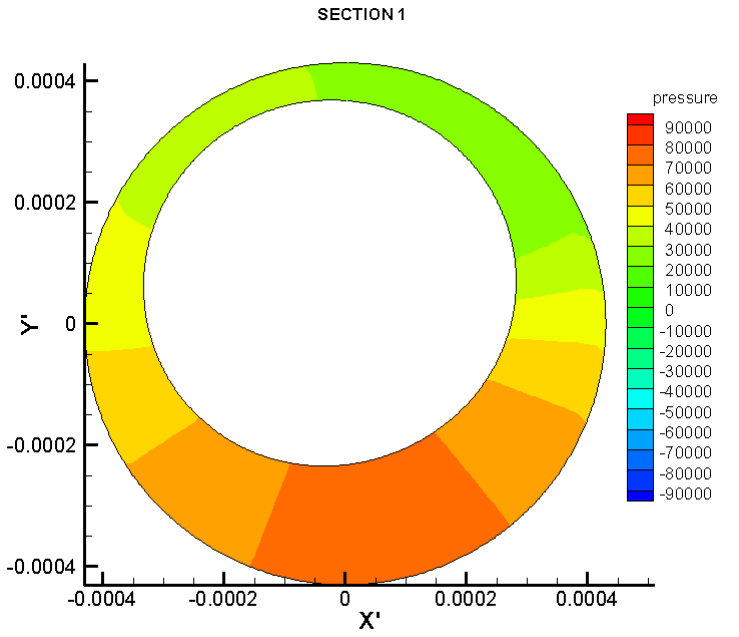

Figure 83. Contours of Pressure at Section 1

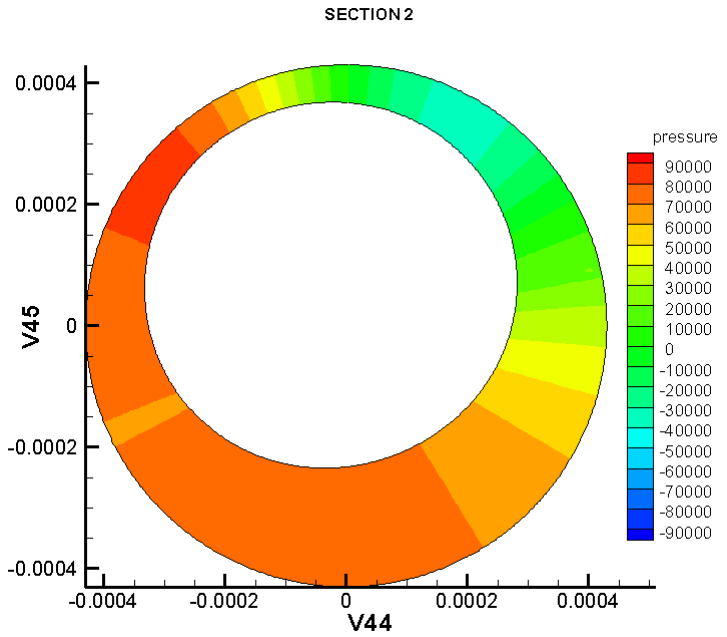

Figure 84. Contours of Pressure at Section 2

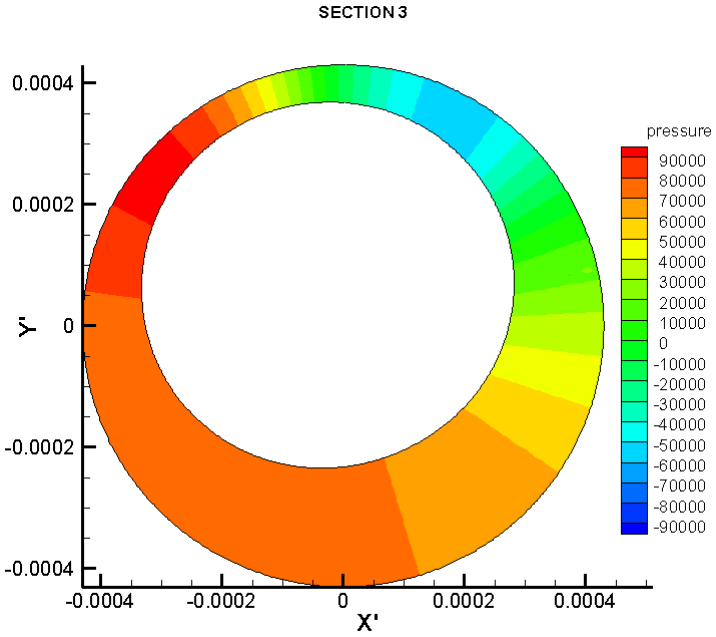

Figure 85. Contours of Pressure at Section 3

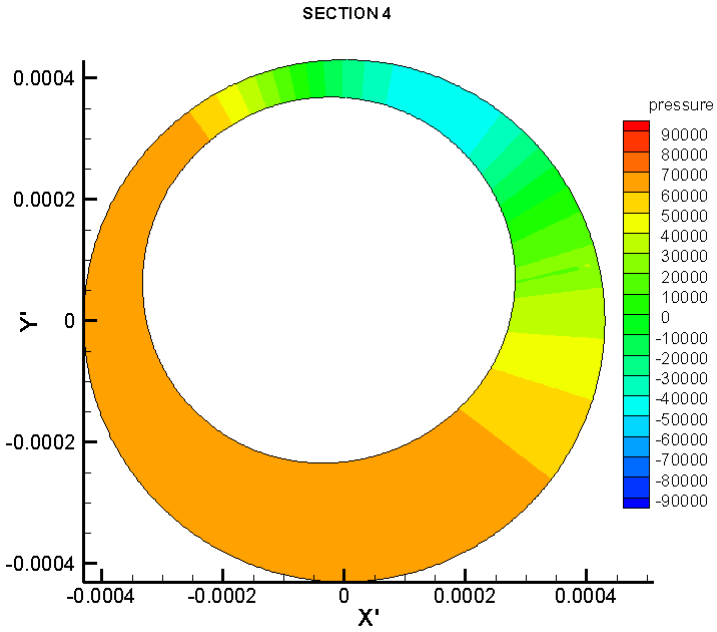

Figure 86. Contours of Pressure at Section 4

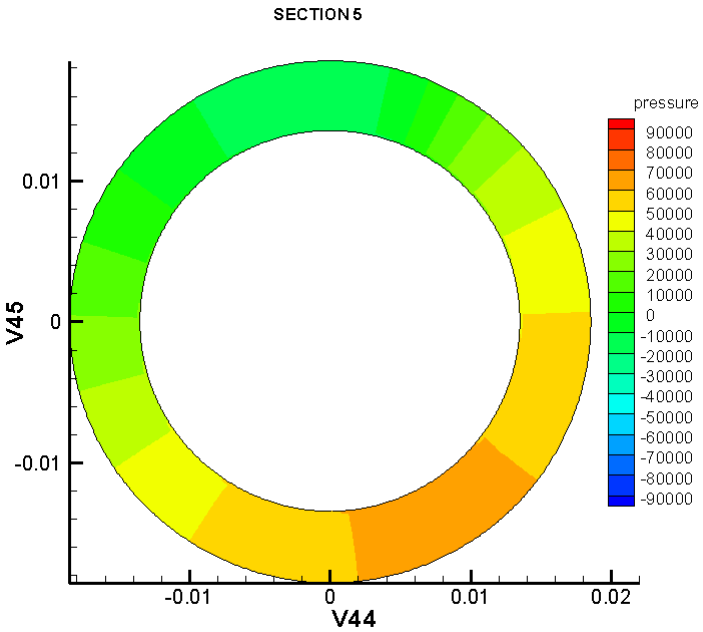

Figure 87. Contours of Pressure at Section 5

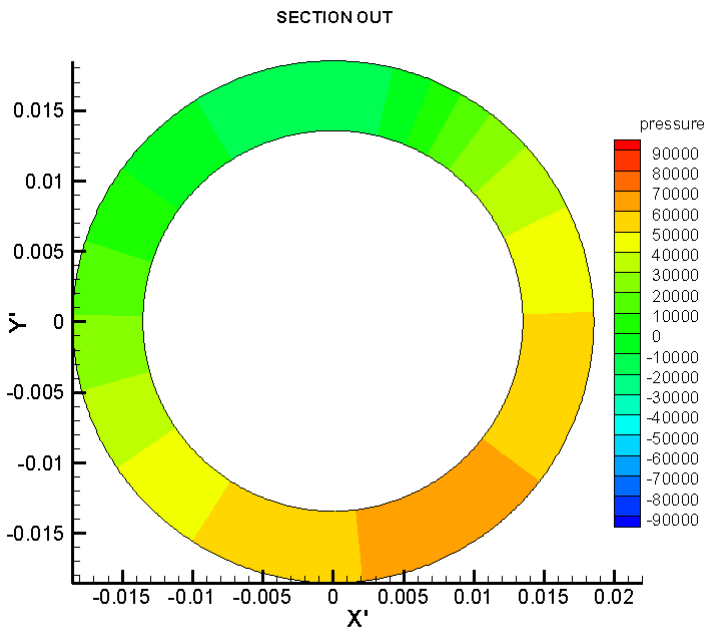

Figure 88. Contours of Pressure at Section 6

Section 1, as it can be seen from Figure 79, is at the end of the feed plenum or the entrance of the SFD land. The top most surface i.e. the entrance of the feed plenum has a uniform supply pressure of 31 kPa. It can be seen from the above plots that the high pressure zone shifts from the maximum clearance region at the entrance of the SFD land to the minimum clearance region at the mid span of the SFD land. It shifts towards the maximum clearance region again as we move downwards to the end of the SFD land. The minimum pressure zone however stays almost unchanged in position with respect to the minimum clearance. The magnitude of P_{max} increases from the top to the mid span of the SFD land and reduces again as we move down towards the exit. The pressure distribution stays the same throughout the recirculation annulus as it can be seen from the contour plots at Section 5 (end of SFD land or entrance of the recirculation annulus) and Section 6 (sealed exit of the SFD).

We can see that the pressure distribution in the clearance of the SFD land is not symmetric about the mid section i.e. the pressure distributions at Sections 2 and 4 for example, are not similar although they are equidistant on either side of the mid-section. This is due to the fact that the opening of the SFD is maintained at constant supply pressure of 31 kPa while the exit is sealed. In future studies, it would be interesting to study the effect of degree of sealing at the exit, on the pressure distribution along the axial direction. Next, the pressure distributions at different angular locations were studied. Following are pressure contours (Figure 89 through Figure 96) at radial Sections 1 through 4 (Angles measure in anti-clockwise sense from positive X axis).

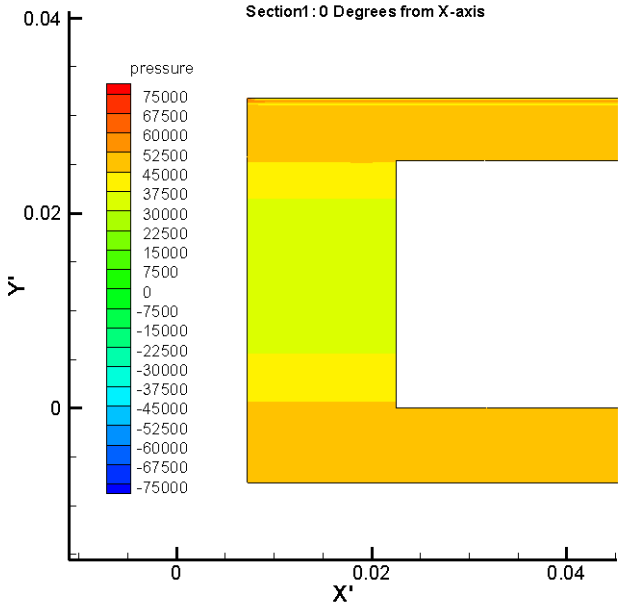

Figure 89. Axial Pressure Distribution at 0 Degree from +ve X Axis

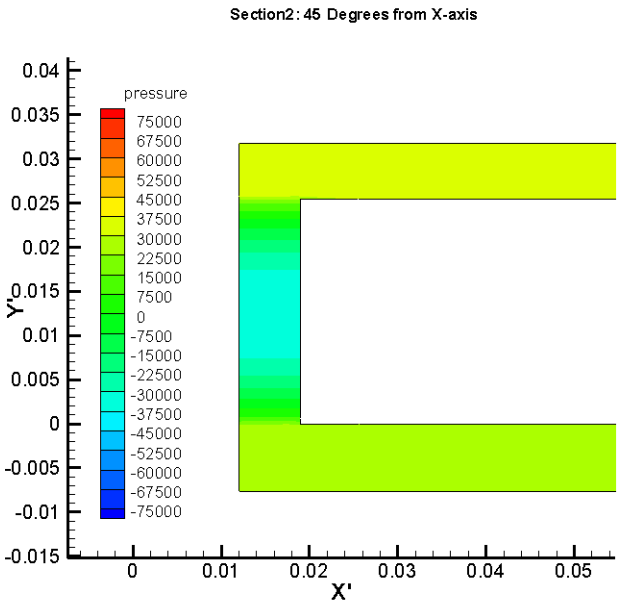

Figure 90. Axial Pressure Distribution at 45 degree from +ve X Axis

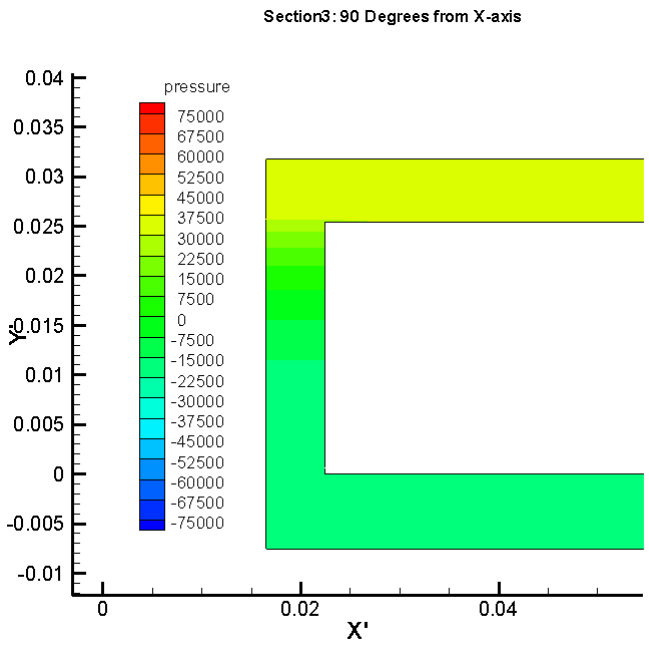

Figure 91. Axial Pressure Distribution at 90 Degree from +ve X Axis

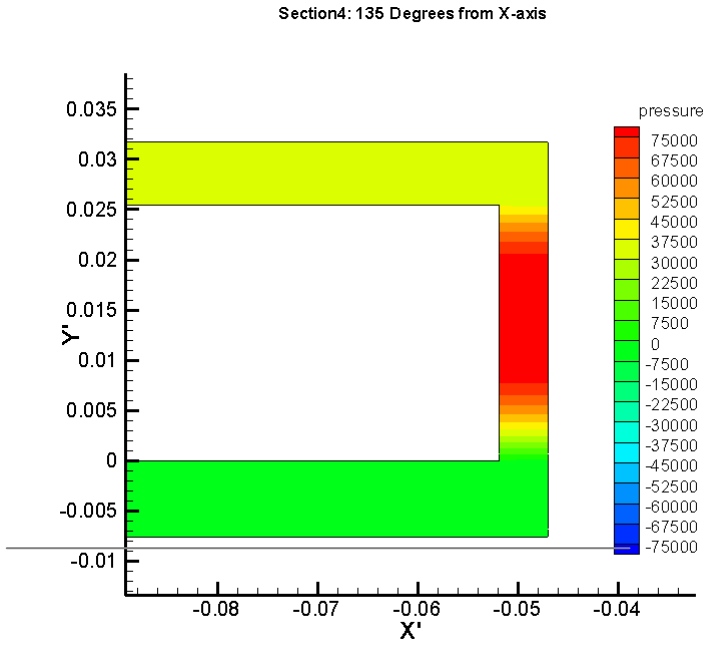

Figure 92. Axial Pressure Distribution at 135 Degree from +ve X Axis

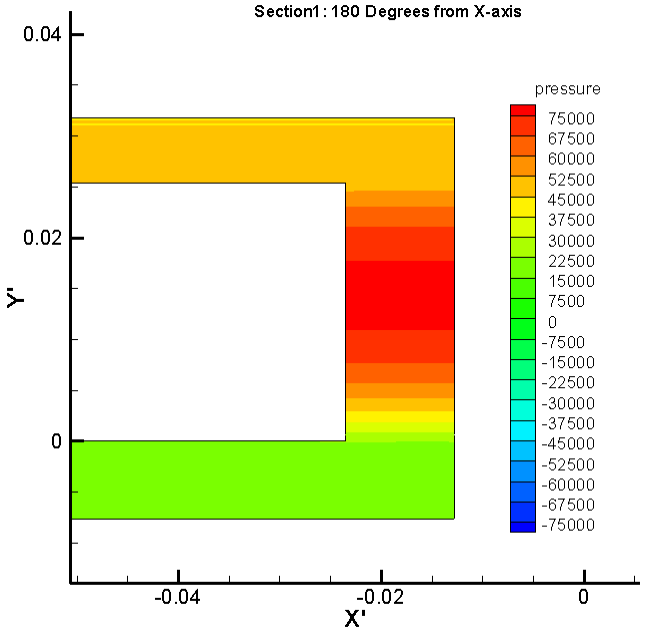

Figure 93. Axial Pressure Distribution at 180 Degree from +ve X Axis

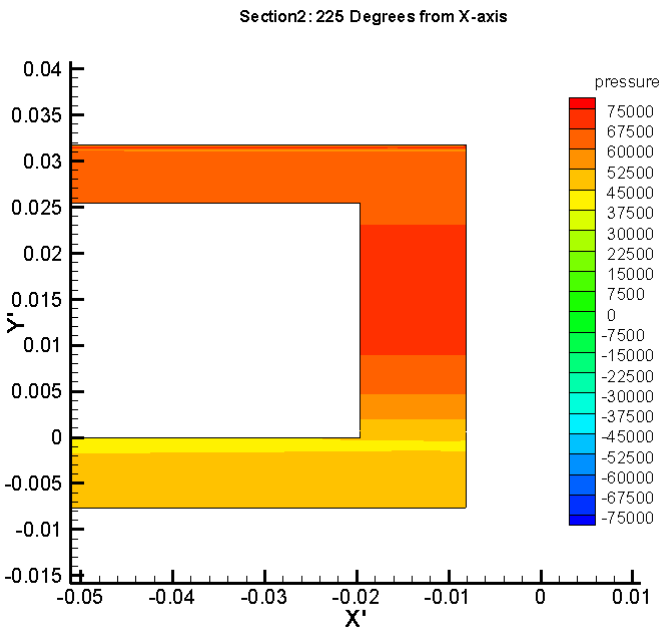

Figure 94. Axial Pressure Distribution at 225 Degree from +ve X Axis

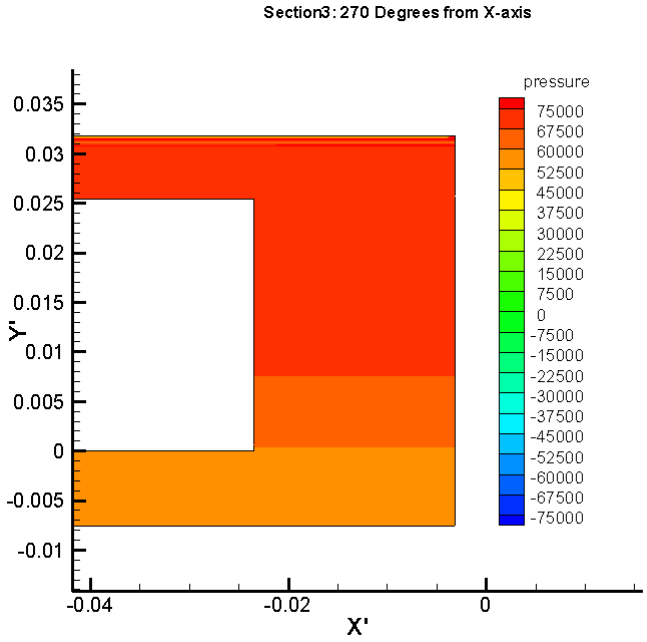

Figure 95. Axial Pressure Distribution at 270 Degree from +ve X Axis

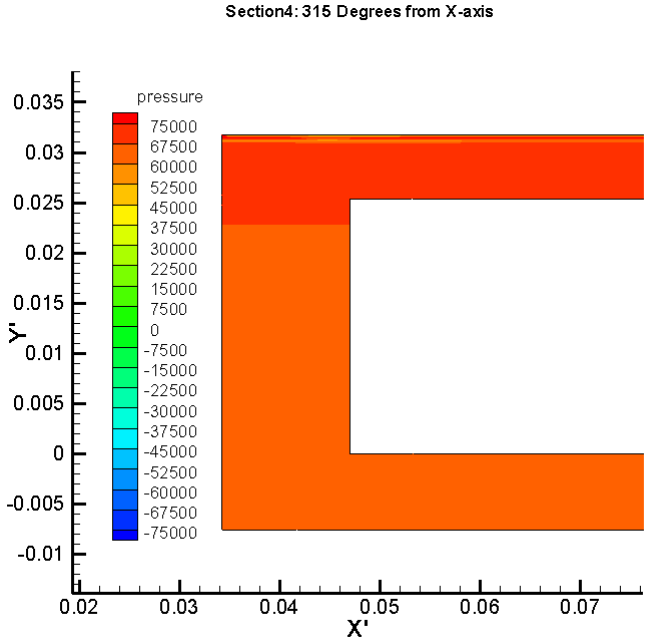

Figure 96. Axial Pressure Distribution at 315 Degree from +ve X Axis

The rotor whirls in an anticlockwise direction and the minimum clearance is located 110 degree from the positive X axis. The clearance decreases from a maximum at 110 degree to a minimum at 290 degree. It is noticed that at all angular positions the pressure is always higher in the feed plenum than the recirculation annulus. Also, at 0 degree and 45 degree positions, as we approach the minimum clearance region, pressure is lower at the mid span of the SFD land compared to the feed plenum and the recirculation annulus. As we approach 110 degree, the high pressure zone appears at the mid span of the land. A high pressure zone (compared to the feed plenum and recirculation annulus) is maintained at the center of the SFD land up to 225 degree beyond which it shifts towards the feed plenum. A close look at the vectors of axial velocity at various angular locations and vectors of radial velocity at the 6 axial sections are presented (Figure 97 through Figure 110). The minimum clearance region is located at 110 degree. Close to his region, the fluid is squeezed outwards from the mid span of the SFD land towards the top and bottom, as the clearance increases from a minimum at 110 degree, (sections 4 and 5 at 135 degree and 180 degree respectively) as it can be seen from the axial velocity vectors. On the other hand, the fluid appears to be moving towards the mid section of the SFD land close to the maximum clearance region located at 290 degree (section 4 and section 1 at 315 and 0 degree respectively), as the clearance decreases. The magnitude of axial velocity is very small in the feed plenum and the recirculation annulus compared to the SFD land.

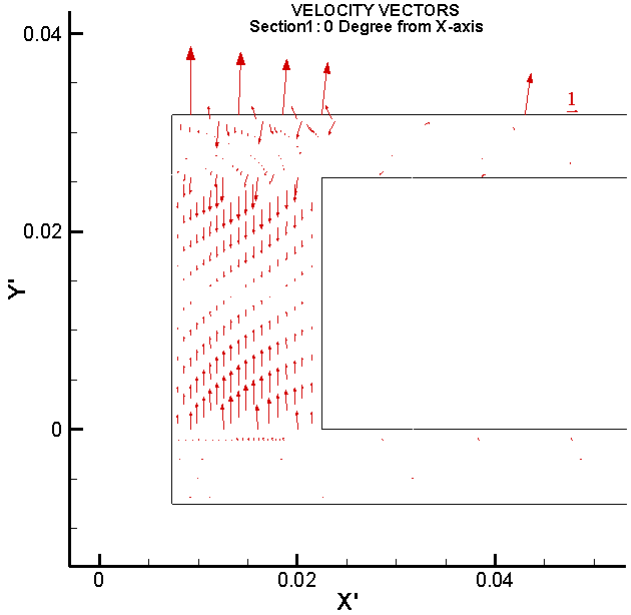

Figure 97. Vectors of Axial Velocity at 0 Degree

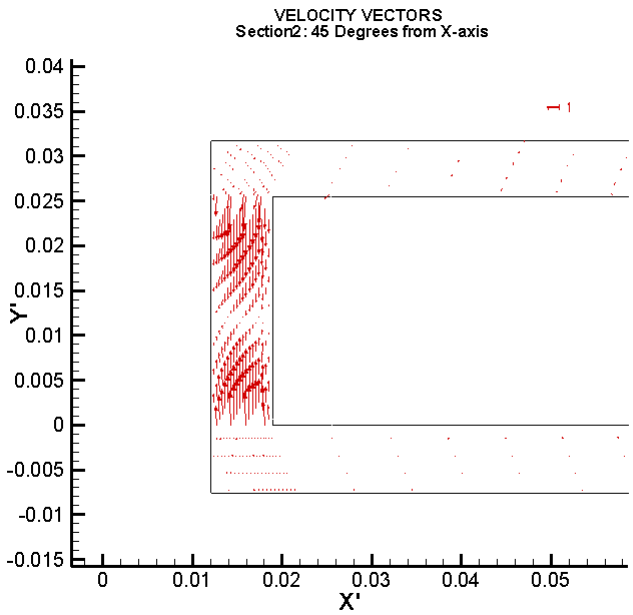

Figure 98. Vectors of Axial Velocity at 45 Degree

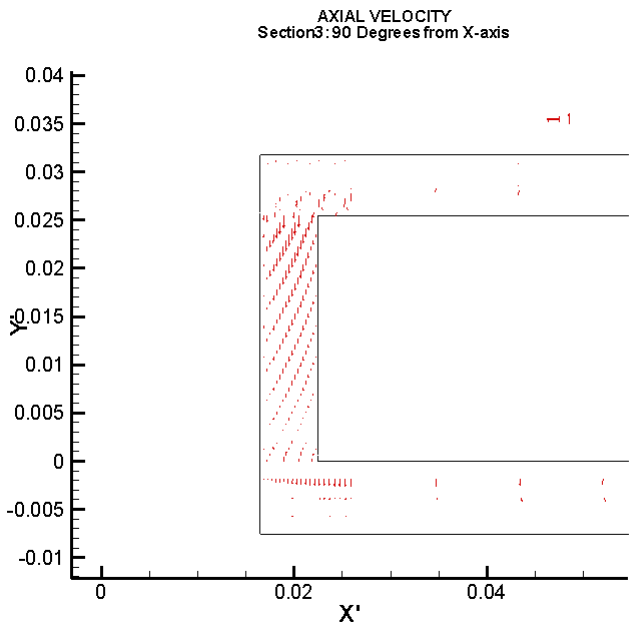

Figure 99. Vectors of Axial Velocity at 90 Degree

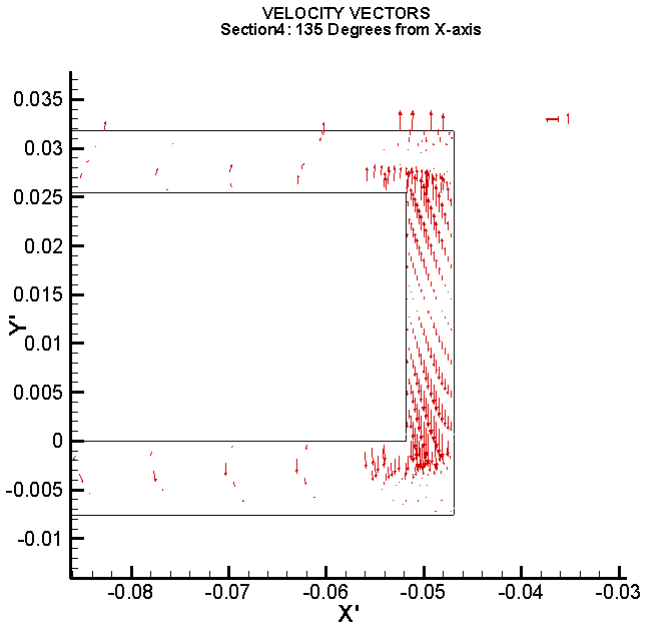

Figure 100. Vectors of Axial Velocity at 135 Degree

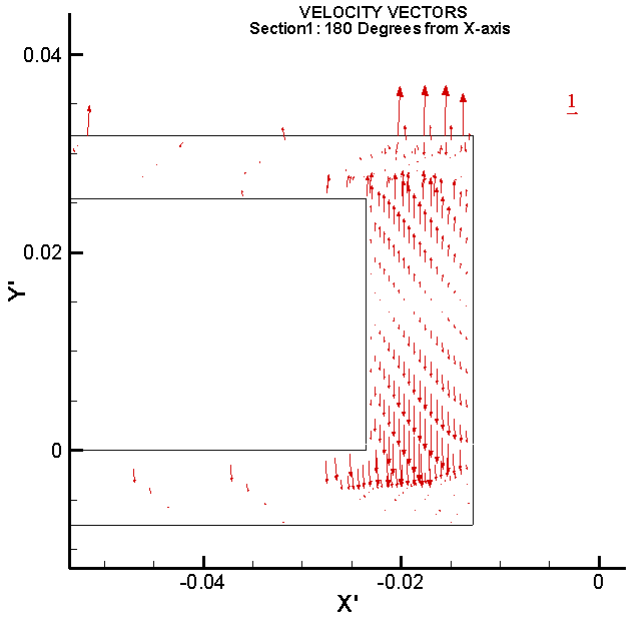

Figure 101. Vectors of Axial Velocity at 180 Degree

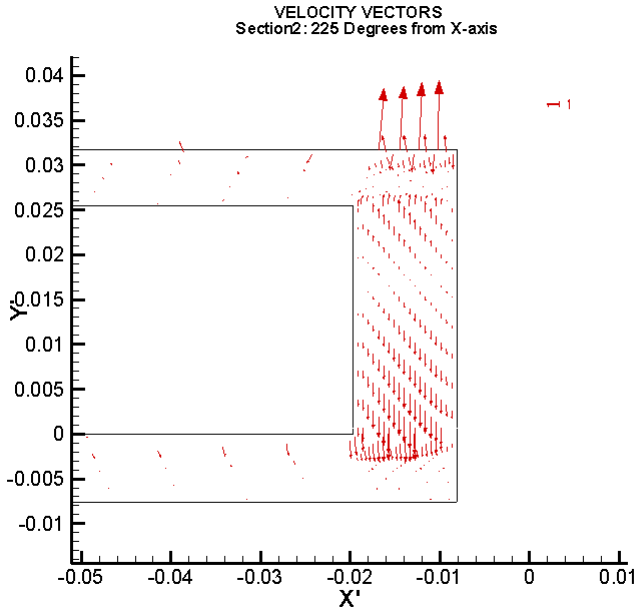

Figure 102. Vectors of Axial Velocity at 225 Degree

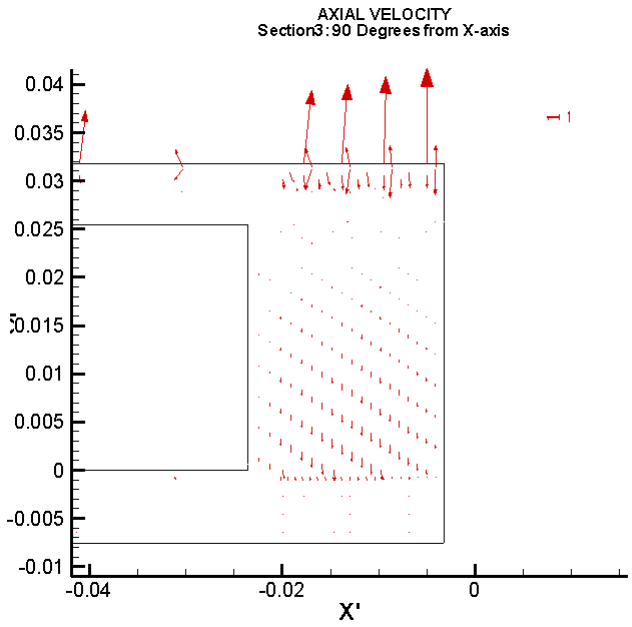

Figure 103. Vectors of Axial Velocity at 270 Degree

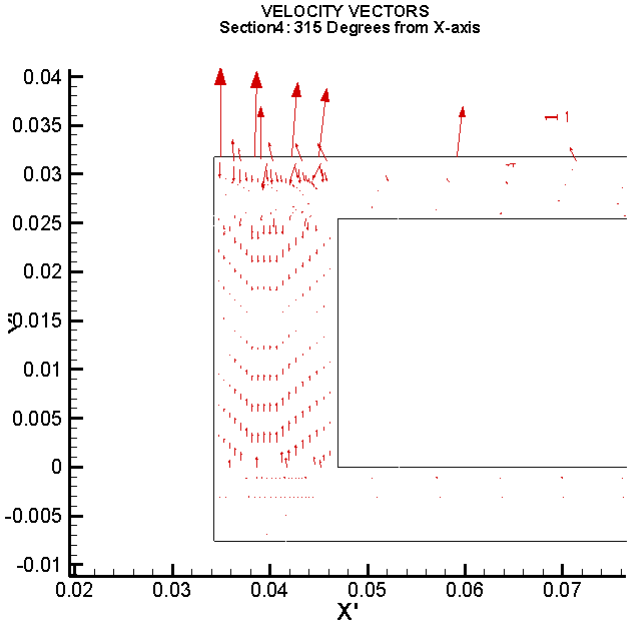

Figure 104. Vectors of Axial Velocity at 315 Degree

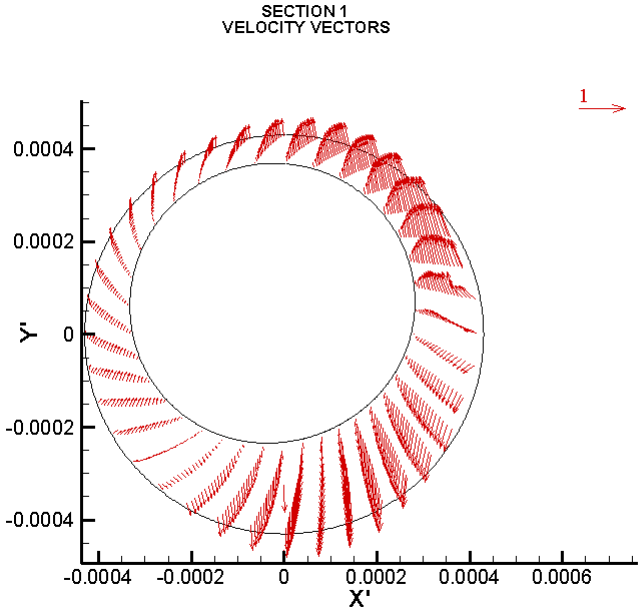

Figure 105. Vectors of Tangential Velocity at Section 1

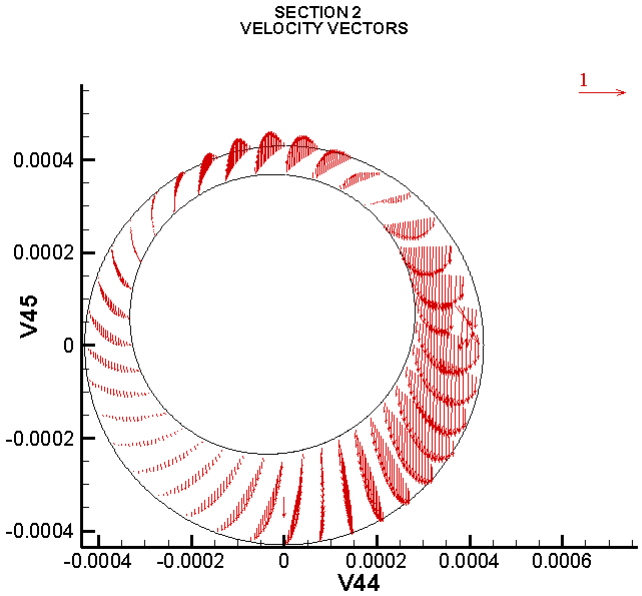

Figure 106. Vectors of Tangential Velocity at Section 2

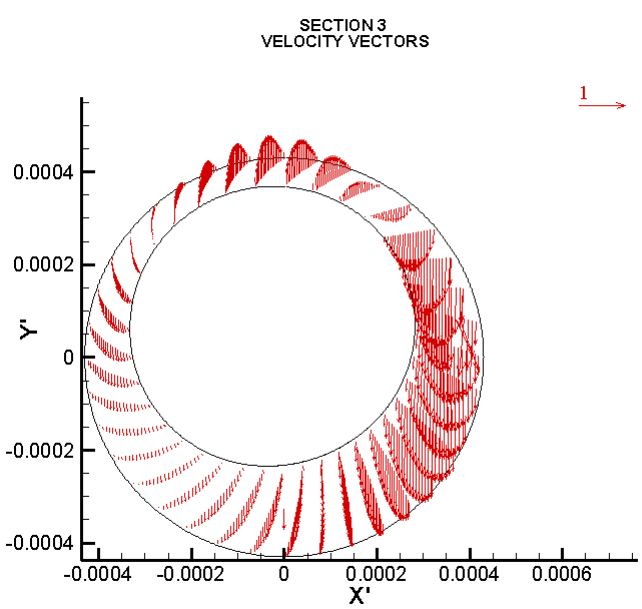

Figure 107. Vectors of Tangential Velocity at Section 3

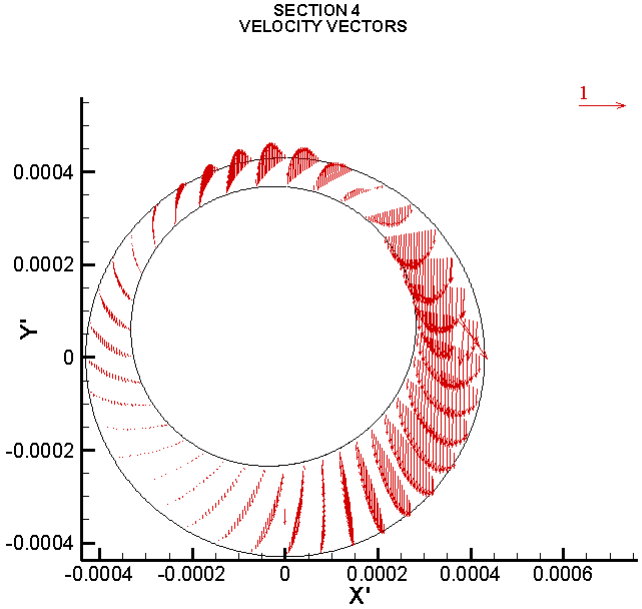

Figure 108. Vectors of Tangential Velocity at Section 4

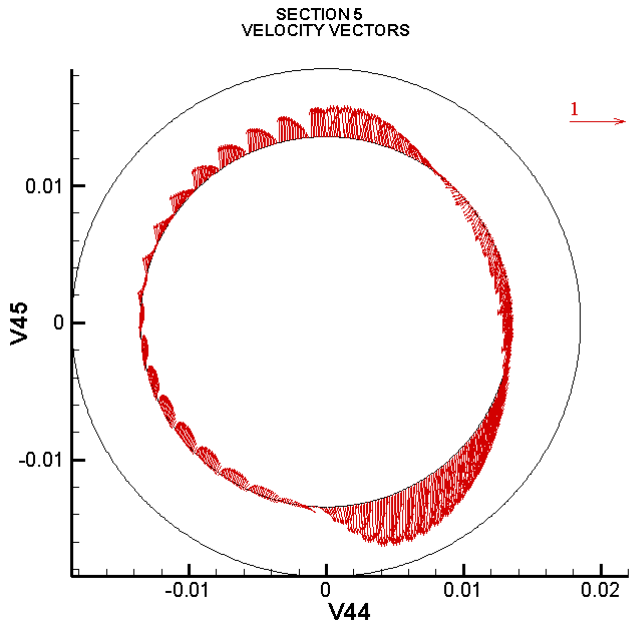

Figure 109. Vectors of Tangential Velocity at Section 5

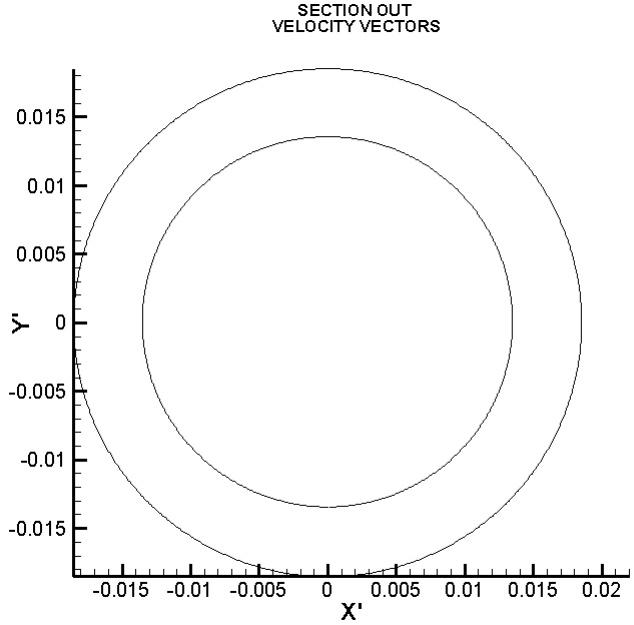

Figure 110. Vectors of Tangential Velocity at Section 'out'

Since the exit of the SFD is sealed, the axial and tangential velocities are zero as expected. As mentioned earlier, the minimum clearance is at 110 degree from positive X axis and the Rotor is whirling in the anticlockwise direction. At section 1 (located at the opening of the SFD land or at the end of the feed plenum), the fluid flows in the direction of the rotor into the minimum clearance, in the opening clearance region (the region of increasing clearance). Fluid also flows opposite to the rotor's direction of whirl in the other quarter of the opening clearance. The magnitude of the tangential velocity in the closing clearance region is much smaller in comparison to the opening clearance region and it moves in the same direction as the rotor. As we move down the SFD land through sections 2 through 5, the same nature of fluid flow is observed. The magnitude of tangential velocity of the fluid in the opening clearance which flows opposite to the rotor whirl direction however increases.

Next, the force acting on the Rotor and the line of action of force with respect to minimum clearance were studied. Since the simulations were terminated at 110 degree, it needs to be investigated if the force has stabilized and the quasi-steady state reached.

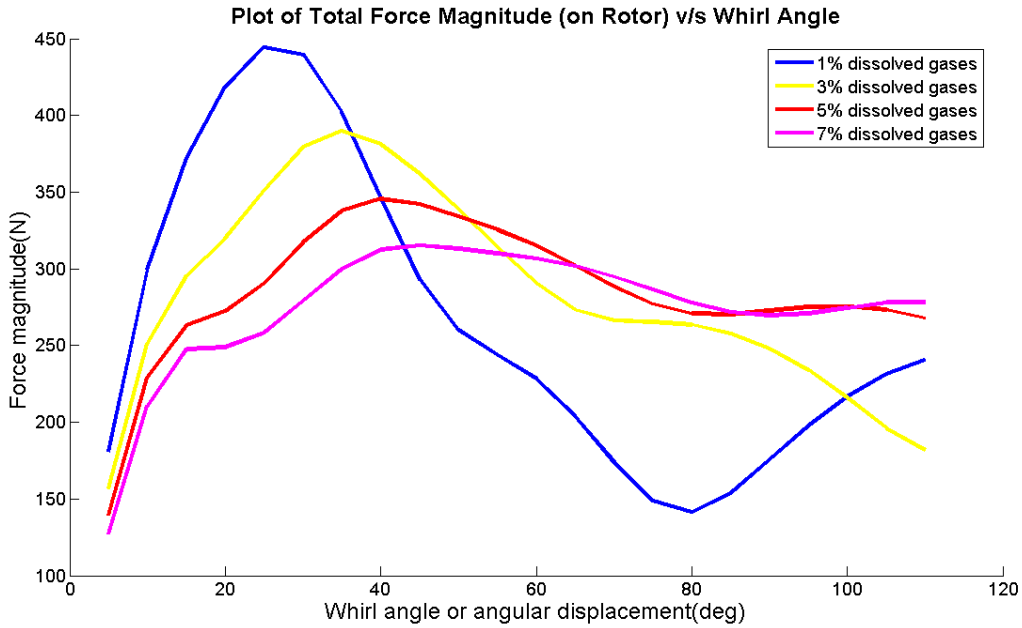

Figure 111. Magnitude of Force on Rotor v/s Whirl Angle (0.127 mm Clearance, 25.4 mm SFD Land Length, 50 Hz Whirl Frequency, 0.074 mm or 60% Eccentricity, Supply Pressure 31 kPa, 1, 3, 5 & 7% by Vol. Non-condensable Dissolved Gases)

As the amount of dissolved gases is increased, the maximum pressure and total force on rotor tends to decrease (Figure 111). The force magnitude appears to be approaching a steady value. The slope of the 5% dissolved gases and 7% dissolved gases curves in particular reach a near zero value. For low quantities of dissolved air, the rotor is under damped and the force magnitude oscillates. As the quantity of dissolved air is increased, damping increases and there is very little over & undershoot. The rate of increase of force on rotor from the static condition or the slope of the curve too, decreases with increase in quantity of dissolved gases. For the 2 dimensional cases a

steady value is attained at about 400 degree. However a steady value appears to have been reached fairly quickly for the 3 dimensional cases.

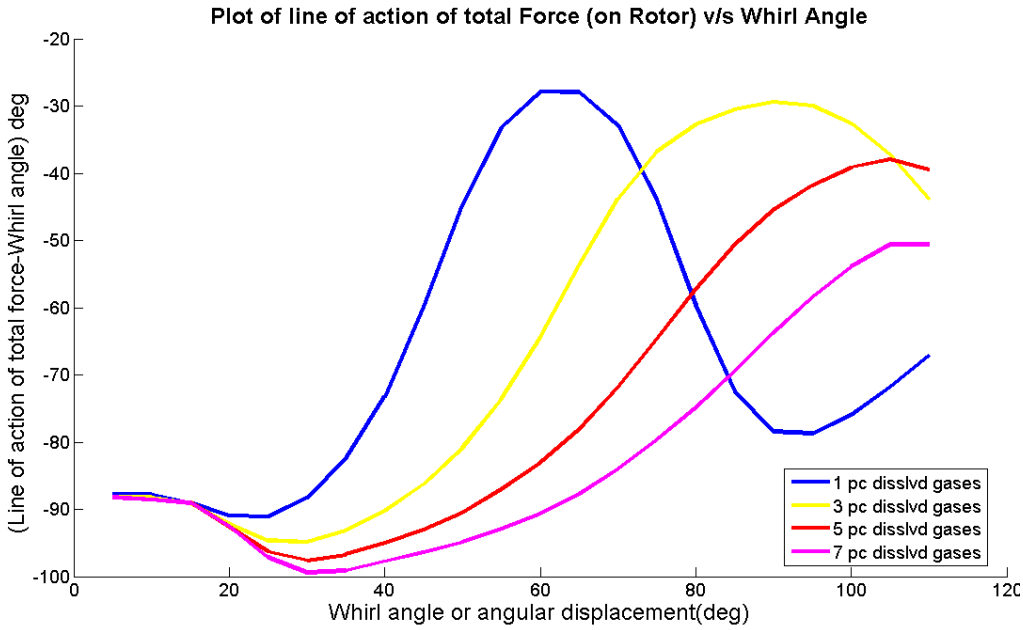

Figure 112. Line of Action of Total Force on Rotor with Respect to Min. Clearance v/s Whirl Angle (0.127 mm Clearance, 25.4 mm SFD Land Length, 50 Hz Whirl Frequency, 0.074 mm or 60% Eccentricity, Supply Pressure 31 kPa, 3% Dissolved Air)

The line of action of force with respect to the minimum clearance also appears to be approaching a steady value (Figure 112). For the two dimensional cases it attains a steady value at about 400 degree. However, the nature of the curve is very different from the two dimensional case. For the two dimensional case, the angle of line of action of Force with respect to the minimum clearance decreases sharply initially, then increases and settles to a steady value. In the three dimensional case on the other hand, this angle slightly decreases initially, then sharply increases. The curve representing 1% dissolved

gases oscillates and the variations appear to become smaller with time. The variation in the angle is between a 90 degree range.

The force acting on the rotor in the axial direction is almost negligible. This is verified from the plot of magnitude of axial force on the rotor v/s whirl angle (Figure 113). This force too appears to have reached a steady value.

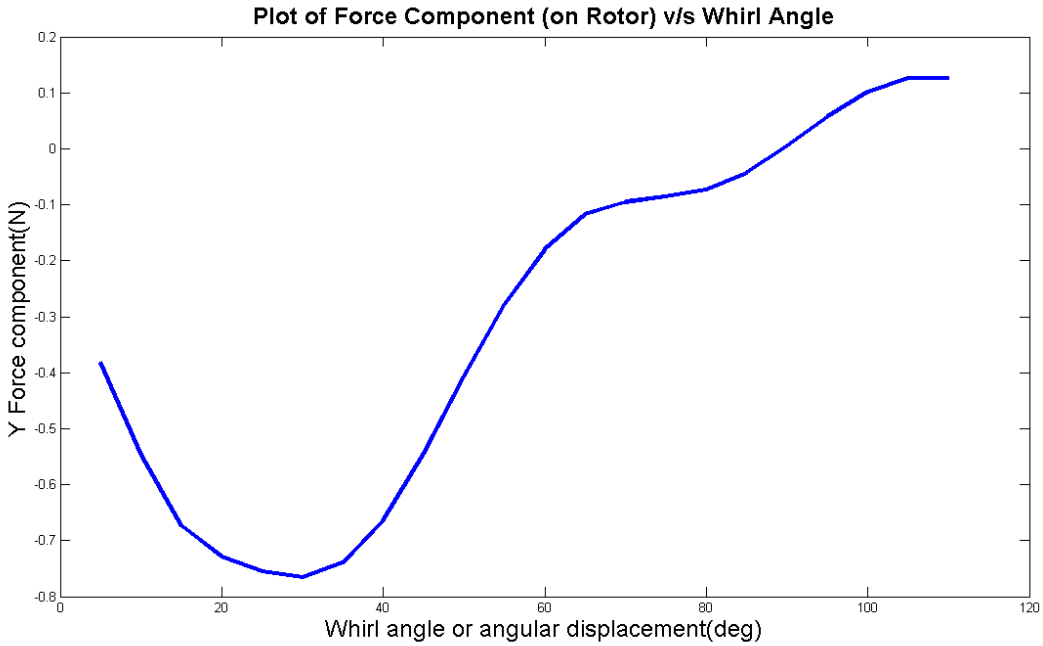

Figure 113. Magnitude of Axial Force v/s Whirl Angle

7. CONCLUSION

The feasibility of applying CFD to the study of flow field in a Squeeze Film Damper (SFD) was examined. Initially, 2D cases were studied. Dynamic deforming mesh capability of Fluent® was used to simulate the whirling motion of the rotor in a SFD. An unsteady solver with the mixture model was used to include the effect of cavitation. The CFD results (pressure distributions in the squeeze film) were compared to experimental data for a 5 mil clearance, 50 Hz rotating frequency case. The quantity of dissolved air in the working fluid was varied. The CFD results showed good agreement with the experimental results. However, the pressure prediction in the cavitation zone predicted from CFD exceeded the experimental pressure values. This could be attributed to several facts. The ingestion of surrounding air into the SFD has not been simulated in the CFD study. Cavitation bubble formation on the surfaces is not taken into account by CFD solver Fluent. The flat portion in the pressure plot has so far been attributed to air ingestion into the SFD. However this typical nature of the pressure plot has been obtained through CFD simulations as well despite air ingestion not being incorporated in the modeling. This provides evidence for the case that the flat portion of the pressure plot i.e. slow increase in pressure, might be partially due to the gaseous cavitation phenomenon as well.

It was found that a 3D geometry requires a significant number of cells in the grid and this dense grid combined with the dynamic mesh model in Fluent considerably increases the simulation time. The availability of faster computers in the near future,

improvements in the methodology and alleviating problems of numerical instability would make the use of CFD an attractive option for analyzing Squeeze Film Dampers.

8. FUTURE SCOPE

1. Address the numerical instabilities so as to run the simulation for more time-steps and higher rotor speeds.
2. Change the cavitation models used to achieve better prediction of pressure distribution in the cavitating region (plateau region of the pressure plot). Currently, the CFD predictions exceed the experimental values in this region.
3. The accuracy of prediction could be further improved by incorporating the complex effects of air-ingestion in the model. In the present work, only the effects of gaseous and vapor cavitation have been included.
4. The type of sealing present also affects the degree of air-ingestion and cavitation. The effect of type and degree of sealing could be included in future studies.
5. The present study includes only circular whirl orbits. Non-circular orbits could be studied too, for future work, by merely modifying the User Defined Function.
6. It would if interest to study the behavior of lubricants other than Mobil Velocite 3 in future simulations.
7. Most practical SFDs have feed grooves or end grooves present. For future work, a groove could be introduced in the SFD land and its effect on the pressure distribution could be studied. Subsequently, the number of grooves could be increased.

REFERENCES

[1] San Andrés, L., 2008, "MEEN 626 Course Notes," Mech. Eng. Dept., Texas A&M University, College Station, http://rotorlab.tamu.edu/me626/.

[2] Zeidan, F., 1989, "Cavitation Effects on the Performance of Squeeze Film Damper Bearings," PhD Dissertation, Texas A&M University, College Station.

[3] Zeidan, F., and Vance, J., 1990, "Cavitation Regimes in Squeeze Film Dampers and Their Effect on the Pressure Distribution," *STLE Tribology Transactions*, Vol. 33, 447-453.

[4] Zeidan, F., and Vance, J., 1990, "Cavitation and Air Entrainment Effects on the Response of Squeeze Film Supported Rotors," *ASME J. Tribology*, Vol. 112, 347-353.

[5] Delgado, A., 2008, "A Linear Fluid Inertia Model for Improved Prediction of Force Coefficients in Grooved Squeeze Film Dampers and Grooved Oil Seal Rings," PhD Dissertation, Texas A&M University, College Station.

[6] Chen, P., and Hahn, E., 1998, "Use of Computational Fluid Dynamics in Hydrodynamic Lubrication," *Proceedings of the Institute of Mechanical Engineers*, Vol. 212, part J.

[7] Guo, Z., Hirano, P., and Gordon Kirk, R., 2005, "Application of CFD Analysis for Rotating Machinery- Part I: Hydrodynamics, Hydrostatic Bearings and Squeeze Film Damper," *ASME J. Engr. for Gas Turbine and Power, Proceedings of the Institute of Mechanical Engineers*, Vol. 127, 445-451.

[8] Xing, C., 2009, "Analysis of the Characteristics of a Squeeze Film Damper by Three-Dimensional Navier-Stokes Equations: A Numerical Approach and Experimental Validation," PhD Dissertation, University of Akron, Ohio.

[9] Della Pietra, L., and Adiletta, G., 2002, "The Squeeze Film Damper over Four Decades of Investigations. Part I: Characteristics and Operating Features," *The Shock and Vibration Digest*, Vol. 34, 3-26.

[10] Della Pietra, L., and Adiletta, G., 2002, "The Squeeze Film Damper over Four Decades of Investigations. Part II: Rotordynamic Analyses with Rigid and Flexible Rotors," *The Shock and Vibration Digest*, Vol. 34, 97-126.

[11] Thomsen, K., and Andersen, H., 1974, "Experimental Investigation of a Simple Squeeze Film Damper," *Trans ASME J. of Engineering for Industry*, Vol. 96, 427-430.

[12] Vance, J., Kirton, A., 1975, "Experimental Measurement of the Dynamic Force Response of a Squeeze Film Bearing Damper," *Trans ASME J. of Engineering for Industry*, Vol. 97, 1282-1290.

[13] Feder E., Bansal, P.N., Blanco, A., 1978, "Investigation of Squeeze Film Damper Forces Produced By Circular Centered Orbits," *Trans ASME J. of Engineering Power*, Vol. 100, n 1, 15-21.

[14] Bansal, P.N., Hibner, D.H., 1978, "Experimental and Analytical Investigation of Squeeze Film Bearing Damper Forces Inducted by Offset Circular Whirl Orbits," *Trans ASME J. Mech Des*, Vol. 100, n 3, 549-57.

[15] San Andres, L., Vance, J., 1987, "Effect of Fluid Inertia on Squeeze-Film Damper Forces for Small-Amplitude Circular-Centered Motions," *Trans ASLE*, Vol. 30, 63-68.

[16] Jung, S.Y., San Andres, L., Vance, J., 1991, "Measurements of Pressure Distributions and Force Coefficients in a Squeeze Film Damper Part I. Fully Open Ended Configurartion," *Tribology Trans*, Vol. 34, 375-382.

[17] Jung, S.Y., San Andres, L., Vance, J., 1991, "Measurements of Pressure Distributions and Force Coefficients in a Squeeze Film Damper Part II. Fully Open Ended Configurartion," *Tribology Trans*, Vol. 34, 383-388.

[18] Della Pietra, L., 2000, “Analytical and Experimental Investigation of Squeeze-Film Dampers Executing Circular Orbits,” *Meccanica*, Vol. 35, 133–157.

[19] Arauz, G.L., San Andres, L., 1993 , “Experimental Pressures and Film Forces in a Squeeze Film Damper Part,” *J. Tribology*, Vol. 115, 134-140.

[20] Feng, N.S., Hahn, E.J., 1986, “Density and Viscosity Models for Two-Phase Homogenous Hydrodynamic Damper Fluids,” *Trans ASLE*, Vol. 29, 361-69.

[21] Feng, N.S., Hahn, E.J., 1986, “Cavitation Effects on Squeeze Film Damper Performance,” *Trans ASLE*, Vol. 29, 353-60.

APPENDIX A

MIXTURE MODEL USED IN FLUENT®

The mixture model in Fluent® can be used to model multiphase flows for both cases viz. phases moving at different velocities but possessing local equilibrium over short length scales and for phases moving at same velocities i.e. homogenous multiphase flows. For this study, a homogenous mixture assumption was made. The continuity, momentum and energy equations are solved for the mixture and the volume fraction equations are solved for the secondary phases. Algebraic relations are solved for relative velocities (slip velocities) in case of phases moving with different velocities.

The following are the governing equations solved by the mixture model. A suffix 'm' is used for the governing equations of the mixture and a suffix 'p' is used for those of the secondary phase.

Continuity equation for the mixture

$$\frac{\partial}{\partial t}(\rho_m) + \nabla \cdot (\rho_m \vec{v}_m) = 0 \tag{A.1}$$

where,

$\vec{v}_m$ is the mass-averaged velocity given by

$$\vec{v}_m = \frac{\sum_{k=1}^{n} \alpha_k \rho_k \vec{v}_k}{\rho_m} \tag{A.2}$$

ρ_m is the mixture density given by $\rho_m = \sum_{k=1}^{n} \alpha_k \rho_k$

and α_k is the volume fraction of the phase k.

Momentum equation for the mixture

The momentum equation for the mixture is obtained by simply summing the individual momentum equations for the individual phases. It is given by

$$\frac{\partial(\rho_m \vec{v}_m)}{\partial t} + \nabla \cdot (\rho_m \vec{v}_m \vec{v}_m) = -\nabla p + \nabla \cdot [\mu_m (\nabla \vec{v}_m + \vec{v}_m^T)] + \rho_m \vec{g} + \vec{F} + \nabla \cdot (\sum_{k=1}^{n} \alpha_k \rho_k \vec{v}_{dr,k} \vec{v}_{dr,k}) \quad \text{(A.3)}$$

With n being the number of phases, $\vec{F}$ being the body force, μ_m being the viscosity of the mixture given by

$$\mu_m = \sum_{k=1}^{n} \alpha_k \mu_k \quad \text{(A.4)}$$

and $\vec{v}_{dr,k}$ is the drift velocity for the phase k given by

$$\vec{v}_{dr,k} = \vec{v}_k - \vec{v}_m \quad \text{(A.5)}$$

Energy Equation for the mixture

$$\frac{\partial}{\partial t} \sum_{k=1}^{n} (\alpha_k \rho_k E_k) + \nabla \cdot \sum_{k=1}^{n} (\alpha_k \vec{v}_k (\rho_k E_k + p)) = \nabla \cdot (k_{eff} \nabla T) + S_E \quad \text{(A.6)}$$

k_{eff} is the effective conductivity given by

$$k_{eff} = \sum \alpha_k (k_k + k_t) \quad \text{(A.7)}$$

where k_t is the turbulent conductivity which depends on the turbulence model being used. The divergence term on the RHS is the energy transfer due to conduction whereas S_E represents volumetric heat sources.

Also, $E_k = h_k - \frac{p}{\rho_k} + \frac{v^2{}_k}{2}$ (A.8)

For, incompressible phases, $E_k = h_k$

Here, h_k is the sensible enthalpy for the phase k

Volume fraction equation for the secondary phases

The volume fraction equation for a secondary phase p can be obtained from the continuity equation for the phase and is given by

$$\frac{\partial}{\partial t}(\alpha_p \rho_p) + \nabla \cdot (\alpha_p \rho_p \vec{v}_m) = -\nabla \cdot (\alpha_p \rho_p \vec{v}_{dr,p}) + \sum_{q=1}^{n} (\dot{m}_{qp} - \dot{m}_{pq}) \tag{A.9}$$

TURBULENCE MODELING AND THE STANDARD k-ε TURBULENCE MODEL

Various turbulence models are available for modeling turbulence. Before selecting a turbulence model, it should be determined which is best suited for the application under consideration. The standard k-ε model, which is one of the most popular turbulence models, was used for this study since encouraging results have been obtained by researchers in the past using this model for flow through annular seal, small clearance and geometries similar to that of the squeeze film damper.

A turbulence model is used to model the Reynolds stress term in the Reynolds-Averaged Navier-Stokes or RANS equations. To obtaining the RANS equations, the flow variables are decomposed into mean and fluctuating components. Therefore, the velocity would be represented by $u_i = \overline{u}_i + u_i'$ where $\overline{u}_i$ is the time-averaged component of the velocity and u_i' is the fluctuating component. These kinds of expressions are substituted into the continuity and momentum equations and a time-average of the resulting equation is taken to obtain the RANS equations

$$\frac{\partial \rho}{\partial t} + \frac{\partial}{\partial x_i}(\rho \overline{u}_i) = 0 \tag{A.10}$$

$$\frac{\partial}{\partial t}(\rho \overline{u}_i) + \frac{\partial}{\partial x_j}(\overline{u}_i \overline{u}_j) = -\frac{\partial \overline{p}}{\partial x_i} + \frac{\partial}{\partial x_j}\left[\mu\left(\mu \frac{\partial u_i}{\partial x_j} + \frac{\partial u_j}{\partial x_i} - \frac{2}{3}\delta_{ij}\frac{\partial u_l}{\partial x_l}\right)\right] + \frac{\partial}{\partial x_j}(-\rho\overline{u_i' u_j'}) \tag{A.11}$$

For the closure of the above equation, the Reynolds stress term, $\rho\overline{u_i' u_j'}$ needs to be modeled. For several turbulence models like the Spalart-Allmaras, the k-ε model and the k-ω model this term using the Boussinesq hypothesis of relating the Reynolds stresses to the mean velocity gradients.

$$-\rho\overline{u_i' u_j'} = \mu_t\left(\frac{\partial u_i}{\partial x_j} + \frac{\partial u_j}{\partial x_i}\right) - \frac{2}{3}\left(\rho k + \mu_t \frac{\partial u_k}{\partial x_k}\right)\delta_{ij} \tag{A.12}$$

where μ_t is the turbulent viscosity and δ_{ij} is the Kronecker delta. The above mentioned models use different correlations for μ_t

The standard k-ε model is a 2 equation model which was first proposed by Launder and Spalding. For this model the transport equations for Turbulence Kinetic Energy (k) and the Turbulence Kinetic Energy Dissipation rate (ε) are derived using the energy equation and physical intuition respectively. They are then solved to obtain *k* and *ε* which are used to obtain μ_t given by $\mu_t = \rho C_\mu \frac{k^2}{\varepsilon}$ where C_μ is constant. The transport equations for *k* and *ε* are given by

$$\frac{\partial}{\partial t}(\rho k) + \frac{\partial}{\partial x_i}(\rho k u_i) = \frac{\partial}{\partial x_j}\left[\left(\mu + \frac{\mu_t}{\sigma_k}\right)\frac{\partial k}{\partial x_j}\right] + G_k + G_b - \rho\varepsilon - Y_M + S_k \tag{A.13}$$

$$\frac{\partial}{\partial t}(\rho\varepsilon)+\frac{\partial}{\partial x_i}(\rho\varepsilon u_i)=\frac{\partial}{\partial x_j}\left[\left(\mu+\frac{\mu_t}{\sigma_\varepsilon}\right)\frac{\partial\varepsilon}{\partial x_j}\right]+C_{1\varepsilon}\frac{\varepsilon}{k}(G_k+C_{3\varepsilon}G_b)-C_{2\varepsilon}\rho\frac{\varepsilon^2}{k}+S_\varepsilon$$

where,

G_k is the generation of turbulence kinetic energy due to the mean velocity gradients given by $2\mu_t S^2$ where

$$S=\sqrt{2S_{ij}S_{ij}} \tag{A.14}$$

and $S_{ij}=\frac{1}{2}\left(\frac{\partial u_i}{\partial x_j}+\frac{\partial u_j}{\partial x_i}\right)$ (A.15)

G_b is the generation of turbulence kinetic energy due to buoyancy given by

$$G_b=\beta\frac{\mu_t}{\mathrm{Pr}_t}\frac{\partial T}{\partial x_i} \tag{A.16}$$

Y_M represents the effect of compressibility on turbulence given by

$$Y_M=\frac{2\rho\varepsilon k}{\gamma RT} \tag{A.17}$$

σ_k, σ_ε are turbulent Prandtl numbers for *k* and *ε* respectively

S_k, S_ε are user-defined source terms.

The following values of constants, which are the default values, were used for the study-

$C_{1\varepsilon}$=1.44, $C_{2\varepsilon}$=1.92, C_μ=0.09, σ_k=1.0 and σ_ε=1.3

APPENDIX B

A moving reference frame is used render a problem which is unsteady into a frame steady with respect to the moving frame. For a steadily rotating frame (i.e., the rotational speed is constant), it is possible to transform the equations of fluid motion to the rotating frame such that steady-state solutions are possible. The following is a description of the equations for a Rotating Reference Frame.

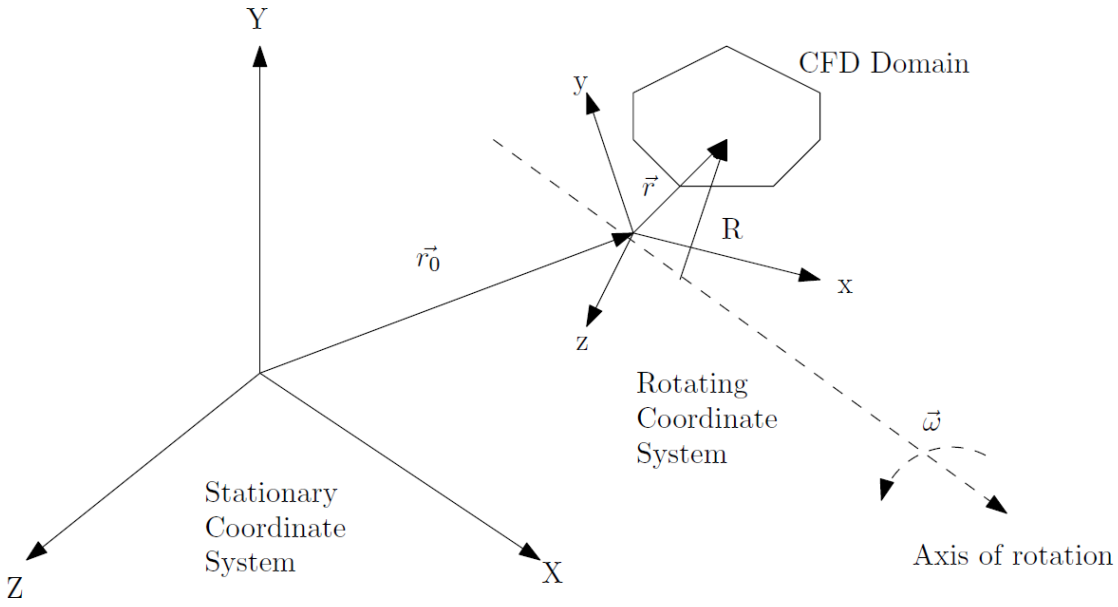

Figure B1. Stationary and Rotating Reference Frames

Consider a coordinate system which is rotating steadily with angular velocity $\vec{\omega}$ relative to a stationary (inertial) reference frame, as illustrated in Figure B1. The origin of the rotating system is located by a position vector $\vec{r}_0$.

The axis of rotation is denoted by a unit direction vector $\hat{a}$ such that

$$\vec{\omega} = \omega \hat{a} \tag{B.1}$$

The computational domain for the CFD problem is defined with respect to the rotating frame such that an arbitrary point in the CFD domain is located by a position vector $\vec{r}$ from the origin of the rotating frame. The fluid velocities can be transformed from the stationary frame to the rotating frame using the following relation:

$$\vec{v}_r = \vec{v} - \vec{u}_r \tag{B.2}$$

where $\vec{u}_r = \vec{\omega} \times \vec{r}$ (B.3)

In the above, $\vec{v}$ is the relative velocity (the velocity viewed from the rotating frame), $\vec{v}$ is the absolute velocity (the velocity viewed from the stationary frame), and $\vec{u}_r$ is the "whirl" velocity (the velocity due to the moving frame).

When the equations of motion are solved in the rotating reference frame, the acceleration of the fluid is augmented by additional terms that appear in the momentum equations. Moreover, the equations can be formulated in two different ways:

i. Expressing the momentum equations using the relative velocities as dependent variables (known as the relative velocity formulation).
ii. Expressing the momentum equations using the absolute velocities as dependent variables in the momentum equations (known as the absolute velocity formulation).

FLUENT's pressure-based solvers provide the option to use either of these two formulations, whereas the density-based solvers always use the absolute velocity formulation.

The details of the Relative Velocity Formation are as follows-

For the relative velocity formulation, the governing equations of fluid flow for a steadily rotating frame can be written as follows:

Conservation of mass:

$$\frac{\partial p}{\partial t} + \nabla \cdot \rho \vec{v}_r = 0 \tag{B.4}$$

Conservation of momentum:

$$\frac{\partial (\rho \vec{v}_r)}{\partial t} + \nabla \cdot (\rho \vec{v}_r \vec{v}_r) + \rho (2\vec{\omega} \times \vec{v}_r + \vec{\omega} \times \vec{\omega} \times \vec{r}) = -\nabla p + \overline{\overline{\tau}}_r + \vec{F} \tag{B.5}$$

The momentum equation contains two additional acceleration terms: the Coriolis acceleration $2\vec{\omega} \times \vec{v}_r$ and the centripetal acceleration $\vec{\omega} \times \vec{\omega} \times \vec{r}$.

To set up the Coordinate Transformation case, a steady state pressure based solver is selected. In the ‘Cell Zone Conditions’ Menu, motion needs to assigned to the fluid. The center of the Stator which also happens to be the origin of the global coordinate system is assigned as the Rotation-axis origin. In the ‘Motion Type’ sub-menu, Moving Reference Frame is selected. In the velocity definition sub-menu, a rotational velocity equal to the rotor whirl speed is assigned to the fluid.

APPENDIX C

For this work, the dynamic mesh capability of FLUENT has been used to simulate the whirling motion of the rotor accommodates changes in the shape of the domain, at each time step. This section explains the theory behind the dynamic mesh approach and procedure required to set up the dynamic mesh in detail. The orbit paths were then simulated using User Defined Functions (UDFs) in FLUENT, which are basically programs written in C++ that specify the motion of the rotor.

USING DYNAMIC MESHES IN FLUENT

In a SFD, the rotation motion of the journal or rotor about its center is prevented by an anti-rotation pin. However, the rotor is free to undergo whirl motion. To reproduce the circular whirl motion of the rotor about the center of the stator a User Defined Function (UDF) was used in conjunction with the dynamic mesh functionality. The changing shape of the fluid domain was thus accommodated using the dynamic meshing capability in FLUENT while the orbit path, i.e. the motion of the rotor was specified using User Defined Functions (UDFs). Dynamic meshing basically enables FLUENT to update the volume mesh for the domain at each time step, based on the new positions of the boundaries. It is, however, necessary to initially have a good quality volume mesh to ensure that all the flow properties are captured satisfactorily.

When a dynamic mesh is used, FLUENT uses one of several available mesh motion methods in order to update the volume mesh that is subject to deformation. These methods are classified under smoothing methods, dynamic layering and local remeshing methods. The method that has been used for the simulations in this study is the spring-

based smoothing method. Here, the edges between any two nodes are taken as a network of springs and the spacing between the nodes in the initial mesh is taken as the equilibrium state. The force acting at each mesh node is then calculated (taking into account a user-defined spring constant) and the condition that at equilibrium the net force acting should be zero are used to obtain an iterative equation. As per Hook's law, the force on the mesh node is given by

$$\vec{F}_i = \sum_j^{n_i} k_{ij}(\Delta\vec{x}_j - \Delta\vec{x}_i)$$

where $\Delta\vec{x}$ represents the displacement of the node, n_i the number of neighboring nodes and k_{ij} the spring constant between node i and its neighbor j. The spring constant for the edge connecting nodes i and j is defined as

$$k_{ij} = \frac{1}{\sqrt{\left|\vec{x}_i - \vec{x}_j\right|}}$$

Using the condition that at equilibrium the net force at a node is zero, the iterative relation obtained is

$$\Delta\vec{x}_i^{\,m+1} = \frac{\sum_j^{n_i} k_{ij}\Delta\vec{x}_i^{\,m}}{\sum_j^{n_i} k_{ij}}$$

As the displacements are known at the boundaries (from the new boundary positions) a Jacobi sweep is performed to solve (1.2) on all interior nodes. At convergence

$$x^{-n+1} = x^{-n} + \Delta x^{-m,converged}$$

where n+1 and n are the positions at the next and the current time step respectively. The FLUENT manual recommends the use of the spring-based smoothing method for non-

tetrahedral meshes under the following cases: when the boundary of the zone moves predominantly in one direction or when the motion is predominantly normal to the boundary zone. Since these conditions are compliant with the geometry and motion of the simulations to be performed, this was the remeshing method of choice. The spring based smoothing method is enabled by default only for the tetrahedral meshing scheme. In order to use it for this work, where a hexahedral mesh was used, the smoothing method can be enabled for all cell types by using the following command

(rpsetvar ‘dynamesh/spring/all-element-type? #t)

Alternatively, the following chain of commands can be used

```
define models dynamic-mesh-controls
smoothing-parameter spring-on-all-shapes?
```

DESCRIBING ROTOR MOTION USING UDFS

In order to specify the motion of the rotor for each of the orbit paths to be simulated, the use of FLUENT’s ability to accommodate problem specific changes to the existing code, is made. Each different case run required the use of two UDFs (User Defined Functions) - one to specify the orbit path and another to specify the surface velocity for the whirling rotor. An UDF in FLUENT can be used for a variety of applications from problem definition to post processing as the need may arise. It is essentially a code written using a C programming language which can be dynamically linked to the solver. For the present application, the programs have been written in C++ using a Visual Studio editor. UDFs typically start with the `udf.h` file inclusion directive and are defined using the DEFINE macros that are provided by FLUENT. This program,

known as the source code, is saved with a .c extension and can then be interpreted or complied in FLUENT. The very first step in using a UDF is to define the problem mathematically, i.e., in the present application, for the motion of the rotor in a certain orbit path, it is necessary to have a set of equations that describe the motion. The next step is to incorporate these equations into C code. As mentioned in the previous paragraph, FLUENT provides a number of predefined functions or macros which can be used depending on the application. The general format of the DEFINE macro is as follows:

DEFINE_macroname (udf_name, passed-in variables)

The definitions for the macros used are all contained in the udf.h header file which must be included at the beginning of every UDF source code. This is done using the following complier directive

#include “udf.h”

While programming a UDF for FLUENT, it is useful to know that in addition to the standard data types from C, FLUENT has its own data types to represent the various computational units. Examples of these data types are - Node, face_t, cell_t and Thread. It is also important to know that in a UDF, zones (as in fluid and boundary zones defined in FLUENT) are referred to as threads.

For the present application, in addition to the basic DEFINE macros, specifying the rotor motion required the use of vector and dimension macros. These macros are used to access and manipulate vector quantities and can be used for both two and three dimensional applications. The first DEFINE macro used in this application is the

DEFINE_CG_MOTION macro which specifies the motion of the dynamic zones by using the angular and linear velocities at each time step. These velocities are then used to update the node positions on the dynamic mesh zones based on the solid-body motion. The general syntax for the function is as follows

DEFINE_CG_MOTION (name, dt, vel, omega, time, dtime)

The arguments used are as follows:

i. *name* ,which is the UDF name and is specified by the user

ii. *dt*, which is a pointer to the structure that stores the dynamic mesh attributes. This is passed from FLUENT directly to the UDF.

iii. *vel*, a real variable which specifies the linear velocity. Its value is passed directly from FLUENT to UDF.

iv. *omega*, a real variable which specifies the angular velocity. This is passed from FLUENT directly to the UDF.

v. *time* , a real variable which specifies the current time. Its value is passed directly from FLUENT to UDF.

vi. *dtime*, a real variable which specifies the time step .This is also passed from FLUENT directly to the UDF.

In addition to the DEFINE macro, a few other macros were used to handle the vector manipulations in the program. These include the NV macros which operate on vectors, and can be used to perform operations right from the definition of the vector to compute dot and cross products. The program also uses a looping macro – begin…end_f_loop which is used to perform operations over all the faces of a given

thread. Another macro used is F_NODE which is used to call vector information such as the coordinate. For this application, this macro is used when the coordinate data for the current node is required within the begin…end_f_loop macro. The complete UDF for the circular orbit, is as follows:

```
/************************************************************
 *
 * Rotor's whirling motion UDF
 * compiled UDF
 *
 ************************************************************/
#include "udf.h"
#include "stdio.h"

DEFINE_CG_MOTION(ROtor_Motion,dt,vel,omega,time,dtime)
{
  Thread *tf = DT_THREAD (dt);
  face_t f;
  Node *v;
  real NV_VEC (axis), NV_VEC (dx);
  real NV_VEC (origin), NV_VEC (rvec), NV_VEC (center), NV_VEC (trans);
  real rotation_radii, RPM;
  real time1, time2, theta1, theta2;
  int n;
  /* set deforming flag on adjacent cell zone */
  SET_DEFORMING_THREAD_FLAG (THREAD_T0 (tf));

  rotation_radii = 0.001*0.0254;  //Whirling radius
  RPM = 56.54866776; //  rad/sec- 540RPM: whirling speed

  NV_D (axis, =, 0.0, 0.0, 0.001);
  NV_D (origin, =, 0.0, 0.0, 0.0);
  NV_D (center, =, rotation_radii, 0.0, 0.0);
  NV_D (trans, =, 0.0, 0.0, 0.0);
  time1 = time;
  time2 = time+dtime;
  theta1= time1 * RPM;
  theta2= time2 * RPM;
  Message ("\n whirl angle=%f     time=%f\n,"theta1*180/3.141592,time);
                if (fabs(theta1) > 6.28318531)
                theta1 -= 6.28318531;
                if (fabs(theta2) > 6.28318531)
                theta2 -= 6.28318531;
  trans[0] = rotation_radii*(cos(theta2)-cos(theta1));  //unit in m
  trans[18] = rotation_radii*(sin(theta2)-sin(theta1));  //unit in m
  Message  ("%f   %f    %f  \n," theta1*180/3.141592, trans[0],
trans[18]);
  begin_f_loop (f, tf)
```

```
    {
      f_node_loop (f, tf, n)
        {
          v = F_NODE (f, tf, n);
                if (NODE_POS_NEED_UPDATE (v))
                                    {
                                    NODE_POS_UPDATED(v);
                                    NV_V (NODE_COORD (v), +=, trans);
        }
        }
    }
  end_f_loop (f, tf);

}
```

The first two lines of the program deal with linking the header files required by the UDF udf.h as mentioned earlier and stdio.h which is the “standard input/output header” and provides functions for input and output operations. The next part involves the usage of the DEFINE macro which has been given the name Rotor_Motion. Within the macro, the first line returns a pointer to the face thread for which the dynamic mesh attributes are specified and this is stored in the pointer `*tf.` The next few lines deal with the declaration of the user defined variables used in the program – the vectors defined are `axis, dx, origin, rvec, center` and `trans` while the scalar variables defined are `theta1, theta2, rotation_radii, RPM, time1` and `time2.` The deforming flag is then set on the adjacent cell zone which is followed by the initialization of the variables.

The variable `rotation_radii` indicates the whirling radius of the seal and this is given by half the value of the eccentricity of the rotor, about the center of the seal (the value is multiplied by 0.0254 to account for the conversion to SI units). The next variable initialized is RPM which indicates the whirling speed (in rad/sec) – this is the variable whose value is changed for different whirl speeds. Similarly the variables

`axis, origin, center` and `trans` are all initialized in the vector form while the values for the variables `time1` and `time 2` are passed to the function from FLUENT itself. Within FLUENT, the time step is computed as follows – for the rotor speed of 540 RPM, which is 9 Hz, which is $1/9^{th}$ of a second for 1 revolution; therefore for a one degree increment, the time step would be 1/(360X9) seconds. The values for `theta1` and `theta2` are then calculated from the values of the `time` variables by multiplying it with the whirling speed. After the variables are initialized, an `if` condition is used to ensure that the values of the angles `theta1` and `theta2` do not exceed 360^0. The next part is to specify the coordinates of the center of the rotor wall according to the orbit path and this is computed using the values of `theta1`, `theta2` and the whirling radius`.` Here, the first two elements of the `trans` vector indicate the x and y coordinates of the center respectively and each element is calculated individually. A loop is then set up using the begin…end_f_loop macro in order to loop over the entire thread and within this, the f_node_loop is used to loop over all the nodes of each face of the thread. An `if` condition is then used within the loop to ensure all the nodes are updated.

VITA

Name: Milind Nandkumar Khandare

Address: Department of Mechanical Engineering,
c/o Dr. Gerald Morrison,
Texas A&M University,
College Station TX 77843-3123

Email Address: nk.milind@gmail.com

Education: B.E., University of Pune, Pune, India, 2007
M.S., Mechanical Engineering, Texas A&M University, 2010